

Late Holocene flood history and tephrochronology using lake sediments from Cajas National Park, south central Ecuador

Master's Thesis

Faculty of Science

University of Bern

presented by

Stéphanie Arcusa

2016

Supervisor:

Prof. Dr. Martin Grosjean

Geographical Institute and Oeschger Centre for Climate Change Research

Advisors:

Tobias Schneider & Dr. Adrien Mestrot

Geographical Institute and Oeschger Centre for Climate Change Research



Cajas National Park eastern side. Credits: W. Tylmann



Cajas National Park south western side. Credits: W. Tylmann

Abstract

Lake sediments archive past changes of the environment and climate. Cajas National Park (2°40' – 3°00'S, 79°00' – 79°25'W), located at high altitude in south central Ecuador, is home to hundreds of lakes which have the potential to record these changes. Cajas National Park is affected by El Niño Southern Oscillation (ENSO) events in the form of extreme precipitation. Whether these are more related to El Niño or La Niña phase remains disputed but the length of observational records hinders the possibility to predict future changes. Lake sediments containing flood layers provide the opportunity to extend the flood history through time. High resolution reconstructions require high precision dating which must be correlated over wide distances. Being located in a volcanic centre, Cajas National Park receives ash fallout as tephra and cryptotephra. These layers can be used to correlate events temporally and spatially. Furthermore, high altitude lakes, once presumed to have remained in a pristine condition, have been impacted by human activities over the last 50 years. In the lakes of Cajas National Park, the impact was caused by fish hatcheries. Lake sediments also provide the means to investigate the scale of these changes.

Four high altitude lakes (3140 - 4133 m) were cored in 2014 and 2015 field campaigns. High resolution ^{210}Pb and ^{14}C dating performed on L. Llaviucu and L. Fondococha provided age-depth profiles. A combination of visual observation, X-Ray Fluorescence (XRF) and hyperspectral image spectrometry was combined to the age profile to produce a flood history for L. Llaviucu. Visual inspection, microscopic analysis, Magnetic Susceptibility Core Scanner (MSCL) and XRF were used to detect volcanic layers in the four lakes. A cleaning procedure based on a stepped density separation technique was conceptualised to purify the bulk tephra samples. The samples were then dissolved by total digestion and fingerprinted for major, minor, and rare earth elements by Inductive Coupled Plasma Mass-Spectrometer (ICP-MS). The colour of tephra was assessed by the Munsell chart and morphology identified by scanning electron microscope (SEM). A tephrostratigraphy was established using the datasets of componentry, colour and geochemistry through statistical methods such as principal component analysis, similarity coefficient and cluster analysis. The results were combined with radiocarbon dating of terrestrial macrofossils to produce a tephrochronology of the late Holocene for Cajas National Park. In order to trace the impact of the fishing activity in L. Llaviucu, elemental C and N as well as ^{13}C and ^{15}N isotopes were measured from bulk sediment samples.

The flood reconstruction shows three distinctive periods of enhanced and suppressed extreme events. The periods 500 - 1000 B.C.E. and 750 - 2014 C.E. saw enhanced frequencies while reduced frequencies were observed in the intermittent period. The pattern compares well to the L. Pallacocha reconstruction by Moy et al. (2002). One to four thin, distal tephra layers were identified in each lake. The geochemical fingerprint from bulk tephra analysis was contaminated by detrital material. Nevertheless, two tephrochronomarkers were identified from the combined statistical analysis of the different datasets. One definitive new tephrochronomarker is established at 1224 (-247, +369) cal. yrs BP. One less certain is dated to 623 - 837 (-105, +79; -165, +352 respectively) cal. yrs BP. Finally, overall decreases in lake geochemistry might have been influenced by changes in thermal stratification, in nutrient origin, or from the atmospheric composition as well as the fishing activity. Overall, the main influence on the lake geochemical record remains inconclusive.

Contents

Abstract	III
Contents	IV
List of Figures	VIII
List of Tables	IX
Acknowledgements	X
1 Introduction	1
1.1 Research motivation.....	1
1.2 Research questions	3
1.3 Project design.....	4
1.4 Project outline.....	4
2 Study Site	6
2.1 Cajas National Park in Ecuador.....	6
2.2 Volcanic landscape	6
2.3 Climatic influences	8
2.4 Lake systems.....	9
2.5 Vegetation at CNP	10
2.6 Soils in Cajas.....	12
2.7 Anthropogenic Impact.....	12
2.7.1 The fishing industry	13
3 Tephra in the literature	14
3.1 Background	14
3.2 Tephrochronology.....	14
3.2.1 Tephra layer identification by scanning.....	14
3.2.2 Tephra identification by core sub-sampling.....	15
3.2.3 Tephra glass shard purification	15
3.2.4 Tephra morphology	16
3.2.5 Tephra concentration.....	17
3.2.6 Preparation for geochemical fingerprinting.....	18
3.2.7 Geochemical fingerprinting	18

3.2.8	Statistical analysis of geochemical data.....	19
4	Methods.....	21
4.1	Fieldwork.....	21
4.1.1	Lake sediment cores	21
4.1.2	Sediment traps and thermistors	22
4.1.3	Algae collection.....	22
4.2	Core opening and sediment description	23
4.2.1	Sediment description.....	23
4.3	Sub-sampling and sample preparation.....	23
4.3.1	Dating.....	23
4.3.2	Samples for the tephra chronology	24
4.3.3	Samples for wet chemical analysis	24
4.4	Scanning techniques.....	25
4.4.1	Multi-Sensor Core Logger (MSCL).....	25
4.4.2	μ XRF.....	25
4.4.3	Tephra layer identification from scanning techniques	26
4.4.4	Hyperspectral core scanner.....	26
4.5	Flood layer classification	27
4.5.1	L. Llaviucu core correlation	27
4.5.2	XRF classification	27
4.5.3	HI classification.....	27
4.6	Wet chemical analysis.....	28
4.6.1	Elemental carbon and nitrogen.....	29
4.6.2	^{13}C and ^{15}N isotopes.....	29
4.6.3	Statistical analyses.....	31
4.7	Dating techniques.....	31
4.7.1	The ^{210}Pb cycle.....	31
4.7.2	Constant Initial Supply (CIS) model	33
4.7.3	Constant Rate of Supply (CRS) model.....	33
4.7.4	Sediment Isotope Tomography (SIT) model	34
4.7.5	Mass accumulation rate (MAR)	34

4.8	Theory behind radiocarbon dating	35
4.8.1	Radiocarbon dating of the CNP lakes.....	35
4.9	Tephra analysis.....	37
4.9.1	Optical identification	37
4.9.2	Extraction test	38
4.9.3	Applied extraction	40
4.9.4	Colour and morphological classification	42
4.9.5	Total digestion.....	42
4.9.6	Geochemical analysis and processing.....	43
4.9.7	Compilation of the datasets	45
4.9.8	Data visualization and description	45
4.9.9	Statistical analysis of the datasets and tephra classification	45
4.9.10	Tephra stratigraphy	47
5	Results.....	48
5.1	Age-depth models of the CNP lakes	48
5.1.1	L. Llaviucu	48
5.1.2	L. Fondococha.....	51
5.2	L. Llaviucu flood frequency.....	54
5.2.1	L. Llaviucu sediment description.....	54
5.2.2	L. Llaviucu master core.....	54
5.2.3	Flood layer classification	57
5.2.4	Flood frequency reconstruction.....	59
5.3	Tephra Analysis.....	63
5.3.1	Tephra layer identification.....	63
5.3.2	Physical characteristics of tephra and their classification.....	68
5.3.3	Qualitative tephra elemental composition	75
5.3.4	Quantitative tephra geochemistry	77
5.3.5	Statistical analysis of the geochemical datasets and tephra classification.....	78
5.3.6	Tephra layer descriptions	84
5.3.7	Tephra correlation.....	84
5.4	Wet chemistry analysis	86

5.4.1	Modern algae	86
5.4.2	Elemental analysis and water content	86
5.4.3	Stable isotopes	87
5.4.4	Statistical analysis.....	89
5.4.5	Hyperspectral images.....	90
6	Discussion.....	92
6.1	Age-depth profiles of Llaviucu and Fondococha.....	92
6.2	Flood reconstruction of the last 3000 years.....	93
6.3	Tephrochronology of CNP.....	96
6.3.1	Volcanic origin of the layers	96
6.4	Uncertainties and limitations of the tephrochronology	98
6.4.1	Tephra type	98
6.4.2	Tephra deposition.....	99
6.4.3	Methodology: tephra identification.....	100
6.4.4	Methodology: cleaning and measurement	101
6.4.5	Statistical correlation	103
6.4.6	Remarks to the limitations and uncertainties.....	103
6.5	The impact of fishing and environmental and climatic change on lake geochemistry	104
7	Conclusions.....	108
7.1	Summary	108
7.2	Concluding remarks.....	109
7.3	Research importance	110
7.4	Recommendations for future research.....	110
8	References	111
	Plate I: Macrofossils L. Llaviucu	122
	Plate II: Macrofossils L. Fondococha.....	123
	Plate III: Tephra	124
	Plate IV: Tephra continued	125
	Declaration	126

List of Figures

Fig. 2-1 The location of Ecuador, Cajas National Park and the lakes investigated in Ecuador.	7
Fig. 2-2 Location of volcanoes in relation to Cajas National Park.....	8
Fig. 2-3 Páramo landscape around Laguna Pallcacocha.	11
Fig. 2-4 Sub-páramo ecosystem in the direction of L. Riñoncocha.....	11
Fig. 2-5 Montane forest and pastoral grassland in the valley of L. Llaviucu.....	12
Fig. 3-1 Descriptive terminology for microscopic tephra classification.....	17
Fig. 4-1 L. Llaviucu 2015 core shown with example locations of training areas.....	28
Fig. 4-2 C:N and $\delta^{13}\text{C}$ isotopic signature for C3 and C4 land plants and algae	29
Fig. 4-3 Nitrogen and carbon isotopic signatures of land plant types and algae.....	30
Fig. 4-4 Radioactive decay chain of ^{238}U to ^{210}Pb	32
Fig. 4-5 Light microscope images of pumice, green particles and striated glass shards.....	38
Fig. 4-6 Flowchart of the step density and clay removal cleaning procedure.	41
Fig. 4-7 Descriptive terminology for microscopic tephra classification.....	42
Fig. 5-1 ^{210}Pb data and CRS model with missing inventory corrections for L. Llaviucu.	48
Fig. 5-2 Age-depth model for L. Llaviucu using the BACON software.	50
Fig. 5-3 L. Llaviucu slump-corrected age-depth model using the CLAM model.....	51
Fig. 5-4 ^{210}Pb data, MAR and CRS age-depth model for L. Fondococha.	52
Fig. 5-5 Age depth model for L. Fondococha using the BACON software	53
Fig. 5-6 Sediment descriptions of L. Llaviucu 2014 and 2015 cores.	55
Fig. 5-7 Example of tephra, organic rich and flood layer in L. Llaviucu.....	54
Fig. 5-8 Llaviucu core correlation based on visual inspection and master core.....	56
Fig. 5-9 Quality control for Llaviucu hyperspectral images.	57
Fig. 5-10 Hyperspectral unsupervised layer classification of layers in L. Llaviucu.....	58
Fig. 5-11 Ti and K profiles for L. Llaviucu 2014 and 2015 cores.....	60
Fig. 5-12 Flood classification of the L. Llaviucu mastercore.	61
Fig. 5-13 Final flood frequency reconstruction for L. Llaviucu.....	62
Fig. 5-14 Organisms found in the modern algae sample.	86
Fig. 5-15 L. Llaviucu physiochemical profiles	88
Fig. 5-16 Llaviucu $\delta^{13}\text{C}$ and $\delta^{15}\text{N}$ biplot using age regularized data.....	89

Fig. 5-17 Llaviucu $\delta^{13}\text{C}$ and C:N ratio biplot using age regularized data.....	90
Fig. 5-18 Image and hyperspectral scans of L. Llaviucu sediment core LLA14-1.	91
Fig. 5-19 MSCL profiles from L. Llaviucu, L. Fondococha and L. Riñoncocha.	64
Fig. 5-20 Sr counts from L. Llaviucu, L. Fondococha, L. Riñoncocha and L. Estrellascocha.	65
Fig. 5-21 Tephra images of light and scanning microscope investigation..	66
Fig. 5-22 Tephra layers overview.....	67
Fig. 5-23 Image test results.....	69
Fig. 5-24 SEM tephra morphology results	70
Fig. 5-25 SEM tephra surface features results.	70
Fig. 5-26 Colour wheel of tephra samples	74
Fig. 5-27 Elemental ratios for L. Estrellascocha, L. Fondococha, L. Riñoncocha and L. Llaviucu... 76	
Fig. 5-28 Line plot of the REE in the A1 dataset.	78
Fig. 5-29 Tephrochronology of Cajas National Park for the last 2000 years.....	85
Fig. 6-1 Comparison of the different ^{210}Pb age-depths models for L. Llaviucu.....	92
Fig. 6-2 Flood event comparison of this study to Moy et al. (2002) for the last 3000 years.	95
Fig. 6-3 Summary plot of the analytic analysis of ^{13}C , ^{15}N and C:N ratio for L. Llaviucu.....	104
Fig. 6-4 Schematic of processes affecting the isotopic signal in L. Llaviucu.....	107
Fig. 6-5 Line plot of the REE compared to literature values..	97
Fig. 6-6 Elemental x-y biplots compared to literature values.....	98

List of Tables

Table 2-1 Information on the lakes used in this study.....	10
Table 2-2 Fish cage data.....	13
Table 4-1 Coring locations and core lengths used in this study.....	21
Table 4-2 Location and depth of sediment traps and thermistors in L. Llaviucu.....	22
Table 4-3 Microwave settings for the first programme.....	43
Table 4-4 Microwave settings for the second programme.....	43
Table 4-5 Measured elements and elements without standards available.....	44
Table 4-6 The two geochemical datasets and the elements they contain.	45
Table 5-1 Organic material, their depths and radiocarbon calibrated ages for L. Llaviucu.....	49

Table 5-2 Organic material, their depths and radiocarbon calibrated ages for L. Fondococha.	53
Table 5-3 Tephra layers as well as their percentage volume and colour.	68
Table 5-4 Tephra groups according to morphological features	72
Table 5-5 Results of the unconstrained k-means analysis of the morphological dataset.....	73
Table 5-6 Tephra groups according to their Munsell colour.	75
Table 5-7 The number of significant principal components (PC) for each dataset.....	79
Table 5-8 Result synthesis of A1 and B2 datasets similarity coefficient analysis.....	80
Table 5-9 Dendrogram clustering results of similarity coefficient values A1 and B2 datasets.....	81
Table 5-10 Dendrogram clustering result analysis of the A1 and B2 datasets	82
Table 5-11 Results of the cluster plot analysis using k-means for the A1 and B2 datasets	83
Table 5-12 Synthesis of the cluster plot analysis with k-means	83
Table 6-1 Origin and reference of comparison data of tephra from Ecuadorian volcanoes.....	97

Acknowledgements

This project was made only possible through the help of many people. I would like to thank all my friends in the Climate Science Masters but especially H el ene Barras, Lea Fr ankl and Danae Motta, for amongst many things, getting me through the rough patches, being my moral support and making sure I stay motivated. I would also like to thank my colleagues in the Paleolimnology group. In particular I am indebted to Christoph Butz, Tobias Schneider, Lea Fr ankl, Denise Rimer, Dr. Iv an Hern andez-Almeida, Christoph D atwyler, Dr. Raphael Neukom, Manuel and Nils Kipfer for their insights, daily jokes and excellent coffee breaks. I would like to thank Christoph Butz especially for sharing his knowledge about the Specim scanner and for the late evening and early morning discussions in the lab. Thanks to Manuel for his help preparing the samples, I would not have managed without him. Thanks to Dr. Wojciech Tylmann for helping out in the field and measuring our lead samples. Thanks to Don Simon and Pablo for helping out in the field every time they could. I am grateful to Dr. Daniela Fischer, Dr. Adrien Mestrot and Dr. Moritz Bigalke for their precious assistance in the lab. Many thanks to Dr. S onke Szidat from the Department of Chemistry and Biochemistry for ¹⁴C measurements and to Prof. Dr. Flavio Anselmetti from the Institute of Geological Science for letting me use the Geotek and ITRAX scanners. Thanks to Dr. Krystyna Saunders for reviewing my discussion and providing support from far away and to Aurich Jeltsch-Th ommles for his review. As always, I am grateful for my parents always being there for me. Most of all, I am beholden to Tobias Schneider for being the best advisor I could ever wish for. Finally, I would like to thank Prof. Dr. Martin Grosjean without whom this study would not have been possible. I would also like to thank Martin for believing I could do this and teaching me many wise things about research, but most of all, making me understand that science is never easy.

1 Introduction

1.1 Research motivation

Lake sediment records have been employed to answer a diverse range of questions encompassing environmental change to human impacts to climate change (Cohen, 2003). High-altitude lakes in particular are often used as archives of past environmental changes as we assume they have remained in a pristine state, unaffected by human activities (Guyard et al., 2007; Sarmiento, 2002). This is no longer the case as both direct and indirect anthropogenic impacts can be seen in these environments through the investigation of lake sediments. However, in order to make any concrete interpretations, any record of past changes must be sufficiently dated (Cohen, 2003). Combinations of radiocarbon and ^{210}Pb have proved invaluable to date recent and old lake sediment. Additionally, tephrochronology has provided the means to correlate events between different records (Lowe, 2011). Through well dated lake records, environmental and climatic changes can be reconstructed.

One of these environmental changes is flood frequencies. Lake sediments can offer long reconstructions of flood frequency which would not be otherwise possible due to the short period of observational data (Schillereff et al., 2014). Reconstructing extreme events provides information for a range of questions. For example, the Ecuadorian Andes are prone to landslides during heavy precipitation (Goddard and Dilley, 2005). These catastrophes are often related to strong El Niño Southern Oscillation (ENSO) events (Vos et al., 1999). However, whether flood events are more related to El Niño or La Niña phases remains disputed (Morán-Tejeda et al., 2016; Moy et al., 2002). Furthermore, the length of observational records of ENSO is limited. To forecast the next phenomenon or to predict possible changes of ENSO with climate change in order to prepare for periods of landslides, long past records are necessary. Lake sediments which contain flood layers may contribute a longer timescale perspective.

Flood layers are produced from the mobilization of catchment material during heavy precipitation events which are then deposited in the lake through river drainage or slope in-wash (Gilli et al., 2013; Schillereff et al., 2014). Flood reconstruction from river profiles or tree growth disturbance have limited time coverage and are potentially incomplete due to erosion (Gilli et al., 2013). By contrast, lake sediments offer the possibility to track flood changes as these are recorded as distinct clastic layers with different colour and properties to the general background sedimentation (Gilli et al., 2013). As opposed to normal precipitation events where the sediment settles slowly to the lake floor, an extreme event allows for the sediment to break through the density stratification of the lake water and deposit the layer as an event layer (Gilli et al., 2013). Lakes which offer the best flood records have a steep relief and provide a detrital material type different to that of the background sedimentation (Gilli et al., 2013). A suite of scanning methods can be used to identify and classify flood layers including X-Ray Fluorescence (XRF) (e.g. Wirth et al., 2013), image analysis (e.g. Rodbell et al., 1999) and computer tomography (e.g. Guyard et al., 2007). However, visible and near infrared hyperspectral scanning methods have yet to be used for this purpose. As spectral imaging has been shown to successfully distinguish between different types of sediment (Mix et al., 1992), scanning reflectance spectroscopy may be a fast and inexpensive technique to classify flood layers.

Interpretations from lake sediment records rest on the ability to produce tightly constrained chronologies (Cohen, 2003). Several dating methods are available, including but not limited to ^{210}Pb and ^{14}C dating. Young sediment deposited over the last century is generally dated using the natural radioactive decay of ^{238}U and constrained with detected peaks in man-made radioactive products such as ^{137}Cs from bomb testing culminating in the 1960s (Appleby, 2008). In some circumstances however, unsupported radioactive decay might be variable due to processes such as atmospheric or limnologic (Appleby, 1998). Furthermore, in the same or other circumstances, nuclear particle fallout might not be deposited in certain locations or in undetectable quantity (French, 1960). As ^{210}Pb is restricted to the last 120 years, radiocarbon dating of macrofossils is usually employed to date the older sediment. ^{14}C dating is not without limitations however, with reservoir effects and calibration plateaus hindering precise dating by producing large age uncertainties (Hatté and Jull, 2013). As a result of limitations in both methods, correlating past events throughout lake records is challenging. However, tephrochronology provides an effective solution (Alloway et al., 2013; Lowe, 2011).

Tephrochronology has become an increasingly widespread tool in palaeoclimatology to date high-resolution climate reconstructions as well as correlate climatic events over large distances (Lowe, 2011). In recent decades, palaeoclimatic research has moved towards producing highly resolved syntheses of regional climate change for regions with particularly low number of available records (e.g. Villalba et al. 2009). This endeavour highlights the need to constrain age-depth models and correlate climatic events over wide distances. Tephrochronology provides the means necessary to do both. However, while there are many tephrochronologies for the northern hemisphere (e.g. Sulpizio et al. 2003; Vogel et al. 2009; Mackay et al. 2016; Hafliðason et al. 2000; Brendryen et al. 2010) and Australasia (e.g. Lowe et al. 2008; Lowe 2008 for reviews), few are available for South America (e.g. Bertrand et al. 2008; Placzek et al. 2009; Fontijn et al. 2014; Van Acker et al. 2014), especially for Ecuador (e.g. Rodbell et al. 2002), which limits the possibilities to date and correlate climate reconstructions. Though Rodbell et al. (2002) produced a tephrochronology for South Central Ecuador, their work focused mostly on the mid Holocene period, leaving the past two thousand years of ash fall out history largely unexplored.

Although the use of single shard tephrochronology through laser ablation or electron microprobe has been widely applied to lake sediments (e.g. Vogel et al. 2009; Rodbell et al. 2002; Hopkins et al. 2015), certain depositional environments only favour finer sized ash material which cannot be hand-picked. In such circumstances bulk sample solution nebulisation and subsequent inductively coupled plasma mass spectrometry (ICP-MS) measurements may offer an efficient solution. An improved step cleaning procedure based on previous work by Blockley et al. (2005) and Turney (1998) can provide purified bulk tephra material for analysis. The volcanoes of Ecuador located in the Northern Volcanic Zone produce andesitic eruptions ejecting weathering-prone, fine, mineral-rich material (Shane, 2000). This tephra property makes correlations challenging due to the difficulty in geochemically fingerprinting the particles. Nevertheless, combining multiple datasets such as componentry, colour, and geochemistry with statistical methods including cluster analysis, principal component analysis and similarity coefficients, provides the means necessary to correlate the layers.

In addition to being useful archives of past natural events, lakes also record the activities of local and distant populations. In some remote locations such as the Ecuadorian Cordillera, lacustrine fisheries have been set up to provide employment and extra protein availability to an

otherwise rural population (Bondad-Reantaso, 2007). These activities are naturally welcomed by the local communities as it is assumed that the environment would buffer any pollution produced (Sarmiento, 2002). However, as was the case for Ecuadorian lakes where such changes occurred, water quality soon began to degrade polluting the water resource of nearby city of Cuenca (Barros and Carrasco, 2006). While the fisheries were shut down as a result of this awareness, and the lake quality returned to a drinkable state in a relatively short period, it remains unclear whether the sediment returned to its natural state. What is “natural” is also poorly defined, but lake sediment records allow for the establishment of a baseline through the quantitative analysis of lake properties through time (Battarbee, 1999; Dearing et al., 2006). Only then can the remedial action be ascertained to have returned the environment to its natural state. The introduction of alien species is an example of localized direct human impact. On the contrary, anthropogenic activities throughout most of the industrialized world have had a strong and persistent indirect impact in the form of climate change (Adrian et al., 2010). Global warming impacts in lakes include effects such as the heating of surface water temperature (Austin and Colman, 2007), the enhancement of thermal stratification (Livingstone, 2003) and the decline in productivity (Tierney et al., 2010).

Lakes record such environmental and climatic changes as the chemistry and physical properties of the water and the sediment are altered (Cohen, 2003). Methods that may recover these changes include stable isotopes of nitrogen and carbon which have been widely used in lacustrine settings (see Ohkouchi et al. 2015 for a review). In general, relative depletions of carbon but enrichments in nitrogen have been linked to anthropogenic impacts such as waste water and agricultural runoff entering the lake (Torres et al., 2012). Other uses of stable nitrogen isotopes have included tracking changes in the food chain such as with the introduction of predators which would produce a trophic level fractionation of +3.4 ‰ (Vander Zanden et al., 1999). Depletion in the $\delta^{13}\text{C}$ ratio has also been shown to record increases in lake thermal stratification (Cohen, 2003; Torres et al., 2012). Thermal stratification in high altitude lakes is unusual and has been linked to climatic change (Michelutti et al., 2016; Tierney et al., 2010). More common methods include the calculation of carbon to nitrogen elemental ratios which may help discriminate the origin of the organic sediment (Cohen, 2003; Meyers, 1994). Whether sediment is produced within the lake or is washed into the water body from the surrounding watershed leaves a different signal which may be climatic or anthropogenic (Meyers and Ishiwatari, 1993). Finally, hyperspectral scanning procedures in the near-infrared have been shown useful to uncover the beginning of significant human impact (Arcusa et al., 2015).

Lake sediments offer the possibility to answer pressing concerns revolving around the threat of climate induced changes on the natural environment as well as anthropogenic impacts degrading valuable resources. A wide range of methods including scanning procedures and analytical analyses are available to learn from the past.

1.2 Research questions

This Master’s thesis aims to answer the following research questions:

- (1) Can flood layers in the sediment of L. Llaviucu be classified and combined with a ^{210}Pb and ^{14}C age-depth model to produce a flood frequency reconstruction of the last 3000 years?

- (2) Can a cleaning procedure be created to purify bulk tephra samples? Can tephra layers in five Cajas National Park lakes (Laguna Llaviucu, Riñoncocha, Fondococha and Estrellascocha) be correlated to each other by geochemical fingerprinting and absolutely dated with the goal to establish a regional tephrochronology?
- (3) Can the effects of the fish hatchery in L. Llaviucu be traced in the sediment? How did the lake recover since the activities stopped and the area was turned into a protected national park? What can analytical studies tell us about environmental change?

1.3 Project design

- (1) **Retrieval of new cores.** Six sediment cores were already retrieved in the 2014 field campaign. Eleven extra cores were retrieved in the 2015 campaign from the original lakes (L. Llaviucu, Fondococha and Riñoncocha) as well as one new lake, L. Estrellascocha.
- (2) **Establishment of the chronology.** Sediment cores were dated using high resolution ^{210}Pb measurements and numerous ^{14}C dating on macrofossils.
- (3) **Conceptualization and realization of the tephra cleaning procedure.** Tephra layers were identified through scanning techniques and microscope analysis and subsampled. A method to thoroughly purify the bulk tephra samples using a step cleaning procedure involving density separation was conceptualized and carried out.
- (4) **Geochemical fingerprinting of the tephra.** The purified bulk tephra samples were totally dissolved by microwave digestion and measured in the ICP-MS for major, minor and trace elements. Statistical methods such as principal component analysis, cluster analysis and similarity coefficients were used to correlate the tephra layers. Geochemical data were visualized with x-y biplots, elemental ratios and line plots.
- (5) **Analytical analysis of sediment properties.** L. Llaviucu sediment cores were subsampled for total nitrogen, total organic carbon, $\delta^{15}\text{N}$ and $\delta^{13}\text{C}$ in order to assess the impact of the fishery as well as any other environmental changes which would be revealed.
- (6) **Classification of flood layers.** Different visual and scanning techniques such as XRF and hyperspectral imaging were employed to classify the flood layers present in the sediment of L. Llaviucu. This reconstruction was then combined with the age-depth model produced in (2) to present a new flood frequency record.
- (7) **Interpretation and project unification.**

1.4 Project outline

This thesis begins with the present introduction (**Chapter 1**) which highlights the current gaps in knowledge as well as the research goals of this project. **Chapter 2** provides a site description of Cajas National Park and especially Laguna Llaviucu since the environmental and flood layer reconstructions were undertaken at this location. **Chapter 3** provides a literature review on tephrochronology in order to support the conceptualization of the tephra cleaning procedure. This is followed by three substantial methodology sections for the tephrochronology, flood classification and environmental reconstructions (**Chapter 4**). The results of the analyses are

reported in **Chapter 5**. The results are followed by their interpretation in the discussion (**Chapter 6**). Finally, **Chapter 7** brings the reader to some conclusions drawn and identifies whether the research questions were answered.

2 Study Site

2.1 Cajas National Park in Ecuador

Ecuador, a small (283,561 km²; CIA, 2014) western equatorial South American country, is both climatologically and volcanologically interesting amongst others. The country is divided into three regions: el Oriente to the east, la Sierra or the Andean cordillera in the centre and la Costa to the west (CIA, 2014). The Andes in Ecuador consist of two ridges, the western and central Cordillera, with a high elevation plateau in between. The eastern Cordillera is much less pronounced (Buytaert et al., 2006). Natural hazards are rife in Ecuador in the low and high altitudes ranging from devastating floods and landslides brought by El Niño Southern Oscillation (Comunidad Andina, 2009; Vos et al., 1999) to volcanic eruptions and earthquakes (CIA, 2014). The site of investigation is located 35 km west from Cuenca in south central Ecuador on the occidental Cordillera. Cajas National Park (CNP; 2° 50' 0" S, 79° 10' 0" W) consists of 285 km² of protected land since 1977 containing over 200 lakes ranging in altitude from 3152 to 4445 m a.s.l (ECOLAP and MAE 2007, **Fig. 2-1**). The landscape above 3500 m was sculpted by glacial action, leaving behind numerous U-shaped valleys, moraines and paternoster lakes (Goodman, 1996 as read in Hansen et al. 2003).

2.2 Volcanic landscape

The avenue of volcanoes spans the northern section of the Ecuadorian Cordillera with 22 volcanoes of Holocene age of which 10 have recorded historical eruptions (Brown et al. 2015, **Fig. 2-2**). Volcanism on the mainland is related to the Nazca Plate sub-ducting beneath the South American Plate (Brown et al., 2015). Large volcanic eruptions from felsic to andesitic stratovolcanoes have occurred in the recent past from most of Ecuador's active volcanoes causing widespread damage (Brown et al., 2015; Comunidad Andina, 2009). Past volcanic eruptions are often collected into databases but few contain information on Ecuadorian volcanoes as most volcanological information is contained within "grey literature" difficult to access (Brown et al., 2015). The Smithsonian Institution (Venzke, 2016) and the Volcano Global Risk Identification and Analysis Project (Croweller et al., 2009) are rare examples containing ages and some citations for reference.

CNP is located 110-130 km away from the closest volcanoes (Tungurahua or Sangay) in a 1600 km section devoid of volcanic activity so is not at immediate risk of volcanic eruptions (Brown et al., 2015; Buytaert et al., 2006; Monzier et al., 1999). Not all eruptions can produce tephra that reaches southern Ecuador. For example, Hall and Mothes (2007) have defined the geochemical signature for several Cotopaxi eruptions, some of which may have occurred in the last 2000 years. However, Biass and Bonadonna (2013) modelled the plausible tephra fall-out from Cotopaxi, none of which reach the southern region. The three volcanoes most likely to affect CNP are Tungurahua, Sangay and Quilotoa which are located on the southern edge of the Carnegie ridge (Barberi et al., 1988) also known as the Andean Northern Volcanic Zone (Monzier et al., 1999). As a result of their distance, the amount of ash likely to be deposited in CNP is small and the grain-size likely to be fine (Buytaert et al., 2006). Geochemical analyses of major elements have been produced for Tungurahua (Hall et al., 1999), Quilotoa (Mothes and Hall, 1998; Stewart and Castro, 2016) and Sangay (Monzier et al., 1999) ash deposits.

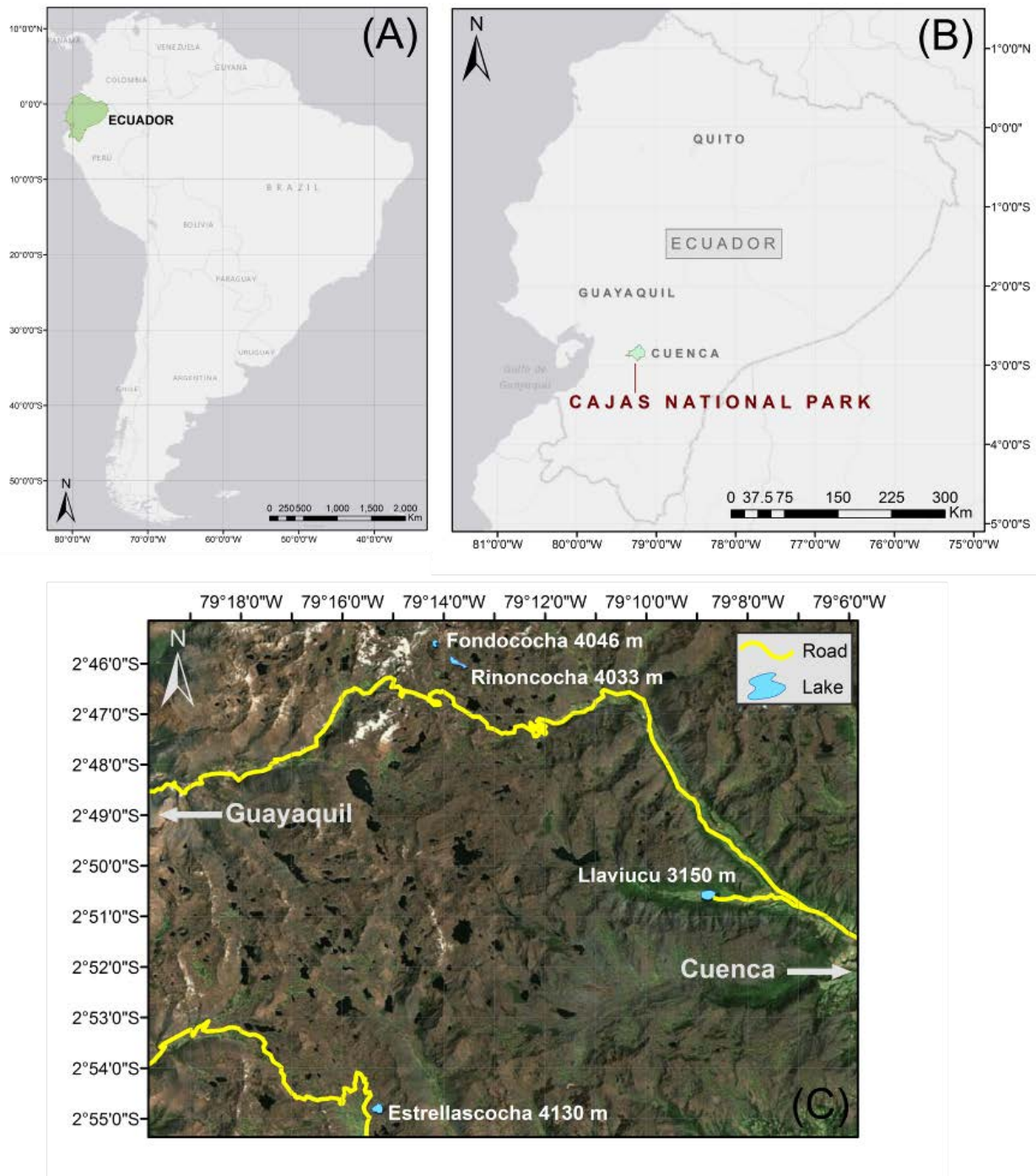


Fig. 2-1 The location of (A) Ecuador, (B) Cajas National Park and (C) the lakes investigated in Ecuador. Basemap source: Esri, DigitalGlobe, GeoEye, Earthstar Geographics, CNES/Airbus DS, USDA, USGS, AEX, Getmapping, Aerogrid, IGN, IGP, swisstopo, and the GIS User Community.

The Cordillera Occidental consists of sedimentary and basic to intermediate volcanic deposits of Palaeocene-Eocene age emplaced in a sub-marine environment (Monzier et al., 1999). Overlying these deposits is the Tarqui Formation, the most widespread late Miocene volcanic series in southern Ecuador (Monzier et al., 1999). This formation consists of intermediate to acidic pyroclastics containing volcanic ashes often altered to dark red and purple kaolinitic clays (Monzier et al., 1999). The park sits entirely on top of these deposits and this directly influences the soils, vegetation and the trophic status of the lakes.

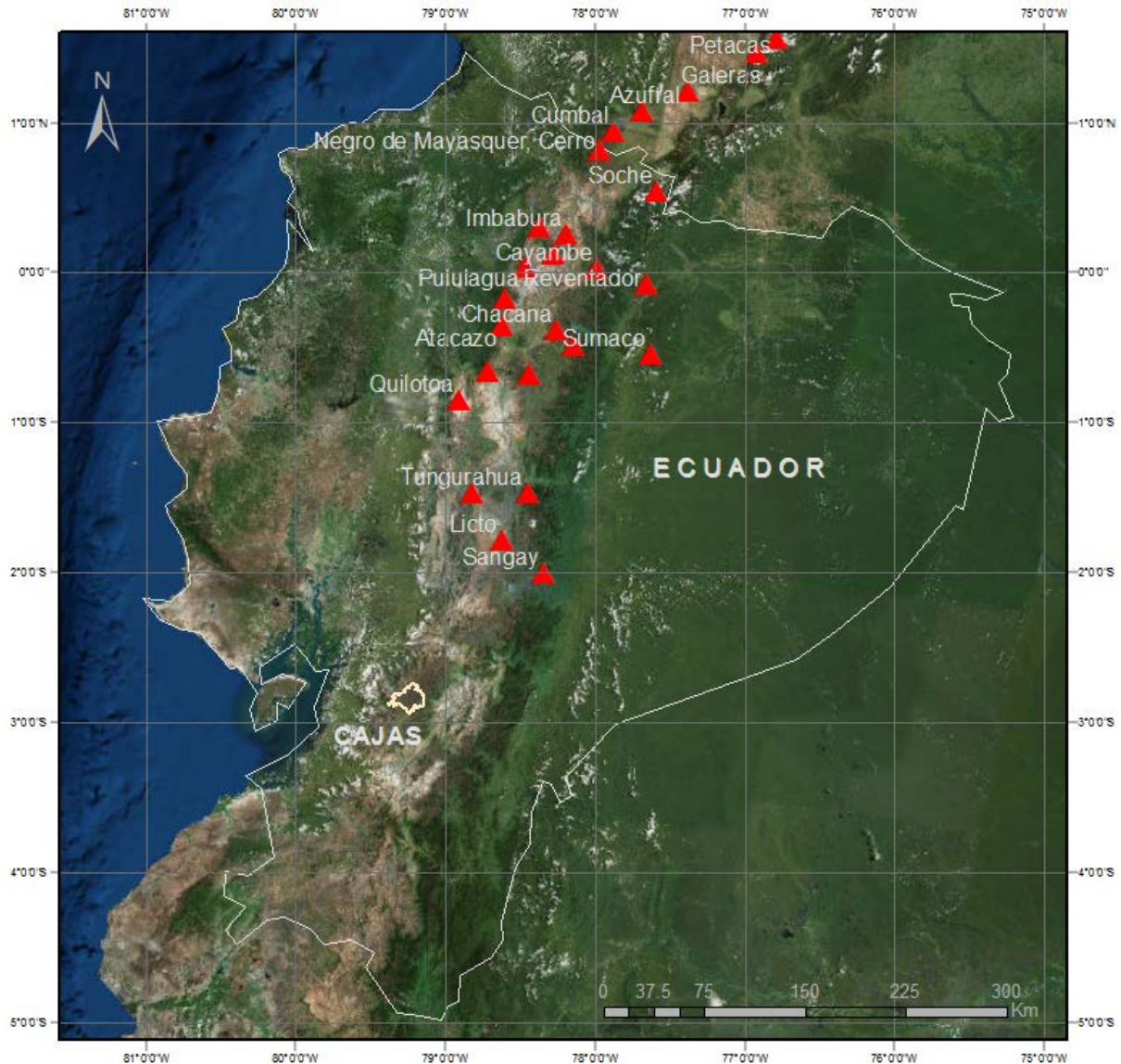


Fig. 2-2 Location of volcanoes (red triangles) in relation to Cajas National Park (yellow outline). Basemap source: Esri, DigitalGlobe, GeoEye, Earthstar Geographics, CNES/Airbus DS, USDA, USGS, AEX, Getmapping, Aerogrid, IGN, IGP, swisstopo, and the GIS User Community.

2.3 Climatic influences

The climate of Ecuador is influenced by atmospheric variability including El Niño Southern Oscillation (ENSO), Pacific Decadal Oscillation (PDO), the migration of the Intertropical Convergence Zone (ITCZ) and the South American Summer Monsoon (SASM). Each influences different locations by varying amounts but ENSO is the main pattern of variability (Morán-Tejeda et al., 2016; Vuille et al., 2000a). The climatic influences on the inter-Andean corridor are particularly difficult to assess due to the complex terrain of this mountainous region (Morán-Tejeda et al., 2016; Vuille et al., 2000a). Based on studies from southern Ecuador, climate on the eastern cordillera is dominated by a tropical regime with strong year-round easterlies carrying moisture-laden air from the Amazon basin (Beck et al., 2008; Brunschön and Behling, 2009). The speed and frequency of the easterly trades has been shown to correlate with Pacific sea surface temperatures, especially those in the El Niño 3.4 region (Emck, 2007; Morán-Tejeda et al., 2016).

However, during La Nina events, the westerlies can intrude further inland due to weakening easterly winds (Emck, 2007). Further support to this east-west divide comes from strontium-90 deposition after nuclear weapon testing in the 1950s. French (1960) found highest values on the eastern base of the Ecuadorian cordillera indicating an eastern movement of moisture. Studies from Rodbell et al. (1999) and Moy et al. (2002) have inferred the opposite mechanism from flood layer deposits.

The climate of CNP between 2800-3900 m a.s.l. has been described as cold and humid with temperatures varying daily between -2 and 18 °C and precipitation varying seasonally between 1000-2000 mm based on local weather stations (ECOLAP and MAE, 2007). Like other tropical regions, seasons at CNP are defined on precipitation rather than temperature as the latter varies minimally over the course of the year (Morán-Tejeda et al., 2016). Two peaks in seasonal rainfall are identified (Barros and Carrasco 2006) but this is likely to be modulated by an overlap of ENSO and PDO (Morán-Tejeda et al., 2016). The average precipitation in the páramo of the Andes according to Morán-Tejeda et al. (2016) is 900 mm which is far below that measured for CNP highlighting the influence of micro-topography. This abundance of rainfall which often takes the form of fog (Emck, 2007) augments the water available to the páramo and for the nearby town of Cuenca.

2.4 Lake systems

The lakes investigated in this study are relatively young glacial lakes from the last deglaciation 17-15 ka BP formed in cirques and U-shaped valleys (Barros and Carrasco 2006). Some, for example Laguna Llaviucu, were formed by damming from a terminal moraine (Hansen et al., 2003). Most of the higher altitude lakes investigated are located above 3500m within the páramo to sub-páramo, high altitude neotropical grassland ecosystems (Buytaert et al., 2006; Colinvaux et al., 1997). Laguna Llaviucu, also known as Surucucho, is the only relatively low altitude lake surrounded by high montane evergreen forest (ECOLAP and MAE, 2007). As a direct result of the type of surrounding vegetation, the lakes with the exception of Llaviucu receive very little terrestrial vegetation input. All the lakes with the exception of Laguna Llaviucu which is meso-trophic, are oligotrophic with very low productivity (Barros and Carrasco, 2006). Some attributes of the surrounding landscape contribute to the trophic status of the lakes. This includes hard igneous bedrock, soils with low phosphorous content, sparse vegetation as well as low temperatures and high precipitation (Cohen, 2003). In addition, the lakes are relatively untouched by human activities as the area was made into a national park and protected area in 1977 (ECOLAP and MAE, 2007). Exceptions include mining near Estrellascocha, the introduction of fish in most lakes and pedestrian access by hikers and horses to all the lakes. Few of the lakes considered here have been investigated previously. Details of each lake can be found in **Table 2-1**.

Table 2-1 Information on the lakes used in this study. ¹ Barros and Carrasco (2006) ² (Hansen et al. 2003) ³Google Earth (2015) ⁴Own measurements.

Lake	Location	Altitude (m.a.s.l)	Max Depth (m)	Trophic state	Formation	System
Llaviucu	02°50'34.71"S 79°08'46.01"W	3140 ¹	16.5 ⁴	Meso-trophic	Glacial terminal moraine (15-20 kya) ¹	Open [In : Rio Taitachugo ; out : Rio Llaviucu] ¹
Riñoncocha	02°45'57.9"S 79°13'48.5"W	4035 ³	29.6 ⁴	Oligo-trophic		Open with sub-surface outlet
Fondococha	02°45'33.9"S 79°14'11.1"W	4133 ³	9.9 ⁴	Oligo-trophic		Open
Estrellascocha	02°51'07.6"S 79°20'30.8"W	4130 ⁴	41.6 ⁴	Oligo-trophic	Glacial cirque ⁴	Open

2.5 Vegetation at CNP

The vegetation in CNP consists of a gradient from montane forest to páramo disturbed in patches by pastoral grasslands and eucalyptus plantations (Hansen et al., 2003). The páramo is a neotropical alpine ecosystem providing important ecosystem services to towns such as Cuenca (Buytaert et al., 2006). The vegetation is dominated by tussock grass species and xeromorphic herbs with a high number of endemic species (Buytaert et al., 2007) (**Fig. 2-3**). Hansen et al. (2003) identified low growing cushion plants (*Azorella* and *Werneria*) as well as forbs (*Chrysactinium*, *Draba*, *Gentiana*, *Halenia*, *Lysipomia* and *Orithrophium*) and pteridophytes (*Asplenium*, *Huperzia*, *Lycopodium* and *Thelypteris*). Vegetation cover is less dense than lower down. Between 3500-4100 m a.s.l. is a sub-páramo ecosystem where bunch grasses (*Calamagrostis* and *Festuca*) associated with small herbaceous plants (Asteraceae, Alstroemeriaceae, Scrophulariaceae, Apicaceae and Gentianaceae) and small woody plants can be found (Hansen et al., 2003) (**Fig. 2-4**). Poorly-drained sites are also found but these contain bog and wetland species (Hansen et al., 2003). The timberline is located at around 3800 m where forest patches are dominated by *Polylepis sp.* and *Gynoxys sp.* (Hansen et al., 2003). Below 3500 m a.s.l. and particularly well visible around Laguna Llaviucu are the remnants of moist Andean montane forest consisting of *Cornus peruviana*, *Meliosma sp.*, *Myrcianthes sp.*, *Urtica sp.* and others (Colinvaux et al., 1997; Hansen et al., 2003) (**Fig. 2-5**).



Fig. 2-3 Páramo landscape around Laguna Pallcacocha. Photo credit: W. Tylmann.



Fig. 2-4 Sub-páramo ecosystem in the direction of Laguna Riñoncocha. Photo credits: W. Tylmann.



Fig. 2-5 Montane forest and pastoral grassland in the valley of Laguna Llaviucu. Photo credit: W. Tylmann.

2.6 Soils in Cajas

Soils of the southern páramo of Ecuador have been seldom described but two studies exist from the Rio Paute basin which is close to CNP (Buytaert et al., 2006). Soils there have been described as very dark and humic, containing small amounts of volcanic ash and large amounts of organic carbon (up to 44%) making them globally significant carbon sinks (Buytaert et al., 2007, 2006). Organic carbon sequestration is enhanced by the low redox potential due to the high water content and wet climate (Buytaert et al., 2006). The soils are categorized as Histic Andosols and Dystic Histosols devoid of allophane, a widely distributed aluminium silicate clay mineral associated with the weathering of volcanic ash (Allbrook, 1985; Buytaert et al., 2007). Buytaert et al. (2007) showed a strong north-south decrease in Andic properties associated with a decrease in volcanic influence which supports the low volcanic glass content (24 - 49%) in the 2000 - 20 μm fraction range found by Buytaert et al. (2006). Soil genesis in the region is strongly influenced by geomorphology, limited Holocenic volcanic ash deposit as well as the cold and wet climate (Buytaert et al., 2007, 2006).

2.7 Anthropogenic Impact

The impact of human activities on CNP is longstanding. In a pollen record from Laguna Chorreras, Hansen et al. (2003) found evidence that sometime after 7500 cal. yr BP disturbances and weed pollen (*Ambrosia*, *Chenopodiaceae*, *Dadonaea* and *Alnus*) began to appear. Pollen grains of *Zea mays* were also found pointing to regional agriculture. Without a doubt, early settlers began farming and clearing forests after 2000 cal. yr BP (Hansen et al., 2003) as this is also coincident with the presence of an “Inca road” of sophisticated construction near to Laguna Llaviucu (Colinvaux et al., 1997; Sarmiento, 2002). Fast forward two millennia and the páramo ecosystem of CNP is put under protection in 1977 as its importance for water provision is

recognized (ECOLAP and MAE, 2007). However, certain activities such as the fishing industry (see below), mining and small scale agriculture have been continuing. Up until 2009, the mining industry exploited up to 29.7% of the area of the park of Macizo del Cajas which is the greater páramo area including CNP (Velastegui, 2010). Nearby lakes such as Laguna Estrellascocha may have been affected by the mining activities but information is lacking.

2.7.1 The fishing industry

In 1951 began the process of stocking trout in high Andean lakes of Ecuador (Bondad-Reantaso, 2007). From 1978 to 1998 intensive caged fisheries activity moved to L. Llaviucu and in two decades an estimated 15.6 million fish (possibly *Oncorhynchus mykiss* or rainbow trout) were raised. From fish size and cage quantity details provided in Barros and Carrasco (2006) (Table 2-2) a yearly tonnage of 2.65 could be calculated. According to Pauly (1993) it is possible to calculate fish weight from its length through a length-weight relationship as follows:

$$W = a L^b \quad (1)$$

Where **W** is the weight (kg), **L** is the length (cm), **b** is a coefficient factor relating to this relationship in fish species and **a** is a species specific coefficient. Specifically for CNP, the fish species *Oncorhynchus mykiss* or rainbow trout was used as it is the most likely (Bondad-Reantaso, 2007). Minimum reproducing size was estimated to be 14.8 cm (as the average of 13.40 cm for males and 16.25 cm for females according to Bastardo 1994). The coefficients **a** and **b** were taken to be 0.01 and 3.02 respectively after data from FishBase (Froese and Pauly, 2016). Quantity data were taken from Table 2-2 below.

Table 2-2 Fish cage data from Paúl Turcotte in Barros and Carrasco (2006).

Quantity	Cage size (m)	Fish size (cm)	Estimated quantity
12	6X6	Reproducing	530
1	3.65x3.65	Reproducing	250
6	3x1	5 a 10	30000
2	3x1	10	10000
9	3.65x3.65	5 a 10	90000
6	Hexagonal length 6 m	20 a 25	60000
1	Hexagonal length 6 m	15 a 20	10000
4	Hexagonal length 6 m	10 a 15	40000
1	6x6	20 a 25	10000

As L. Llaviucu provides nearly 20% of the water supply for the 332,000 inhabitants of Cuenca, concerns were raised on the water quality. From 1995 onwards, monitoring of the lake as well as the in- and out-flow rivers (Rio Taitachugo and Rio Llaviucu) was carried out by ETAPA (Barros and Carrasco, 2006). By 1998 the First Chamber of the Constitutional Court ruled against the fisheries activity as it was found that the water quality had deteriorated. The impact source on the water was manifold: faecal matter from the fish population, algal growth on the cages and slaughtering wastes all worked to change the lake's trophic status from mesotrophic to eutrophic in the course of 20 years (Barros and Carrasco, 2006). Once the activity ceased completely in 1999, the lake quickly began to restore itself as its turnover rate is unusually fast (17 days) (Barros and Carrasco, 2006). By the 2000's the lake had returned to an oligo-mesotrophic state.

3 Tephra in the literature

3.1 Background

Absolute dating of lake sediment cores is not always possible. In high altitude lakes in the páramo of Ecuador the paucity of terrestrial plant macrofossils and the likelihood of reservoir effects hinders the potential for radiocarbon dating. Furthermore, dating using ^{210}Pb is restricted to the last 100 - 120 years and must be validated by independent time markers (Putyrskaya et al., 2015). Event markers such as dated volcanic eruptions are ideal to overcome these difficulties.

The Ecuador project will bring together a multitude of proxies from seven different lakes (L. Riñoncocha, L. Fondocochoa, L. Estrellascocha, L. Pallcacocha, L. Burrines, L. Jiheno and L. Llaviucu), three of which are located at approximately 4000 m a.s.l. in grassland/páramo landscape and one, Llaviucu, at much lower altitude in a vegetated zone. Being in a semi-forested area, Llaviucu is expected to yield more macrofossils from terrestrial plants than the other lakes. As such, this lake will be crucial for dating compared to the others where the paucity of macrofossils is an issue. Tephrochronology here provides a unique solution to the problem. By identifying tephra layers in all cores either visible with the naked eye or hidden as cryptotephra, all cores can potentially be correlated. In addition, radiocarbon dating of the layers above and below the tephra horizon will constrain their ages and can then be applied to the other lakes. The major objective of using tephrochronology in this project is to correlate the cores from the different lakes (Laguna Llaviucu, Fondocochoa, Riñoncocha and Estrellascocha) and to assign radiocarbon ages to each of the layers. The secondary aim is to link the layers to known eruptions.

Few tephrochronology studies have been undertaken in Ecuador at regional and temporal scales of interest for this study. One study looked at several lakes in Cajas National Park, including Llaviucu and Pallcacocha (Rodbell et al., 2002). However, the authors only found two tephra layers in the last 3000 years at 250 and 550 B.C.E. The authors only concentrated on visible tephra layers and did not attempt to investigate cryptotephra. Since Ecuador is located in a volcanically active region home to several large volcanoes (e.g. Sangay, Quilotoa, Cotopaxi, Tungurahua for example) the paucity of tephra in Rodbell et al. (2002) for the last 3,000 years is surprising. Visible determination is rapid and easy but the addition of cryptotephra would yield more comprehensive results. In the context of this project several tie points within the timespan of the cores are needed for a more robust correlation.

3.2 Tephrochronology

Tephra has been studied for many decades once its use as chronological marker and absolute dating potential was realized (Lowe, 2011). Cryptotephra or hidden tephra on the other hand is a recent revolution in the field of tephrochronology (Davies, 2015; Lowe, 2011). Using both provides the best chance of correlating between cores.

3.2.1 Tephra layer identification by scanning

Non-destructive and destructive methods have been used to identify tephra layers (Gehrels et

al., 2008). Reflectance spectroscopy, X-ray fluorescence (XRF), magnetic susceptibility (MS) and gamma density are all fast, inexpensive scanning methods yielding very high spatial resolution data. However, work by Gehrels et al. (2008) demonstrated a lower detection rate of tephra than with traditional destructive methods. Of the possible methods, XRF has the highest potential for cryptotephra detection although the combination of diagnostic elements may vary from core to core (Davies et al., 2015). For alkaline cryptotephra, Nb might be the most useful diagnostic element according to Lim et al. (2008). On the other hand, reflectance spectroscopy shows high noise ratios while density and magnetic susceptibility can be influenced by other sediment properties unrelated to tephra (Gehrels et al., 2008). Hyperspectral scanning methods have not been used to locate tephra. Visual inspection combined with smear slides for light microscopy analysis might still be the best method for detection. A combination of all the above techniques might be useful to form a preliminary idea of where tephra might be found. However, in the end the occurrence of tephra can only be confirmed through destructive methods.

3.2.2 Tephra identification by core sub-sampling

Sampling for tephra must follow a contiguous strategy since tephra fall-outs are discreet events in time (Lowe, 2011). Any other strategy might result in missed events. An adequate strategy might be to sample at 5 cm resolution throughout the core while sampling visible tephra layers separately. The coarse resolution can then be refined to narrow down on the location of tephra. Microscopic inspection of smear slides using light reflectance and potentially scanning electron microscope (SEM) is based on the visual discrimination of tephra. Glass shards which are non-crystalline and isotropic become black under polarised light when using both analysers (Lowe, 2011). On this basis, tephra may be identified and the sampling refined. Automated identification has also been attempted using FlowCAM photographs of the particles in suspension but was found to be inappropriate for morphologies outside the range of the reference library as may be the case for Ecuadorian tephra (D'Anjou et al., 2014).

3.2.3 Tephra glass shard purification

Sample preparation involves removing organic matter through ashing or hydrogen peroxide. Ashing combines combusting the organics at high temperature (600°C) for 4 hours and using weak acids to disintegrate the burned material. Loss on ignition (LOI), as a measure of organic versus inorganic content can be measured as part of the ashing treatment (Gehrels et al., 2008). However, the samples are then unusable for the geochemical analysis (Roland et al., 2015). On the contrary, hydrogen peroxide oxidation has not been found to alter the composition of shards. Rodbell et al. (2002) treated samples with 30 mL 30% H₂O₂ and sieved the material using a 75 µm sieve before using for geochemical analysis. Placzek et al. (2009) prepared their samples for both count and geochemical analysis by treating with 2M HCl to remove carbonates, rinsing in 2% HF very briefly and washing in distilled water. The samples were then sieved into >120 µm, 60 – 120 µm, and <60 µm size fractions.

Although much faster, the acid wash method of Placzek et al. (2009) involves the use of several dangerous chemicals. Furthermore, a question on whether the acids alter the geochemical composition has recently emerged (Blockley et al., 2005). Blockley et al. (2005) found an alteration of glass shards at varying rates when exposed to acid, neutral and alkali environments. Most notably, they found an average shard loss of 65 ± 9% for samples treated with NaOH to remove biogenic silica. Conversely, Roland et al. (2015) have investigated the

matter using peat sediments and found no significant differences. Rea et al. (2012) made the point of following the most used procedure to allow for comparison with geochemical data held by TephraBase (Newton et al., 2007). Ideally, heavy liquid separation using non-toxic sodium polytungstate (SPT) following the method by Turney (1998) and subsequently improved by (Blockley et al., 2005) could be used. The liquid is prepared to have a known density of 2.0 gcm⁻³ in a first round, followed by 2.5 gcm⁻³ in the second float (Blockley et al., 2005) which would mean the tephra would sink while other sediments and organic matter would float and be removed. However, settling is a time consuming process. Furthermore, some tephra compositions might be lighter than the determined heavy liquid density (Gehrels et al., 2008). More crucially, heavy liquid separation does not recover the heavy basaltic tephra (Mackie et al., 2002). This may be biasing the geochemical fingerprint if this density fraction is important.

In order to recover the basaltic fraction, the use of a magnetic separator has been investigated initially by Nelson et al. (1985) then by Mackie et al. (2002). They ashed 1 cm³ samples at 550°C to enhance the magnetic susceptibility even though high heat has been shown to alter geochemistry (Gehrels et al., 2008; Roland et al., 2015). They then exploited the magnetic affinities of the basaltic material to separate the material from other minerals still present in the heavy fraction (Mackie *et al.*, 2002). Pearce et al. (2004) used a hand magnet and a magnetic separator to remove ferro-magnesian minerals and grains containing magnetite from the glass shards. Other papers mention the use of magnetic separation without explicit detail (e.g. Eden et al. 1992).

3.2.4 Tephra morphology

Tephra morphological determination has been employed as a correlation tool. Tephra occurs in several forms including pumice, scoria fragments, glass shards and crystal and lithic fragments (Daga et al., 2010) representing different stages of the eruption as well as distance (Pearce et al., 2004). Sieving with different mesh sizes (e.g. >500 µm, 500 - 250 µm, 250 - 125 µm, 125 - 63 µm and <63 µm) is recommended to find all the different types once organics are removed (Daga et al., 2010). Three morphological types of glass shards have been put forward including bubble walled (cusped), platy and pumiceous/inflated (Lowe, 2011). Classification schemes have been developed by Nelson et al. (1985), Katoh et al. (2000) and Liu et al. (2015) (see **Fig. 3-1** for example). Characterizing tephra through physical, textural, morphological and vesicular appearance may be indicative of the source volcano even without geochemical analysis. Classification and photographs of tephra may be done while counting.

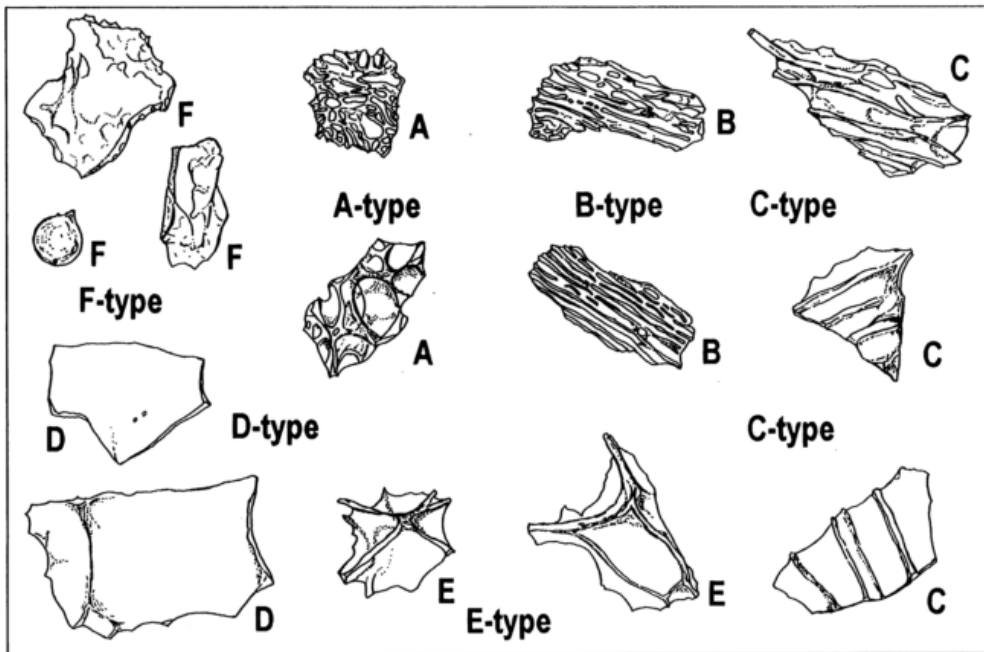


Fig. 3-1 Descriptive terminology for microscopic tephra classification. From Katoh et al. (2000).

3.2.5 Tephra concentration

Concentration can be recorded as the number of shards counted using a polarizing microscope and point counter in a set volume of wet sediment (per cm³) or weight of dry sediment (per g). Up to 3,000 grain counts are necessary to be representative (Lowe, 2011). A faster method borrowed from palynology would be to spike the prepared sample with one tablet of *Lycopodium* with a known concentration of spores. A homogenised drop of sample is mounted on a microscopic slide and 200 spores are counted alongside the tephra shards. The concentration relative to dry weight is then calculated using the formula (Gehrels et al., 2008):

$$C = l * (a/b * d) \quad (2)$$

where *a* is glass shard count, *b* is *Lycopodium* spore count, *d* is sample dry weight in milligrams, and *l* is the number of *Lycopodium* spores in the tablet added to the sample. This technique has the advantage of being relatively fast while not reducing the accuracy significantly (Lowe, 2011). Results are then plotted on a depth versus concentration graph to visualise the data (Ramsey et al., 2015).

The concentration of tephra even at deposition sites of close proximity is not expected to be similar due to differing conditions during deposition (Rea et al., 2012). Factors such as altitude, prevailing wind and precipitation patterns may all affect the process (Rea et al., 2012). Non-conformity between sites is an indication for local reworking (Lowe, 2011). Reworked tephra form diachronous surfaces comprising of the primary deposit, the non-reworked part of the deposit which yields a maximum age, and the secondary deposit which is always younger (Lowe, 2011). Reworking can be demonstrated by looking at the tephra. Partial rounding and loss of glassy coating may point to reworking (Lowe, 2011). In addition, understanding tephra dispersion patterns is crucial for correlation (Rea et al., 2012).

3.2.6 Preparation for geochemical fingerprinting

Geochemical analysis is used to determine the elemental composition of a material to the degree of 10-13 major components (Si, Al, Ti, Fe, Mn, Ca, Na, K, P, S, F and Cl) (Lowe, 2011), trace elements (Ba, Ce, Sr, Rb and Nb) (Pearce et al., 2007) and rare earth elements (REE). In a first step the different types of tephra must be separated. For correlation purposes, the glass fraction has been identified as most reliable as it represents the magma composition at the time of the eruption and does not alter with distance from the source (Daga et al., 2010). Pumice on the other hand, gives information on the mixing of volcanic sources (Daga et al., 2010). Two procedures are possible: bulk chemical assay (e.g. Eastwood et al. 1999) or single grain analysis (e.g. Rea et al. 2012) and each method require a different preparation technique.

For bulk chemical assay acid digestion is used. Preparation of the sample may follow the TephraBase (Newton et al., 2007) standard procedure based on Persson (1971) which according to Dugmore and Newton (1995) does not alter the geochemistry of the shards. If ashing was used to remove organics, fresh samples must be prepared as the very high temperatures (>350°C) alters the geochemical composition through potassium uptake (Gehrels et al. 2008; Roland et al. 2015). Pearce et al. (2004) designed a method specifically for the use of an inductively-coupled mass-spectrometer (ICP-MS). A sample of 0.5 g is added to a beaker with two millimetres of HCl and left to stand cold for 15 h before evaporation to dryness which dissolves any Fe oxides still present. A mixture of 15 ml HF and 4 ml HClO₄ is added to the beaker when the solution is cold and once again evaporated to dryness. More HF/ HClO₄ may be added if the sample is not completely dissolved. The soluble residue is taken into solution in 100 ml of 5% HNO₃ further diluted to a maximum of 0.2% total dissolved solids (TDS). The sample should be spiked with a known concentration (e.g. 100 µg l⁻¹ of one element such as Ru; Pearce et al., 2004).

The preparation method differs if single grains are to be analysed. Statistically, more than 50 grains should be picked out for heterogeneous samples (Lowe, 2011) although some studies have used less (see Rodbell et al. 2002). The selected shards are placed in thin-section epoxy on a petrographic slide, and polished using a diamond plate (Kuehn and Froese, 2010). The use of single grain analysis has superseded bulk chemical assay as the latter is easily affected by mineral inclusions and impurities (Alloway et al., 2013; Lowe, 2011; Pearce et al., 2007; Shane, 2000).

3.2.7 Geochemical fingerprinting

The geochemical fingerprinting method depends on the preparation. If analysis is done on single grains then electron micro-probe analysis (EMPA) may be used to measure major elements. EMPA works by directing a focused beam of electrons onto a sample, generating X-rays of particular energy and wavelengths relating to the elemental composition. The intensity of the rays is a measure of the specific element abundance. Primary and secondary standards must be regularly assessed (Lowe, 2011) and calibrated using Lipari obsidian for example and synthetic oxides (Rea et al., 2012). Importantly is to minimize sodium migration by adjusting the settings accordingly (Roland et al., 2015) and by analysing sodium first and several times during the procedure (Hayward, 2012). Lowe (2011) and Pearce et al. (2004) indicates bulk samples are not useful here due to the presence of variable phenocrysts and detrital material.

Major elements may not be sufficient to discriminate between volcanoes especially those of andesitic and rhyolitic compositions due to the multiplicity of eruptive units and paucity of suitable glass (Lowe, 2011; Pearce et al., 2007). Trace elements are thus necessary to discriminate between similar volcanoes (Tomlinson et al., 2010) since they represent small scale magma variations resulting from a combination of fractional crystallisation of mineral phases causing local composition variations (Pearce et al., 2007). Trace elements are analysed using inductively coupled plasma mass-spectrometers (ICP-MS) with laser ablation (Pearce et al., 2004). Pearce et al. (2007) recommend using larger shards (>20 μm) and not thin ones. The advantage of LA-ICP-MS following EMPA is that the prepared samples can be used for both (Lowe, 2011).

However, single grain analysis is time consuming and restricted to larger shards so ICP-MS “wet” analysis on bulk samples by solution nebulisation can provide accurate data for samples as small as 0.025g (Pearce et al., 2004). Solution analyses on bulk samples are slightly more accurate than LA-ICP-MS to $\pm 5\%$ and have higher precisions for abundant trace elements (e.g. Zr and Rb) which deteriorates significantly for rare elements in small samples (e.g. HREE) (Pearce et al., 2004). In addition, ICP on bulk samples is subject to fewer calibration issues than LA-ICP-MS due to elemental fractionation (Tomlinson et al., 2010) and offers quantitative results through a single line calibration (Rüdel et al., 2011). For this procedure, the prepared samples must be digested and diluted for analysis (Pearce et al. 2004 see section 2.6). The sample is then ionised and drawn into the mass spectrometer. Other methods have been proposed such as instrumental neutron activation analysis (INAA) (Lim et al., 2008) which has not been shown to provide any advantages compared to the above methods.

3.2.8 Statistical analysis of geochemical data

There are two analyses possible from the results of geochemical analysis. Firstly, the described layers can be used to correlate between the cores. The compositions should be the same in all lakes. Correlation between layers can be done using the similarity coefficient (SC) with a range of 0 to 1 where 1 is a perfect match in both the mean and the standard deviation (Borchardt et al., 1972; Rodbell et al., 2002). Maximum SC is calculated to evaluate heterogeneity of the tephra even though they should be identical between the lakes (Rodbell et al., 2002). Graphical representations of the compositions may also be useful. Datasets from EMPA are often plotted as x-y biplots of Total Alkali-Silica (TAS) (Ramsey et al., 2015; Vogel et al., 2009). The major oxides include TiO_2 , Al_2O_3 , FeO_x , MnO , MgO , CaO , Na_2O and K_2O (Ramsey et al., 2015) and are calculated from the weight percent. In the final product, stratigraphy should always be respected.

In a second step the results dataset known as the candidate is tested against a reference dataset known to be associated to a particular eruption and available from various online databases (e.g. TephraBase) (Ramsey et al., 2015). In this case, the candidate dataset is often filtered for outliers as well as low oxide totals below a typical threshold of <95% (Roland et al., 2015). However, high oxide totals are not always available in sufficient numbers due to taphonomic, analytical and volcanic processes (Roland et al., 2015). In North America and New Zealand, datasets are usually normalised to remove the effect of shard hydration but this may mask data quality and is based on unproven assumptions (Pollard et al., 2006; Roland et al., 2015). This practice is not usually found in Europe (Ramsey et al., 2015). Testing the candidate against the reference is done through numerical methods. Statistical procedures such as unnormalised multivariate normal and kernel density distribution t-test comparisons, principal

component analysis and ellipsoidal matrix were used by Roland et al. (2015). Similarly, Lowe (2011) proposed SC and coefficients of variation followed by single linkage clustering.

4 Methods

4.1 Fieldwork

Two field campaigns took place in July 2014 and 2015 of which the author took part in the latter. The campaigns consisted of the recovery of several lake cores, the installation and retrieval of sediment traps and thermistors as well as the collection of algae samples.

4.1.1 Lake sediment cores

Whole lake sediment cores were retrieved from the deepest point of Laguna Llaviucu, Pallcacocha, Fondococha and Riñoncocha using a gravitational UWITEC-corer® (Schultze and Niederreiter, 1990) (diameter 6.3 cm) with weights and a hammer in summer 2014. During the second field campaign in 2015 both whole and previously split cores were collected from the lakes mentioned above as well as Laguna Jiheno, Estrellascocha and Burrines Grande. Specifics of the core lengths and locations can be found in **Table 4-1**. Whole cores were sent back to Switzerland in a non-refrigerated container both years. The voyage back lasted between one and three weeks. The split cores were opened at the University of Cuenca Environmental Laboratory, Ecuador in order to collect extra material for tephra and radiocarbon analysis.

Table 4-1 Coring locations and core lengths used in this study. Cores from Burrines Grande, Pallcacocha and Jiheno which were not used in this study are not described.

Lake	Core Name	Location	Length (m)	Water depth (m)
Fondococha	FON-14-1	2°45'36.6"S 79°14'11.1"W	1.37	9.8
	FON-14-2	2°45'36.6"S 79°14'11.1"W	1.25	9.8
	FON-15-3	02°45'35.7"S 79°14'11.1"W	0.86	9.9
	FON-15-5	02°45'36.2"S 79°14'10.7"W	1	9.9
Riñoncocha	RIN-14-1	2°45'57.5"S 79°13'49.0"W	1.45	29.6
	RIN-15-3	02°45'57.9"S 79°13'48.5"W	1.12	22.5
	RIN-15-4	02°45'57.9"S 79°13'48.5"W	1.19	22.5
	RIN-15-5	02°45'57.9"S 79°13'48.5"W	1	22.5
Estrellascocha	EST-15-1	02°51'07.5"S 79°20'30.6"W	0.53	41.6
	EST-15-3	02°51'08.3"S 79°20'30.7"W	0.625	40
Llaviucu	LLA-14-1	2°50'33.84"S 79°8'43.15"W	1.12	15
	LLA-14-2	2°50'33.84"S 79°8'43.15"W	1.15	15
	LLA-15-1	02°50'34.7"S 79°08'47.0"W	0.735	16.5
	LLA-15-2	02°50'34.8"S 79°08'47.0"W	0.755	16.5
	LLA-15-3	02°50'34.7"S 79°13'47.0"W	0.93	16.5
	LLA-15-4	02°50'34.7"S 79°08'47.0"W	1.04	16.5
	LLA-15-5	02°50'34.7"S 79°08'47.0"W	1.28	16.5
	LLA-15-6-I	02°50'34.8"S 79°13'47.0"W	0.855	16.5
LLA-15-6-II	02°50'34.8"S 79°13'47.0"W	1.145	16.5	

4.1.2 Sediment traps and thermistors

Automatically-rotating monthly-collecting sediment traps as well as annual traps were installed in several lakes during the 2014 campaign (see **Table 4-2**). The equipment was checked during the second campaign in 2015. The sediment collected was packed and labelled to be sent back. Formaldehyde (CH₂O) of unknown concentration was added as a fixative and bacteria inhibitor (Sarakinos et al., 2002; Tuominen et al., 1994). New collection recipients were also installed as the sediments traps will remain for a second year. All traps were anchored at 1 m above the lake bed with anchor nets and stones. All sediment traps were also fitted in 2014 with two thermistors. The first placed one meter below the water surface and the second fitted one meter above the lake bed. The location and depth details of the traps and thermistors were noted (**Table 4-2**). Data collected from sediment traps and thermistors are useful to further understand lake system processes (Cohen, 2003) and data from L. Llaviucu were particularly valuable for this study.

Table 4-2 Location and depth of sediment traps and thermistors retrieved and installed in L. Llaviucu.

Lake	Location	Sampling Depth (m)	Installation year	Equipment
Llaviucu	2°50'33.84"S 79°8'43.15"W	15	2014	Thermistors (2)
	2°50'35.2" S 79°08'46.9" W	17.1	2015	Thermistors (2)
	2°50'33.84"S 79°8'43.15"W	15	2014	Sediment trap

4.1.3 Algae collection

A 500 ml recipient of modern algae was collected by hand from the cord of the thermistor/sediment trap of Laguna Llaviucu where it formed a biofilm. It was decided to collect such algae as it would represent an annually integrated community. Formaldehyde (CH₂O) of unknown concentration was added to stop degradation as for the sediment trap samples. The algae were collected to act as a ¹⁵N and ¹³C reference values for the down-core measurements. Formaldehyde has not been shown to affect the nitrogen isotopes of aquatic organisms to a significant degree (Kaehler and Pakhomov, 2001; Sarakinos et al., 2002). Any change in ¹⁵N after preservation would be related to leaching rather than uptake as formaldehyde does not contain nitrogen (Bicknell et al., 2011; Sarakinos et al., 2002). On the other hand, many studies have shown formaldehyde fixation to have a significant impact on the ¹³C signature of marine, freshwater and terrestrial organisms (Bicknell et al., 2011; Carabel et al., 2009; Kaehler and Pakhomov, 2001; Sarakinos et al., 2002). The impact may be isotope depletion (Bicknell et al., 2011; Carabel et al., 2009; Kaehler and Pakhomov, 2001) or varies between species (Sarakinos et al., 2002) which makes it difficult to find a correction factor.

4.2 Core opening and sediment description

Unopened cores were firstly scanned using the Multi-Sensor Core Logger (MSCL) and the full procedure is described in section 4.4.1. All cores were then opened at the University of Bern, Switzerland. Once opened the cores were kept in a dark cold room at 4°C wrapped in a protective plastic film and cover in order to avoid oxidation and diagenetic biological processes.

4.2.1 Sediment description

One half from each core from each lake was described in detail using the description procedure by Schnurrenberger et al. (2003). Core length, stratigraphy, texture and colour were described using a fixed legend. Testing for carbonates using 10% Hydrochloric acid was carried out. The location of organic rich layers or plant remains was noted. Colour estimation using the Munsell® colour chart was undertaken on wet sediment. L. Llaviucu sediment cores from the 2014 and 2015 field campaigns were described in most detail. The colour of the tephra layers was also recorded using the Munsell® chart. Microscopic slides and Scanning Electron Microscope (SEM) samples were prepared for each layer which appeared to contain tephra.

4.3 Sub-sampling and sample preparation

The sub-sampling procedures differed for each technique and are described in this section. Two methods of dating were used in this study, each requiring a different approach to the sub-sampling and are described in section 4.3.1. Tephra occurs in discreet events and thus needed its own sampling strategy (section 4.3.2). Finally, samples for wet chemical analyses were also extracted differently and this is described in section 4.3.3.

4.3.1 Dating

Samples for ²¹⁰Pb dating

²¹⁰Pb dating has been widely used in young sediments as it is confined to the last 150 years due to the short half-life of the radioactive isotope (Cohen, 2003). As a result, sub-sampling was limited to the top 20 - 30 cm as this section was estimated to reach back by this time-span. Samples were cut at 0.5 cm resolution and similarly weighed while wet, then frozen, freeze-dried and re-weighed when dry. The samples were placed in tin-foil which was also weighed. The methodology of ²¹⁰Pb dating is described in more detail in section 0.

Samples for radiocarbon dating

Radiocarbon dating was attempted on both bulk and macro-fossil remains in order to estimate the occurrence of a reservoir effect. Bulk sediment from various depths in L. Llaviucu, Fondococha and Pallcacocha were sub-sampled at 0.5 - 1 cm resolution. Half of the sample was weighed when wet. The bulk samples were then frozen over-night and freeze-dried. The dry sample was then re-weighed in order to calculate the net weight and water content. The other half of the sample was sieved for macro-fossil remains. The remains were similarly weighed, frozen, freeze-dried and re-weighed. The fossils were identified under the light-microscope and only terrestrial material was selected. These included twigs, grass blades and fruit shells. Insects could in theory have been used if they could be identified as terrestrial with high certainty. Further macro-fossil samples were sieved from the three lakes in order to improve the

chronology. In addition, 1 cm resolution samples were taken from below and above each tephra layer in order to date layers with maximum accuracy. The methodology behind radiocarbon dating is described in more details in section 4.8.

4.3.2 Samples for the tephra chronology

Approximately 50 mg tephra material was needed per measurement for geochemical analysis. As a result, several split-cores were taken from each lake. The thickness of each identified layer was first measured then sub-sampled taking care not to include any over or under lying sediment to minimize the contamination. Samples from split cores from the same lakes were merged in the field after checking the stratigraphy. Measurement and sub-sampling for cryptotephra was problematic as the layer could not be seen with the naked eye. As a result, a much thicker sample had to be extracted thus containing much non-volcanic sediment possibly contaminating the sample with re-worked tephra.

Tephra pre-processing included weighing while wet, over-night freezing, freeze-drying and weighing while dry. The samples were oxidized using hydrogen peroxide (15 ml 30% H₂O₂ for at least 72 hrs and until the samples stop fizzing). In two test samples, 10% hydrochloric acid was added to remove carbonates if present. The samples did not fizz as expected so the addition of HCl was not necessary for the other samples. The samples were washed thrice with distilled water using the centrifuge at 2500 rpm for 5 minutes each time.

A SEM sample was prepared for each layer. Samples were prepared in three different manners to find the most suitable SEM sample preparation. The first method consisted of spreading material onto a carbon tape using a spatula but tephra was found to be highly electrostatic. The second method involved tapping a carbon tape with a gloved finger covered in tephra but this was found not to produce an even coverage. The third method involved the density settling of the material through a water column onto the carbon tape and this was found to yield the best although not perfect result. Hence this method was used to to prepare the samples.

4.3.3 Samples for wet chemical analysis

Sub-sampling in the sediment core for wet chemical analysis such as elemental concentrations (carbon and nitrogen) and isotopes (¹³C and ¹⁵N) was straight-forward. The top 20 cm of L. Llaviucu was sub-sampled at 0.2 mm resolution. Such high resolution was needed to assess the variability through time. The collected algae from L. Llaviucu were also processed for wet chemical analysis. In a first instance, an aliquot of the algae sample collected in the field was taken out so the algal species could be identified using the light microscope after the biofilm cells were released in distilled water by shaking (Bellinger and Sigee, 2010). The rest of the sample was first washed repeatedly under the fume hood with distilled water using a 40 µm filter to remove the formaldehyde which was used for preservation. The sample was centrifuged thrice with distilled water at 2500 rpm for 5 minutes in order to concentrate the material. The water was pipetted out and replaced to clean the sample thoroughly. All samples were then weighed wet, frozen over-night, freeze-dried and weighed while dry in order to also calculate the net weight and water content. Freezing and freeze drying were not found to significantly change ¹⁵N ratios (Bicknell et al., 2011; Kaehler and Pakhomov, 2001) and were thus considered safe methods. The samples were ground up to a fine powder using a mortar and pestle.

In order to determine the right amount of material needed for analysis, three aliquots from different depths were split into smaller aliquots of 10, 20, and 40 mg and placed in aluminium capsules. As ^{15}N and ^{13}C had to be also measured on the same samples, the weight needed to be large enough to measure the isotopes precisely. A minimum of 50 μg of nitrogen must be present in the sample for accurate measurement according to the machine manufacturer. A 16 mg weight was identified as being sufficient for the down-core measurement. With this weight, every tenth sample was triplicated to assess the measurement precision. Similarly, a test was carried out for the algae measurements and 8 mg was found to be sufficient. More details about the methods are provided in sections 0 and 4.6.

4.4 Scanning techniques

Logging techniques have been used for decades as they offer fast, quasi-continuous, non-destructive, high-resolution analyses (Birks et al., 2001; Grosjean et al., 2014; Schultheiss and Weaver, 1992). The advantages of scanning techniques include the fact that they do not involve sub-sampling, are cost effective, can be operated at sub-millimetre scale and can quickly produce long datasets. Disadvantages are few but mainly relate to the measured values not being substance specific (Grosjean et al., 2014). In addition, high resolution scanning techniques produce enormous amounts of data. Scanning techniques such as multi-sensor core logger (MSCL), visible to near-infrared spectroscopy (Specim) and X-ray fluorescence were employed to detect possible cryptotephra layers within the cores as discussed in section 4.4.3. In addition, hyperspectral scanning was employed in order to classify the occurrence of flood layers within the L. Llaviucu sediment cores. Most importantly, the scanning logs were also used to correlate between cores and design the sampling strategy for tephra.

4.4.1 Multi-Sensor Core Logger (MSCL)

The automated multi-sensor core logger (MSCL) consists of a moving tray and fixed measuring equipment including amongst others gamma ray attenuation sensor and a magnetic susceptibility loop which measures semi-continuously at a resolution of 0.5 cm (Birks et al., 2001; Croudace and Rothwell, 2015; Schultheiss and Weaver, 1992). The gamma ray attenuation sensor works by recording the intensity of gamma rays produced by a radioactive source that is mounted on the MSCL as they pass through the core (Birks et al., 2001). Along with the measurement of core thickness and the input of the Compton attenuation coefficient, the bulk density of the core can be calculated (Birks et al., 2001). Similarly, the magnetic susceptibility loop characterizes the ease with which the sediment becomes magnetized using a Bartington sensor (Birks et al., 2001; Croudace and Rothwell, 2015). Magnetic susceptibility varies with the content of ferromagnetic or iron-bearing minerals which is often a proxy for detrital material but also for tephra (Birks et al., 2001; Gehrels et al., 2008). All un-opened CNP cores were scanned with the Geotek® MSCL at the Geological Institute of the University of Bern with a resolution of 0.5 cm in order to measure magnetic susceptibility ($\text{SI} \times 10^{-5}$) and density (g cm^{-3}). MSCL data were used to isolate cryptotephra layers (see section 4.4.3) and correlated between cores.

4.4.2 μXRF

Micro X-ray fluorescence (μXRF) systems have been used for the semi-quantitative, non-destructive analysis of sediment cores. The scanner uses a medium power (2 - 3 keV) x-ray

generator with a user selected x-ray tube (Mo, Cr or Rh) to optimize the analysis. The choice of the tube determines the range of elements which can be analysed (Croudace and Rothwell, 2015). Unlike MSCL which is multi-interpretative, XRF produces data about the actual composition of the sediment (Birks et al., 2001). The most often used elements include Si, K, Ca, Ti, Fe, Rb, Sr and Zr which have been linked to various environmental proxies such as detrital material or tephra (Davies et al., 2015). The opened CNP cores were scanned with an ITRAX® (Cox Analytical System) micro x-ray fluorescence (μ XRF) scanner at a resolution of 2 mm for the 2014 cores and 1 mm for the 2015 cores also at the Geological Institute of the University of Bern. A special plastic film was used to cover the cores and protect the sensor from contamination. Each scan produced a RGB digital image, a radiographic digital image and a μ XRF elemental profile. The 2014 cores were measured using a Mo tube with 40 kV voltage, 20 mA current and 10 seconds exposure time. The range of elements included Al, Si, K, Ca, Ti, Mn, Fe, Rb, S, Sr and Zr. The 2015 cores were measured also using a Mo tube with 45 kV voltages, 20 mA current and 20 seconds exposure time. The range of elements included Al, Si, K, Ca, Ti, Mn, Fe, Rb, Ni, Cu, Pb, Br, S, Sr and Zr. μ XRF data were used to correlate between the cores and isolate cryptotephra layers.

4.4.3 Tephra layer identification from scanning techniques

As discussed in section 3.2.1, scanning techniques have been used to identify possible tephra layers which are invisible to the naked eye. MSCL measurements are particularly useful to identify tephra layers as volcanic material may contain ferromagnetic minerals and may be denser. However, this method was only partially successful in this study, revealing mostly only optically visible tephra layers rather than discerning the thin cryptotephra as was cautioned by Gehrels et al. (2008). XRF has also been shown to find cryptotephra as certain elements could be indicative of tephra depending on their composition (Davies et al. 2015; Vogel et al. 2009) which may differ between eruptions (e.g. Lim et al. 2008). It was not known precisely which ratios/elements could be useful so all elements were investigated separately. In this study, the elemental ratios Ti/Ca, K/Sr, Mn/Ca, Ca/Ni and Zn/Ca were the most useful in identifying cryptotephra, as was identified by (Davies et al. 2015). Like for MSCL, this method was only partially successful, revealing mainly the thicker layers.

4.4.4 Hyperspectral core scanner

The hyperspectral imaging (HI) scanner measures sediment reflectance from which properties such as mineralogy and organic compounds can be inferred. Optical reflectance spectroscopy records in the visible and near infrared (400 - 1000 nm) wavelengths of the electromagnetic spectrum (Butz et al., 2015; Croudace and Rothwell, 2015; Grosjean et al., 2014). HI produces rapid, semi-quantitative data at very high sample resolution (38 x 38 μ m) (Grosjean et al., 2014). HI scanner can be combined with digital imaging to create compositional maps (Croudace and Rothwell, 2015). The CNP open cores were scanned using a Specim Ltd sediment-core-scanning system (SCS) scanner which consists of a hyperspectral camera (Specim PFD-xx-V10E) and a Schneider Kreuznach Xenoplan 1.9/35 lens as well as a tray that moves underneath an illumination chamber (Butz et al., 2015; Grosjean et al., 2014). The images were measured in the very near infrared spectrum from 400 - 1000 nm. The camera slit is 30 μ m wide and the spectral resolution 2.8 μ m sampled at 0.78 nm intervals (binning 1). Dark (closed shutter) and white (BaSO₄ ceramic) reference material were also scanned. The software used to capture the images

was ChemaDAQ Specim Ltd. The images were then processed in ENVI5.0 software following the methodology of Butz et al. (2015).

4.5 Flood layer classification

4.5.1 L. Llaviucu core correlation

L. Llaviucu 2014 and 2015 cores were correlated in order to create a master core containing the flood layer classification. The correlation was done visually by assigning layers to each other using stratigraphical order as parameter. The resulting classification was also used in the radiocarbon age-depth modelling to produce a slump-corrected model.

4.5.2 XRF classification

Based on the correlated stratigraphy, several methods were attempted to classify flood layers including using XRF and HI data. Classification using XRF data targeted elements which have been previously shown to relate to flood layers (Davies et al. 2015) such as the covariation between K and Ti. Parallel peaks in both elements may reflect flood layers. Other elements such as Rb, Ba and Zr were also investigated but were found to be too noisy.

4.5.3 HI classification

Classification using HI data was attempted on LLA15-6 following the procedures described by Butz (2016). Two main classification types are distinguished: supervised and unsupervised classification (Jain, 2010). Following an unsupervised procedure the number of anticipated classes is selected but no other data input is necessary. On the other hand, supervised classification requires the selection of training areas which must be a-priori known by the user. In both procedures the algorithm type must be selected. Asadzadeh and de Souza Filho (2016) provides an overview of the classification methods.

The methodology for the hyperspectral data processing followed that described by Butz (2016). In the sub-setting routine, the hyperspectral data were first cut off at a wavelength of 480 nm in order to remove the noise at the lower blue edge of the visible spectrum. The hyperspectral profiles were then filtered using the Savitzky-Golay moving window which calculates a polynomial fit with different degrees of smoothing (Butz, 2016). The subsequent preparation procedure of the resulting filtered data then followed Butz et al. (2015) before the classification procedures were applied. The number of classes was varied (2, 3 or 4) to try obtaining the best results. Classes for tephra, flood layers, organic layers and background sediment were created (**Fig. 4-1**).

The supervised classification procedures used were as follows:

- A.** Spectral angle mapping (SAM) using manually and automatically determined endmember collections and a maximum angle of 0.1 radians as threshold of similarity.
- B.** Minimum distance which is implemented through the classification workflow. This classifier calculates the minimum Euclidean distance between a sample and a reference spectrum (Butz, 2016).

The unsupervised classification procedure used was as follows:

A. ISODATA classification which is highly dependent on the number of classes selected.

In a last step, post-classification processing was attempted to diminish minor classes and to aggregate dominating areas. Cleaning-up procedures followed that described in Butz (2016) including sieving and clumping different classes.

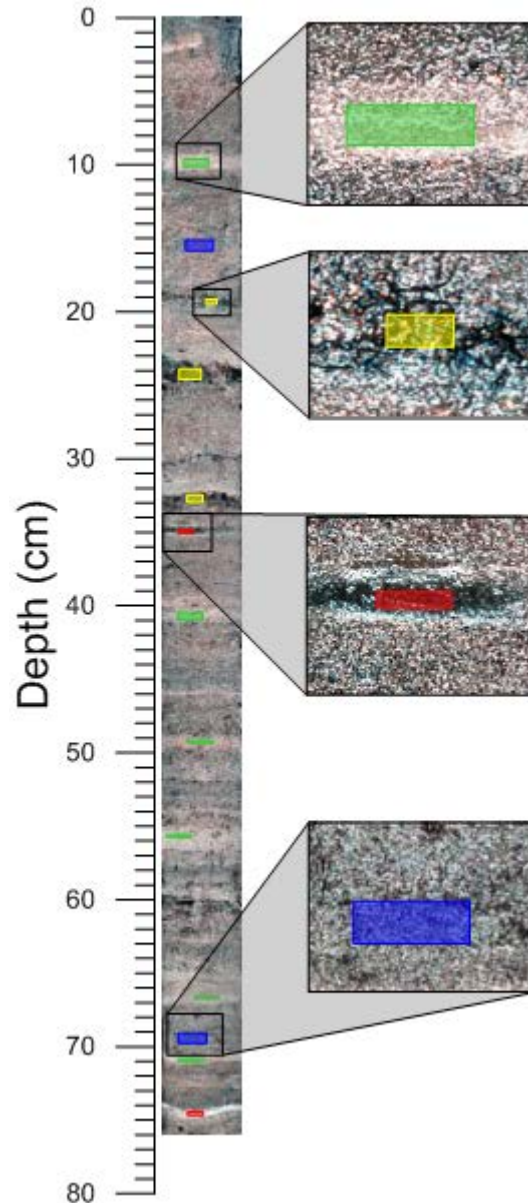


Fig. 4-1 L. Llaviucu 2015 (top half) core shown with example locations of training areas for tephra (red), background sediment (blue), flood layers (green) and organic layers (yellow).

4.6 Wet chemical analysis

The wet chemical analysis employed in this study aimed to reconstruct the impact of fisheries within L. Llaviucu as well as investigate climatic and environmental change. Core sediment, sediment trap material and algae material were measured for elemental carbon and nitrogen as well as ^{13}C and ^{15}N isotopes. The techniques are described below in more details.

4.6.1 Elemental carbon and nitrogen

Total organic carbon (TOC) and total nitrogen (TN) concentrations are measured in order to calculate C:N ratios. These three parameters are useful to investigate the origin of organic material (Meyers and Ishiwatari, 1993) but also track lake productivity (Cohen, 2003). C:N ratios have been used to distinguish between aquatic and terrestrial sources of sediment organic matter (Meyers, 1994). This method uses the fact that vascular plants such as grasses, shrubs and trees have higher ratios (>20) than non-vascular aquatic plants (4 - 10) (Fig. 4-2) (Meyers and Ishiwatari, 1993; Meyers, 1994). The distinction arises from the abundance of cellulose in land plants and its absence in algae (Meyers, 1994). Ratios of 13 - 14 would suggest a mixture of terrestrial and aquatic contributions (Meyers and Ishiwatari, 1993).

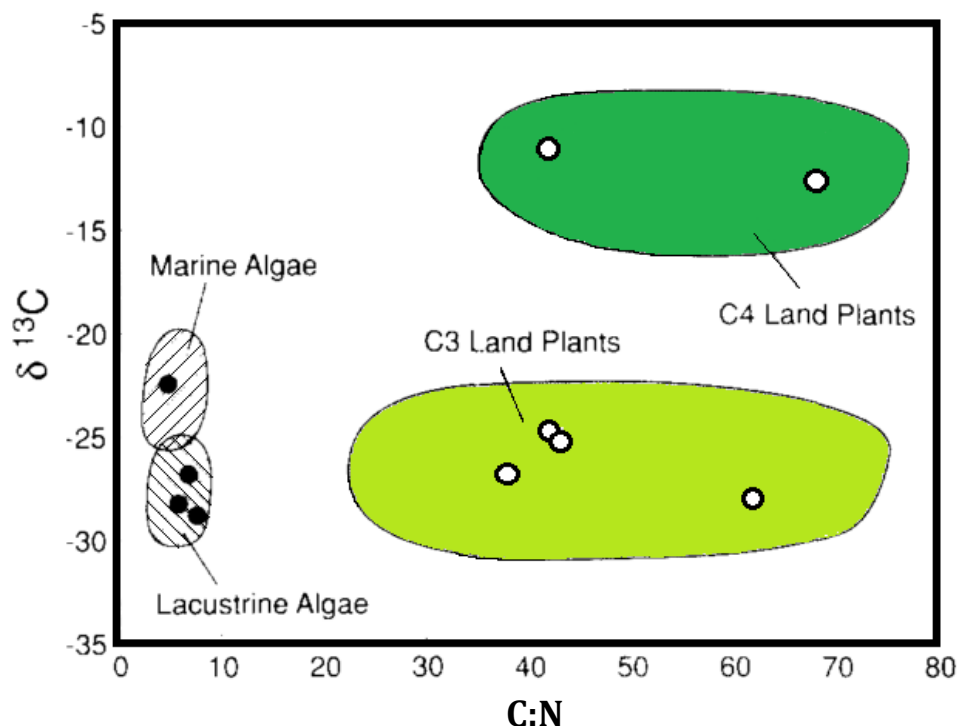


Fig. 4-2 Distinctive source C:N and $\delta^{13}\text{C}$ isotopic signature for C3 and C4 land plants as well as marine and lacustrine algae. Adapted from Meyers (1994).

Analyses were conducted on sediment core material as well as algae at the Geographical Institute of the University of Bern via continuous flow isotope ratio mass spectrometry using a Vario EL Cube Elemental Analyser (Elementar, Germany). Sediment trap material was measured by Tobias Schneider. The data for carbon and nitrogen concentration was converted to flux ($\text{mg}/\text{cm}^2/\text{yr}$) by multiplying by the sedimentation rate at the depth of the particular sample.

4.6.2 ^{13}C and ^{15}N isotopes

Measurement of ^{15}N and ^{13}C in lacustrine sediment has been limited to date (Meyers and Ishiwatari, 1993) but may provide information on lake productivity and the food chain (Ohkouchi et al., 2015). While carbon isotopes are influenced by internal and external lake processes such as eutrophication and watershed vegetation change, nitrogen is predominantly controlled by lacustrine autochthonous inputs (Cohen, 2003). Teranes and Bernasconi (2000)

bring attention to the possibility of identifying the addition of heterotrophs into a lake system by an increase in $\delta^{15}\text{N}$ values as $\delta^{15}\text{N}$ increases by 3 - 4‰ with every trophic level. As large quantities of heterotrophs were added to L. Llaviucu, it is likely the faecal matter of the animals incorporated in the sediment would have a different isotopic signature to the background deposition.

Nitrogen and carbon isotopic analyses have also been used to determine the source of sedimenting organic matter (Cohen, 2003). However, as depicted in **Fig. 4-3**, freshwater algae have the same ^{15}N isotopic signature range as terrestrial C3 plants. Similarly the signature of certain freshwater algae appears to overlap with C3 plants. This realization has led several authors to warn that lake derived organic matter is indistinguishable from organic matter from the surrounding watershed (Meyers and Ishiwatari, 1993; Meyers, 1994; Ohkouchi et al., 2015). Any interpretation on the provenance of organic matter should be made together with C:N ratio information.

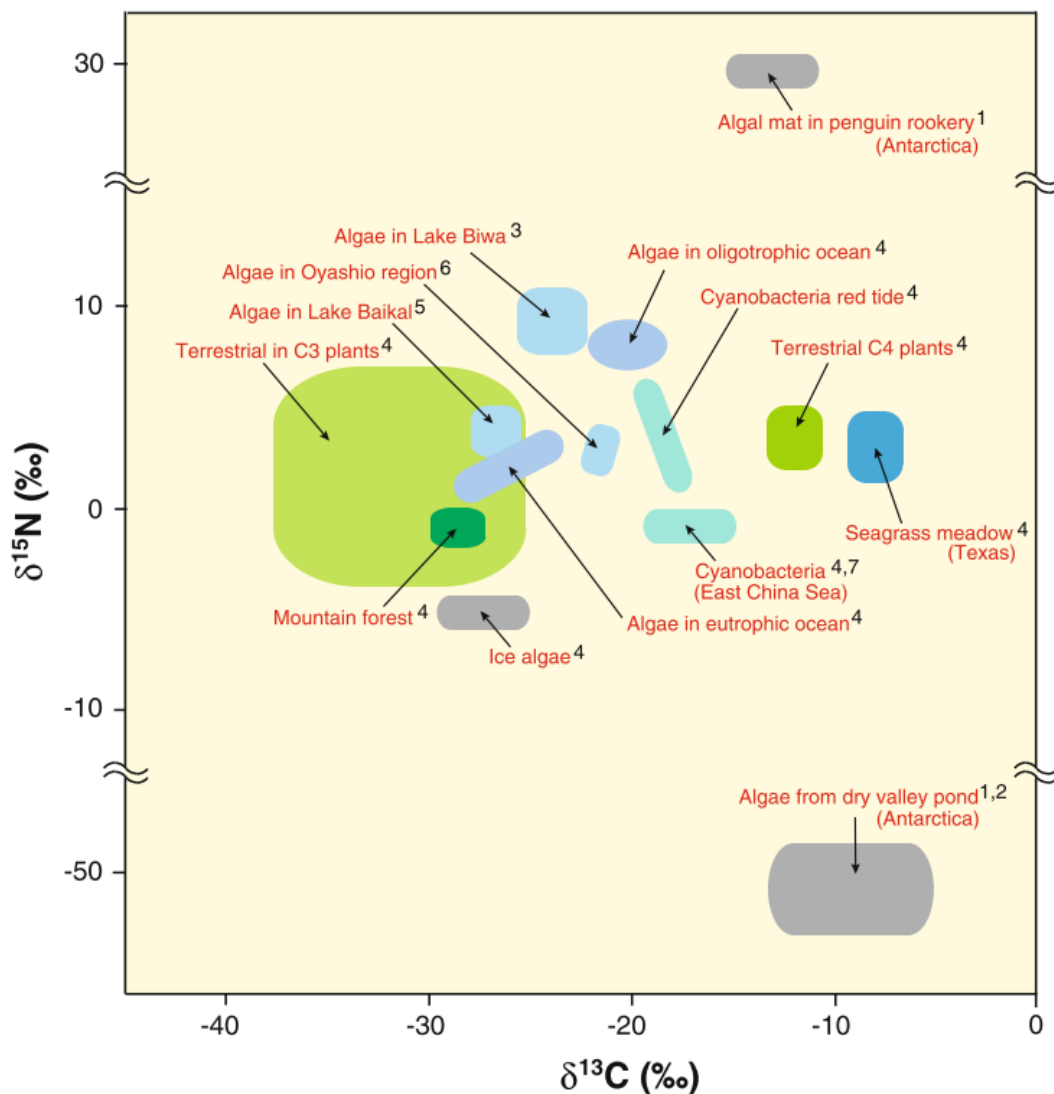


Fig. 4-3 Nitrogen and carbon isotopic signatures of different land plant types as well as marine and freshwater algae. Source: Ohkouchi et al. (2015).

Isotopes of ^{15}N and ^{13}C were measured on core sediment and algae using the same machine as for the elemental analysis (see section 4.6.1). Measurements were made every 6 mm down-core

and every tenth sample was triplicated. Isotopic values were corrected for drift as highlighted by the analysis of glutamic acid. Isotope ratios are reported as δ -values and expressed as ‰ according to the equation

$$\delta X = [(R_{\text{sample}}/R_{\text{standard}})-1] \times 1000 \text{ [‰]} \quad (3)$$

where X is ^{15}N or ^{13}C , R_{sample} is the corresponding ratio $^{15}\text{N}/^{14}\text{N}$ or $^{13}\text{C}/^{12}\text{C}$ and R_{standard} is the ratio of the international reference AIR for nitrogen (IAEA-N-2) and Vienna PeeDee Belemnite for carbon (IAEA-C-6). The standard deviation of multiple analyses was calculated to represent the accuracy of the $\delta^{15}\text{N}$ measurements but this was not possible for ^{13}C .

4.6.3 Statistical analyses

Statistical analyses were performed on standardized data (mean 0, standard deviation 1) consisting of carbon and nitrogen flux, C:N ratio, $\delta^{13}\text{C}$, $\delta^{15}\text{N}$ and percentage water content. A range of different constrained hierarchical clustering methods were tested on the dataset. Also known as agglomerative cluster analysis, this bottom up technique starts with single observations and pairs them to their nearest cluster. The result is an evolutionary tree which can be cut to obtain a number of clusters (Wilks, 2011). Constraining the method means it is forced to stay within stratigraphic order. Constrained incremental sum of squares (CONISS) and unweighted pair group method with arithmetic mean (UPGMA) were used. In addition, a biplot was created between $\delta^{13}\text{C}$, $\delta^{15}\text{N}$ values to track the change in isotopic values through time. The CONISS method was found to yield more stable results and this was compared to the biplot.

4.7 Dating techniques

Tephrochronology and absolute dating complement one another. Here radiocarbon dating as well as ^{210}Pb were employed to strengthen the chronology and are described in more detail.

4.7.1 The ^{210}Pb cycle

^{210}Pb can provide a highly resolved chronology of young sediment when measured at a high sampling resolution. The method is based on the latter part of the decay chain of ^{238}U (Fig. 4-4). An isotope within this chain, ^{226}Ra , is found in exposed bedrock and soils in trace amounts and decays to a gas, ^{222}Rn which moves into the atmosphere (Cohen, 2003). ^{222}Rn decays rapidly to ^{210}Pb which is then deposited from the atmosphere onto land (Cohen, 2003). Fallout is assumed to be spatially constant but the fallout amount may actually vary from place to place depending on rainfall and geographical location (Appleby, 1998). ^{210}Pb in lake sediments is composed of a supported fraction due to natural decay in the sediment and an unsupported part arising from fallout (Appleby, 2008). As the sediment becomes buried by younger sediment, ^{210}Pb starts to act as a natural clock recording the time since deposition (Appleby, 2008). Measurements of mean ^{226}Ra can be used to infer supported ^{210}Pb which can then be subtracted from total ^{210}Pb to calculate the unsupported fraction (Cohen, 2003). However, ^{210}Pb dating is complicated by the fact that the concentration of ^{210}Pb at the surface of the lake bed is a function of both the flux rate of the unsupported ^{210}Pb and the background sedimentation rate (Cohen, 2003). Therefore, once unsupported ^{210}Pb has been calculated, the activity must be transformed into an age with the help of models and plotted as age in years versus depth in the sediment core in cm (see sections 4.7.2, 4.7.3 and 4.7.4).

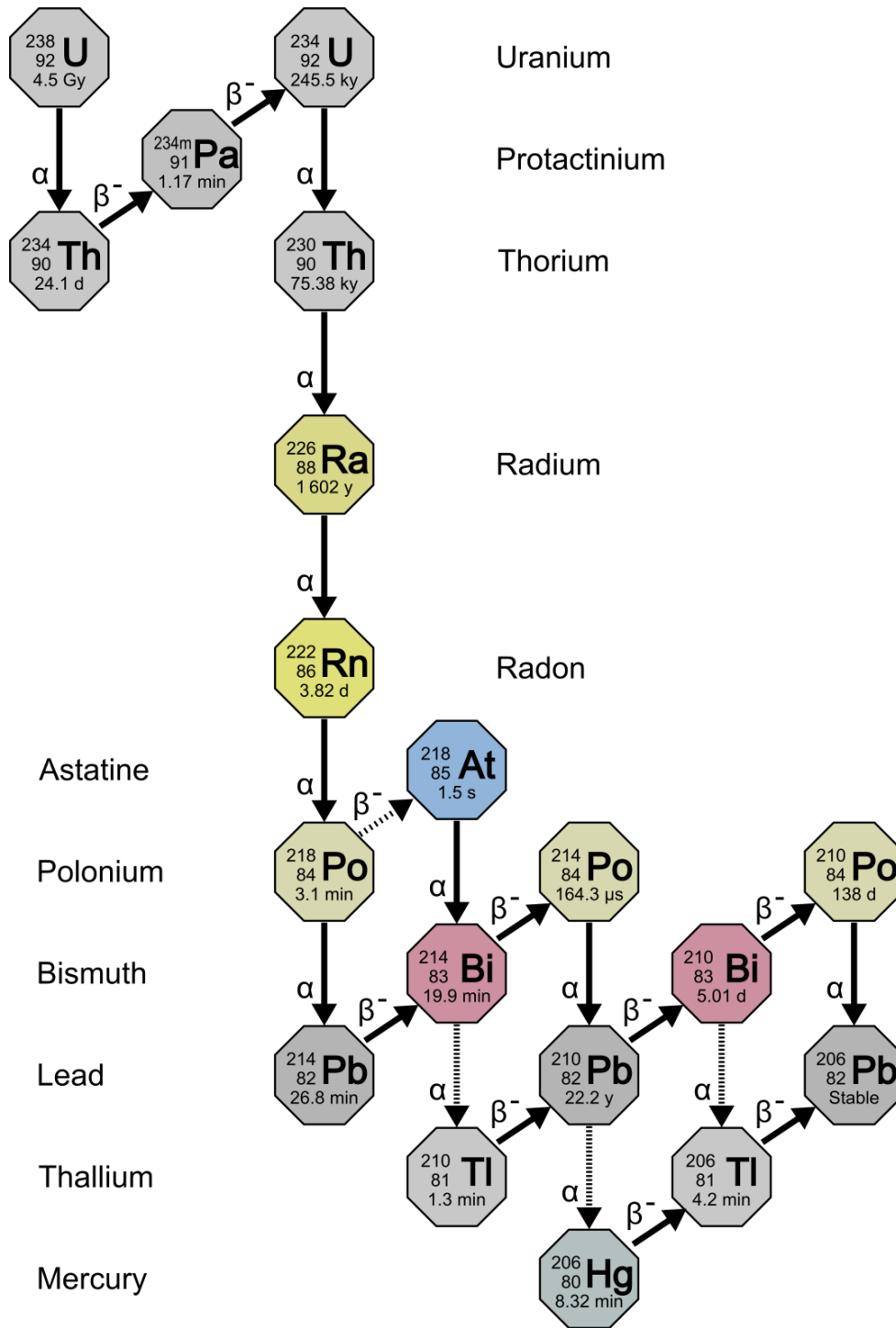


Fig. 4-4 Radioactive decay chain of ^{238}U to ^{206}Pb with the decay pathway as well as the half-life times indicated..

^{210}Pb dating

Sediment cores from L. Fondococha and L. Llaviucu were analysed for ^{137}Cs , ^{226}Ra and ^{210}Pb by W. Tylmann at the Uniwersytet Gdański, Poland. Due to the low mass of the sediment available, the total activity of ^{210}Pb was determined by measuring its daughter product ^{210}Po using alpha spectrometry. The full procedure is detailed in Tylmann et al., (2016).

Constraining the ²¹⁰Pb profile

The independent validation of the chronology obtained by ²¹⁰Pb is essential to have high confidence in the results (Appleby, 1998; Putyrskaya et al., 2015). Other radiometric elements such as ¹³⁷Cs are often used in conjunction to ²¹⁰Pb as independent time markers (Appleby, 1998). The ¹³⁷Cs bomb spike was detected in the Galápagos for the year 1963 by Conroy et al. (2008). However, only traces of ¹³⁷Cs were found in the CNP lakes which meant this time marker could not be used. Low ¹³⁷Cs may be reflecting a trend in low ⁹⁰Sr found by French (1960) for the Central Cordillera.

4.7.2 Constant Initial Supply (CIS) model

The first model used was the CIS (Goldberg, 1963 as read in Putyrskaya et al. 2015) further refined by Krishnaswamy et al. (1971). This model assumes a constant initial concentration of ²¹⁰Pb (Cohen, 2003; Putyrskaya et al., 2015). The initial activity of the unsupported ²¹⁰Pb per gram dry weight is assumed to have remained unchanged throughout the deposition period (Cohen, 2003). The age of the sediment can be calculated from the following equation:

$$t(x) = \frac{1}{\lambda} \cdot \ln \frac{C(0)}{C(x)} \quad (4)$$

where λ is the radioactive decay constant of ²¹⁰Pb in yr⁻¹, C(0) and C(x) are the initial and present activity concentrations of the unsupported ²¹⁰Pb in the layer at depth x in Bq g⁻¹ (Putyrskaya et al., 2015). Cumulative dry mass is used in order to eliminate the effect of sediment compaction with depth, and this is true for all other models (Putyrskaya et al., 2015). Although simplistic, the CIS model works well for lakes with constant sedimentation rates (Cohen, 2003).

4.7.3 Constant Rate of Supply (CRS) model

The CIS model assumes a constant initial concentration at each stage of accumulation despite evidence for varying accumulation rates. Taking this into consideration the CRS model was developed by Appleby and Oldfield (1978). The CRS model assumes a deposition of the same amount of unsupported ²¹⁰Pb per time interval and at variable sedimentation rates (Putyrskaya et al., 2015). This assumption results in lower ²¹⁰Pb concentrations at times of higher background sedimentation rates (Cohen, 2003). The age of the sediment can be calculated from the following equation:

$$t(x) = \frac{1}{\lambda} \cdot \ln \frac{C_r(0)}{C_r(x)} = \frac{1}{\lambda} \cdot \ln \frac{\int_0^{\infty} \rho_b(x) C(x) dx}{\int_x^{\infty} \rho_b(x) C(x) dx}, \quad (5)$$

where Cr(0) is the total cumulated unsupported ²¹⁰Pb in the sediment core in Bq cm⁻²; Cr(x) is

the residual (cumulated) unsupported ^{210}Pb in the sediment below the depth x in Bq cm^{-2} ; λ is the radioactive decay constant for ^{210}Pb in yr^{-1} ; $\rho_b(x)$ is a bulk density of sediments in g cm^{-3} ; $C(x)$ is the activity concentration of the unsupported ^{210}Pb at depth x in Bq g^{-1} (Putyrskaya et al., 2015). The CRS model has proved more reliable for lakes with varying sediment rates (Appleby, 2008; Cohen, 2003).

4.7.4 Sediment Isotope Tomography (SIT) model

The latest ^{210}Pb model is the SIT which was developed to interpret more complex ^{210}Pb vertical profiles in cases where both the fluxes of unsupported ^{210}Pb and the sediment rate vary with time (Putyrskaya et al., 2015). The model applies inverse numerical analysis techniques to separate components of variations in radioisotope activity and sediment depth caused by variations in sediment accumulation rate and ^{210}Pb flux (Carroll and Abraham, 1996). A more complex equation calculates the vertical distribution of ^{210}Pb activity:

$$C(x) = C(0)\exp\left[-\lambda \cdot x_{\max} \bar{S} \left(z + \underbrace{\sum_{n=1}^N \frac{a_n}{n\pi} \sin\left(\frac{n\pi x}{x_{\max}}\right)}_{\text{Sedimentation term}} \right) + \left(\underbrace{\sum_{n=1}^N \frac{b_n}{n\pi} \left(1 - \cos\left(\frac{n\pi x}{x_{\max}}\right)\right)}_{\text{Source term}} \right) \right] \quad (6)$$

where $C(x)$ is the unsupported ^{210}Pb activity concentration at depth x in Bq cm^{-3} ; $C(0)$ is the initial unsupported ^{210}Pb activity concentration in Bq cm^{-3} ; x_{\max} is the greatest depth of the measurement in cm ; $S(x)$ is slowness in yr cm^{-1} : ($S = 1/v$), where v is the sedimentation speed in cm y^{-1} ; \bar{S} is the average slowness; z is a relative depth: $z=x/x_{\max}$; a_n and b_n are the unknown Fourier series coefficient (Putyrskaya et al., 2015). The age of the sediment can then be calculated from the following equation (Putyrskaya et al., 2015):

$$t(x) = x_{\max} \cdot \bar{S} \left[z + \sum_{n=1}^N \frac{a_n}{n\pi} \sin(n\pi z) \right] \quad (7)$$

The SIT model would have provided the most reliable results but due to time constraint this avenue was not investigated any further.

4.7.5 Mass accumulation rate (MAR)

The most plausible ^{210}Pb age model was combined with sediment depth to calculate the dry mass sedimentation rate after Appleby (2001):

$$r = (\lambda \cdot A/C)/10 \quad (8)$$

where r is the dry mass sedimentation rate in $\text{g cm}^{-2} \text{y}^{-1}$, λ is the ^{210}Pb radioactive decay constant of 0.03114 y^{-1} , A is the unsupported cumulative inventory (Bq/m^{-2}) and C is the unsupported activity (Bq/kg). The MAR was used to calculate the fluxes in elemental carbon and nitrogen.

4.8 Theory behind radiocarbon dating

The continuous bombardment of cosmic rays onto the atmosphere forms radioisotopes such as ^{14}C . The oxidation to $^{14}\text{CO}_2$ avails the radioactive isotope to plant photosynthesis (Cohen, 2003). The molecule then becomes incorporated into the tissue of organisms with a certain $^{14}\text{C}/^{12}\text{C}$ ratio close to the atmospheric ratio (Blaauw and Christen, 2005). However, this ratio becomes unstable once the organism dies and the ratio will start to decrease. Measuring this decay of ^{14}C back to its original isotope ^{14}N allows the determination of a radiocarbon age (Blaauw and Christen, 2005; Cohen, 2003). The relatively short half-life of this decay (5730 years) permits the method to be used for time periods back to 50 kyrs (Cohen, 2003). The technique was first developed in Libby et al. (1949) and has since become a method of choice.

Bulk or macrofossil samples are measured to estimate the age of the material. However, the relationship between radiocarbon and calendar ages is not linear due to variations in the Earth's magnetic field and CO_2 concentration which means the radiocarbon ages must be calibrated (Cohen, 2003). The choice of the calibration curve varies with the geographical location as well as whether the sample is terrestrial or marine so several curves exist (e.g. SHCal04 for the southern hemisphere, IntCal13 for northern hemisphere and Marine13 for marine samples) (McCormac et al., 2004; Reimer et al., 2013). The calibration of ^{14}C dates aims to find the probability of a date belonging to a given calendar year which can then be used in an age-depth model (Blaauw, 2010).

The choice of the material used for dating affects the age estimate. The sample may not be contemporaneous with the surrounding sediment and often older material contaminates younger deposits by reworking processes or by the inclusion of older soil material (Cohen, 2003). As a result terrestrial macrofossil dating is preferred as these are less likely to be influenced by this "reservoir effect" (Cohen, 2003). However, macrofossils may also be affected by a "hard-water effect", a situation where the age of water in contact with limestone is increased, so lacustrine invertebrates or aquatic macrophytes should be avoided (Cohen, 2003).

Building a chronology for palaeoenvironmental analysis requires building an age-depth model to estimate the calendar age of depths in a core based on a limited number of data points (Blaauw, 2010). Age-modelling assumes a monotonic relationship between the sediment deposition and time so that deeper levels are always older than the higher levels except in exceptional circumstances (law of superposition as described by Nicolas Steno in the 17th century). Commonly, dates are interpolated between available data but this presents many disadvantages as described by Blaauw and Christen (2005). An improved method is to use calendar age probability distributions by taking into account stratigraphic position, prior assumptions and down-weighting outliers (Blaauw and Christen, 2005). This has been applied in the last decades as either "classical" or Bayesian age-modelling approaches through software such as Clam and Bacon (Blaauw and Christen, 2011, 2005). Age-depth models may be slump-corrected when flood layers are abundant.

4.8.1 Radiocarbon dating of the CNP lakes

In a first step, a series of bulk and macrofossils were dated from L. Llaviucu and L. Fondococha in order to assess the possibility of a reservoir effect. Samples were measured by Accelerated Mass Spectrometry (AMS) at the MICADAS ^{14}C AMS laboratory at the University of Bern, Switzerland.

As the bulk samples revealed a reservoir effect of varying age was present for L. Llaviucu and L. Fondococha (approx. 300 and 700 years respectively) further efforts were focused in a second step on finding datable macro-fossils. Sediment from catchments with low vegetation cover often lack organic remains (Cohen, 2003) but very small fossils (27-648 μg) could be found by sieving extensive amounts of material for each of the lakes. These were measured using a gas ion source (Salazar et al., 2015). The focus was on selecting terrestrial plant material which were identified and photographed under the light microscope. Finding macro-fossils from layers above and below tephra layers was a particular aim in order to date volcanic events accurately. The radiocarbon ages were calibrated using the northern hemisphere calibration curve IntCal13 (Reimer et al., 2013) using the software Calib v.7.1 (Stuiver and Reimer, 1986). The age-depth modelling used both classical and Bayesian approaches and compared for the “best” results.

Classical modelling approach

The Clam (Classical Age Model) software follows a classical modelling approach (Blaauw and Christen, 2005). In this model, all radiocarbon dates of a sequence are calibrated individually by calculating their calibrated distributions for every calendar year. Outlying samples can be removed and dates falling outside the range of the calibration curve are not used. The age-depth model is constructed by specifying the type of model which can be linear interpolation, linear or higher order polynomial regressions or cubic, smoothed or locally weighed splines. The confidence intervals are then calculated using a Monte Carlo approach (Blaauw and Christen, 2005).

CLAM modelling for L. Llaviucu used the IntCal13 (Reimer et al., 2013) curve and linear interpolation between dated levels. The 95% confidence interval stems from 1000 Monte Carlo simulations. The calendar age point estimates for the depths were based on the weighted average of all the age-depth curves. The resulting age scale was plotted using cal. BP at a resolution of 1 yr. Three outliers at 21.15, 55.45 and 61.30 cm depth were assumed as the age of the samples appeared too old. A slump corrected model for L. Llaviucu was attempted using the CLAM modelling approach based on the flood layer classification from section 4.5. Tephra and flood layers were removed from the CLAM modelling under the assumption that they deposited instantaneously as often done for clastic rich sediments (e.g. Wirth et al., 2013). Settings remained the same for L. Fondococha except that only one outlier at 26.65 cm was assumed as its age appeared too old.

Bayesian modelling approach

The Bacon model uses Bayesian statistics to reconstruct Bayesian accumulation histories by combining radiocarbon and other dates with prior knowledge. The model takes into account prior assumptions regarding the accumulation rate as well as its variability over time and it is not influenced by outliers as the dates are modelled through a student-t distribution with wide tails (Blaauw and Christen, 2011). The Bacon model divides the core into many time slices and through millions of Markov Chain Monte Carlo (MCMC) iterations estimates the accumulation rate for each section. The combination with an estimated starting date yields an age-depth model (Blaauw and Christen, 2011). BACON modelling for L. Llaviucu used accumulation rates of 20 yr/cm based on data from Michelutti et al. (2015) and Rodbell et al. (1999) and default acceleration shape of 1.5. The default memory settings were retained. No slump-corrected

modelling was attempted as this was beyond the scope of this study. The same settings were used for L. Fondocochoa.

4.9 Tephra analysis

The analysis of tephra as a chronostratigraphic tool was discussed in detail in Chapter 3. In the following section, the method adopted in this study is described in detail based on the literature review.

4.9.1 Optical identification

Potential tephra layers identified through the non-destructive scanning methods (section 4.4.3) were checked by optical microscopy before sub-sampling the cores. Microscopic slides were produced from every layer identified through the non-destructive techniques. These were viewed under polarized and un-polarised light. Tephra glass was identified as clear grains with sharp edges and occasionally vesicles under plain light. Some particles had a green tint. Other particles were identified as pumice from being light grey and highly vesicular (**Fig. 4-5**). Under polarized light, tephra showed light grey birefringence with extinction between 0 - 5°.

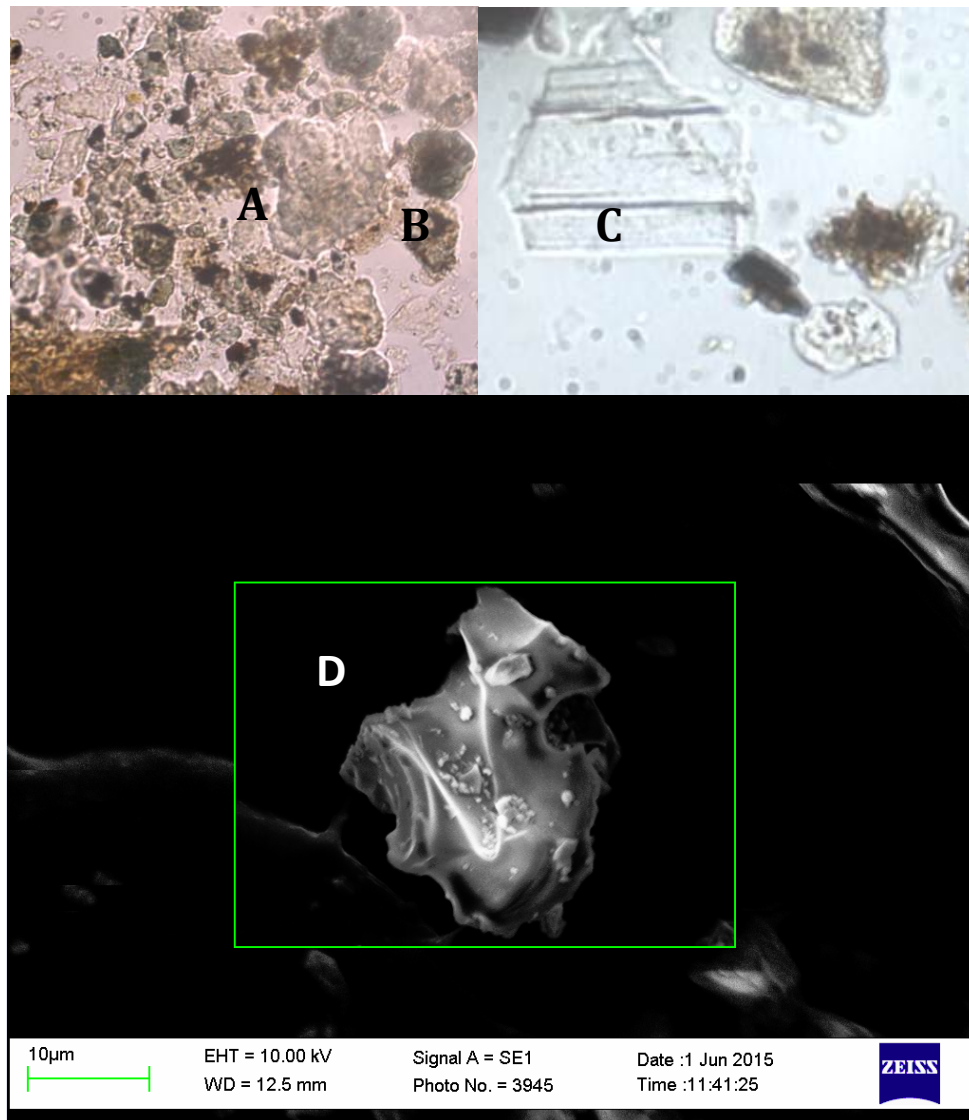


Fig. 4-5 Image from the light microscope showing pumice (A; LLA14-1A) and green particles (B; LLA14-1A) and striated glass shards (C; FON14-1-A). Particle (D; FON14-1A) was taken using the SEM.

4.9.2 Extraction test

It was decided to use bulk chemical assay using ICP-MS to fingerprint the tephra. This method although susceptible to detrital mineral contamination was chosen because it would allow the geochemical fingerprinting of extremely fine tephra in a relatively short time as was the case in this study. In order to make the results as accurate as possible, the samples had to be cleaned from contaminations to the best possible level. A test was therefore undertaken on two 1 cm³ samples, one from a cryptotephra layer (FON39.5), and the other from a thick layer (FON75.5) in order to devise the best possible cleaning technique.

Test 1: decanting

Decanting was attempted as a first cleaning procedure by adding 100 ml distilled water and 3 ml dispersant (16.5 g of sodium-hexametaphosphate and 3.5 g sodium carbonate) to the two test samples. The samples were shaken and after 5 seconds the supernatant was decanted. This procedure was repeated twice and the supernatant and residue were checked under the

microscope using microscopic slides. It was found for both samples that the residue still contained much clay but that decant did remove some clay, charcoal and diatoms. The results were better for the tephra layer than for the cryptotephra. In another test, 5 ml dispersant and 40 ml deionised water was added to the <41 µm fraction. The samples were “shocked” in the centrifuge at 4000 rpm for 12 seconds with full acceleration and deceleration. The suspended material was pipetted off to remove the clay fraction. This method was found to be most efficient.

Test 2: pump filtering

The residue of the samples was filtered with 41 µm paper using a pump in order to remove the very fine fraction including clay and diatoms. However, it was found that the <41 µm fraction contained much fine tephra material as well as clay and diatoms. This was more prominent for the cryptotephra layer which in general contains fewer tephra grains. Adding 5 ml of dispersant solution was found to help remove clay particles.

Test 3: heavy liquid separation

Sodium Polytungstate (SPT) was used to separate particles of different densities in a modified procedure developed by Blockley et al. (2005). Each stage was repeated until all the material had floated up and the samples washed at least 10 times. Repeated washing was deemed highly important when it was discovered that even after three washes SPT was still present within the sample. This was discovered when the washed sample was freeze-dried, leaving non-volatile SPT within the sample.

SPT at 1.98 g/cm³ was used in a first instance. Particles recovered in the float included charcoal, amorphous organic matter and silica, phytoliths as well as one or two tephra grains. The organic material found at this density stage indicated the oxidizing phase should be prolonged. SPT at 2.0 g/cm³ was then used, recovering in the float mostly diatoms, amorphous silica and charcoal for the cryptotephra sample. However, for the FON75.5 tephra layer sample, the float contained pumice almost exclusively. This contradicting effect indicates tephra of different nature is in each of the samples. This is problematic if a unique procedure is to be developed to concentrate tephra. However, it has been indicated that pumice very likely contains varying proportions of phenocrysts which would affect the overall composition. Removing pumice is thus recommended (Pearce et al., 2004). SPT at 2.5 g/cm³ was used in a next step. Decanting off the float at this stage was difficult as the residue no longer coalesced so pipetting was preferred. The float at this density consisted exclusively of brownish tephra shards on average 60 µm in length. The coloured tephra may be reflecting the deterioration of the glass to clay-bearing bentonite (Pearce et al., 2004).

A further separation at 2.7 g/cm³ (density of quartz) recovered almost exclusively glass shards, although one or two other mineral particles were also found. At this density, the sample could be considered as clean. However, as described in the literature, this sample would only contain the light density fraction of the tephra, as the presumably basaltic component has a higher density (Mackie et al., 2002). The residue (>2.7 g/cm³) was found to consist of higher density greenish basaltic tephra shards as well as many other minerals.

Test 4: magnetic separation

It was attempted to separate the basaltic tephra using a magnetic separator as is described in the study by Mackie et al. (2002). However, it became quickly apparent that such techniques are not possible for small volumes of fine ash as is found in the Ecuadorian lake cores. This leads to question the plausibility of Mackie et al. (2002) study since they separated only 1 cm³ of sediment as in the present study. In addition, the authors oven dried the samples to enhance the magnetic signal, a procedure which has been shown to affect the geochemistry (Roland et al., 2015). In this study, a hand magnet was tested to separate the basaltic shard. The result of this was inconclusive as glass shards were found both in the magnetic and non-magnetic fraction. In conclusion, it was decided to discard the heavier basaltic fraction and keep the light density fraction instead for fingerprinting.

4.9.3 Applied extraction

Having tested different methods on two samples, a cleaning procedure could be developed and is shown as a flowchart (**Fig. 4-6**).

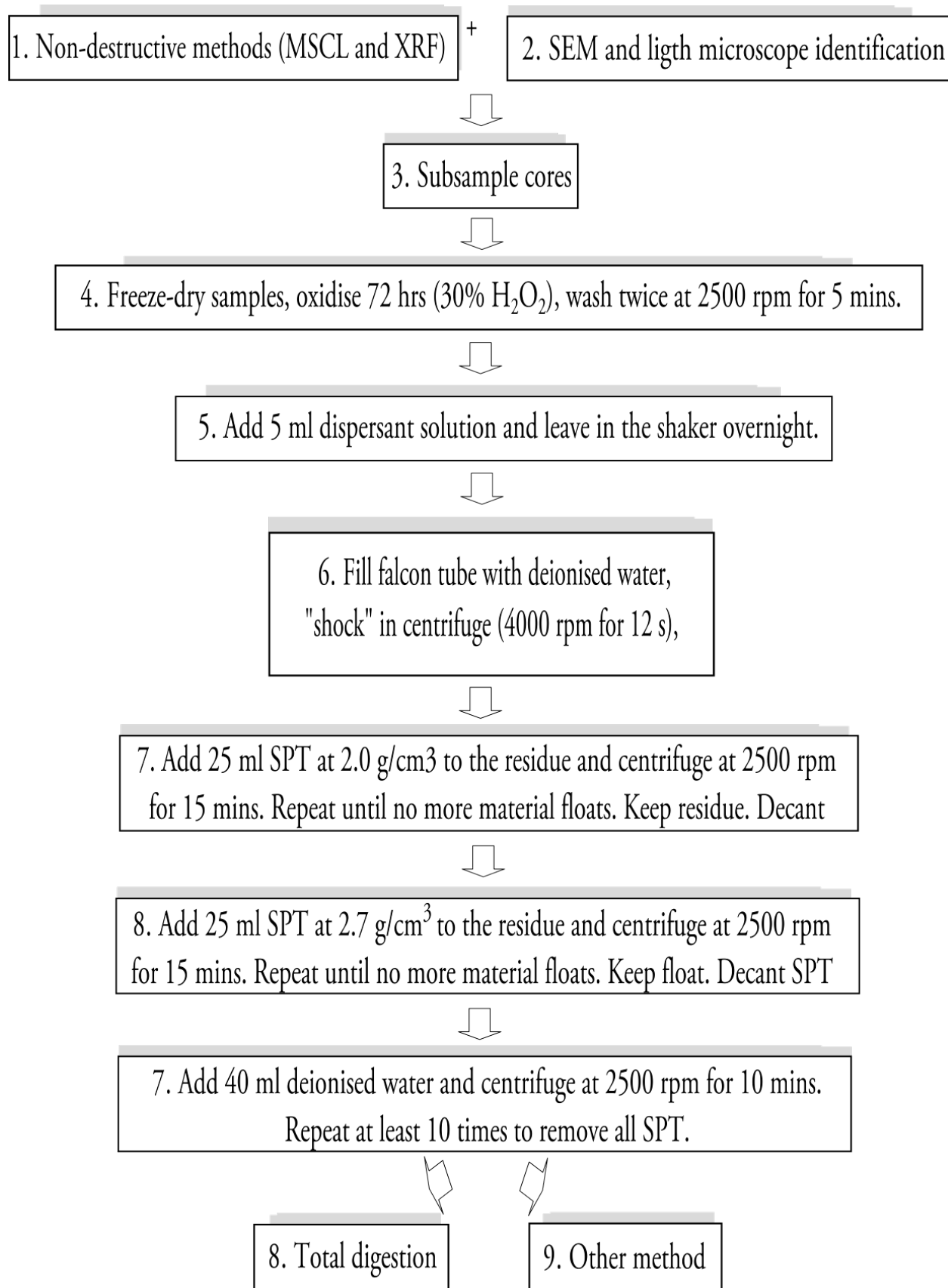


Fig. 4-6 Flowchart of the step density and clay removal cleaning procedure. Other method (9) are described in section 3.2.6.

4.9.4 Colour and morphological classification

As the correlation of tephra requires an analysis of both physical and chemical attributes (Cohen, 2003), a colour and morphological classification was attempted after the extraction procedure. A morphological analysis based on the scheme developed by Liu et al. (2015) (Fig. 4-7) using degrees of vesicularity and crystallinity was attempted on 20 random images from each cleaned tephra layer (see Fig. 5-16). The images were obtained from a scanning electron microscope using a 10 kV accelerating voltage, and focused beam at the University of Bern. With twenty images it was found that the mean size was only slightly over-estimated. The classification scheme from Liu et al. (2015) was altered so as to also include the degree of weatherisation, the transformation of glass into clay bearing, glass free shards, see (Pearce et al., 2004), the occurrence of elongation features and the category of the material (glass, lithic or pumice). The length and breadth of each particle was measured with the software Scandium®. The measurements were made at 90° to one another. Statistical methods were employed to find potential clusters and to correlate between samples (see section 4.9.9).

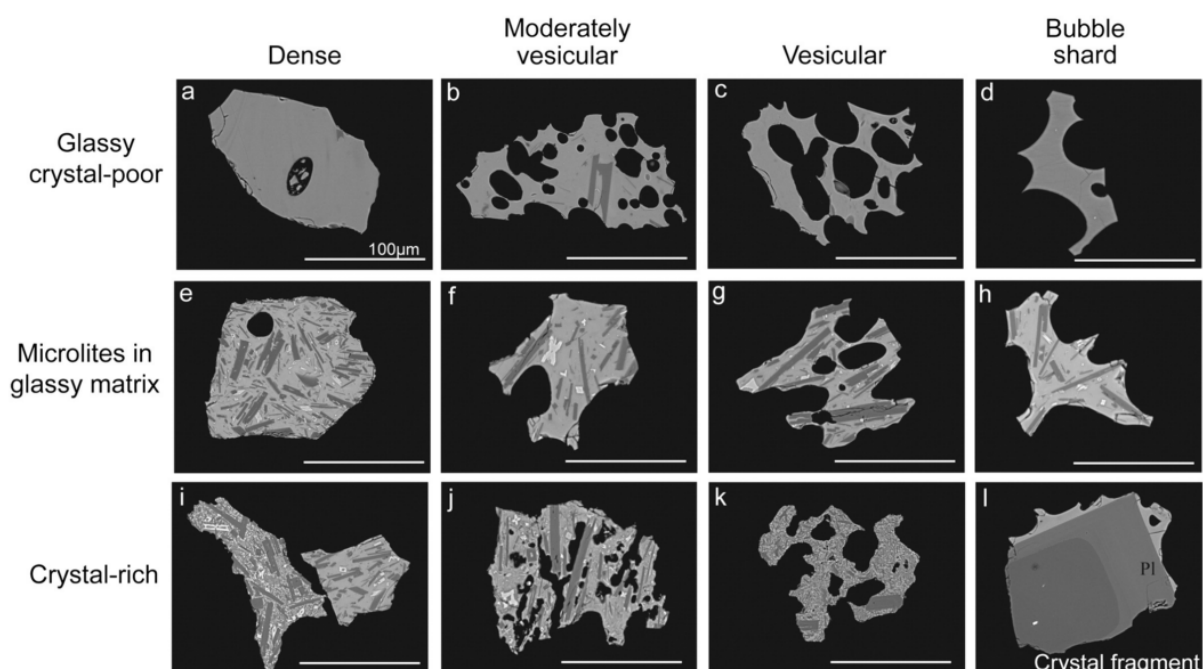


Fig. 4-7 Descriptive terminology for microscopic tephra classification. From Liu et al. (2015).

4.9.5 Total digestion

Total microwave digestion involves the use of high purity acids under high heat and pressure to completely dissolve silica based material into a liquid while preserving volatile elements (Taggart, 2002). This liquid can then be measured for various elements using an inductively coupled plasma mass-spectrometer (ICP-MS). Cleaned tephra samples were freeze dried and ground up using a mortar and pestle. Aliquots of 50 mg were removed from each sample and placed in cleaned (10% HNO₃) and dried Teflon vessels. The exact weight was noted as this is necessary to process the geochemical data. An aliquot from pure SPT was also weighed to check whether the samples were washed thoroughly. Each batch consisted of eight tephra samples, one blank to check for contamination as well as one certified reference material (CRM) to

estimate uncertainty. Recovery rates of 80-120% are determined as good. The CRM used here was Basalt Columbia River (BCR-2) collected in 1996 from the Bridal Veil Flow Quarry, Portland, Oregon, USA (Wilson, 1997). Into each Teflon vessel was added 2 ml HNO₃, 0.5 ml H₂O₂ and 2 ml HF. The vessels were closed tightly and inserted into the MLS-ETHOS (MLS GmbH) microwave at the Institute of Geography at the University of Bern which was run using two programmes (Table 4-3).

Table 4-3 Microwave settings for the first programme.

Time (min)	Power (W)	Temperature (Celsius)
5	300	120
10	700	200
30	450	200
20	-	cooling

Once sufficiently cooled and opened, 10 ml 6% H₃BO₃ was added to each vessel. The vessels were closed tightly once again and inserted into the microwave which was run using a second programme (Table 4-4).

Table 4-4 Microwave settings for the second programme.

Time (min)	Power (W)	Temperature (Celsius)
5	350	180
10	750	180
20	450	180
20	-	cooling

Once sufficiently cooled and opened, the liquids were transferred into flasks and deionized water was added to 50 ml. The flasks were shook three times and the contents poured into labelled plastic bottles which were kept refrigerated until analysis.

4.9.6 Geochemical analysis and processing

Through the inductively coupled plasma mass-spectrometer it is possible to detect and quantify elements in solution. The solution is nebulized and transported to plasma where the analytes are atomized and ionized. The ions are extracted and separated according to their mass-charge ratio. The signals created and recorded in the detector are evaluated by the machine's software. Using a calibration with standard solutions it is possible to make a quantitative determination of the concentration of an element in the sample (Rüdel et al., 2011). The totally digested liquid samples were diluted 10 times for trace elements and 200 times for major elements using 1% HNO₃. A calibration using a cocktail of different standard elements (Table 4-5) was produced using different dilutions (x 0.1, 0.5, 1, 5, 10, 50, 100, 500 and 1000) to cover the working range

in order to calculate concentrations. Standard material was not available for some elements (Table 4-5) so only count per second data can be measured for those. Due to total digestion through HF, Si cannot be measured as the digestion volatilized silica in proportions which cannot be known. The samples were measured using both He gas and no gas configurations. Some elements such as Y, Nb and Hf were measured as trace elements when they should have been measured as major elements as their concentrations were beyond the calibration curve's highest value. An internal standard (Rh) was used to correct any matrix effect (Thomas, 2001).

Table 4-5 Measured elements and elements without standards available.

Standards available	Standards not available
Na, Mg, Al, K, Ca, Sc, Mn, Fe, Sc, Ti, Si, Re, Zr, Mo, V, Cr, Co, Ni, Cu, Zn, As, Se, Rb, Sr, Cd, Ba, La, Ce, Pr, Nd, Sm, Eu, Gd, Dy, Ho, Er, Tm, Yb, Lu, Hf, Ta, Hg, Tl, Pb, Th, U	Y, Nb, Sn, Sb, Bi

Pre-processing the ICP-MS data was as follows:

1. Check the row labelled "rinse" and the 1, 10, 50 and 100 calibration concentrations. All the values should be close to their respective weighed numbers indicating no pollution. The "rinse" row should have values close to or below the method's detection limit which is calculated by the software.
2. Plot all the 1, 10, 50 and 100 calibration concentrations values to check for drift which may have to be corrected if the values deviate from a straight line. Values up to $\pm 10\%$ are acceptable.
3. Take out all reference material rows and calculate based on their weights the actual concentration of each element. The formula follows that of Rüdél et al. (2011):

$$\omega_E = V / M * \rho_E * F \quad (9)$$

Where ω_E is the proportion by mass of the element in the solid matter ($\mu\text{g/g}$), M is the mass of the sample used (mg), V is the volume to which the sample is replenished (mL), ρ_E is the concentration of the element under consideration in the digested solution as measured by the machine ($\mu\text{g/L}$) and F is a conversion factor ($1 \text{ L} / \text{mL} * \text{mg/g}$).

4. Calculate the percent recovery between the aqueous certified reference sample (BCR2) and the sample reference values.

$$(\text{Measurement} / \text{CRM}) * 100 = \text{Recovery} \quad (10)$$

5. Compare to CRM certificate (see Wilson 1997). Values on the certificate are reported as Wt % (weight percent) so that if it is 1.5% then it means 15000 mg/g. The deviation from the target values should be $< \pm 20\%$.
6. Investigate the recovery values. Good values are 80-120% (mark as green), mediocre (50-150% mark as orange). Based on this one can choose which isotope to use for a certain element and whether to use measurement from He gas or no gas.
7. Check the blanks for contamination. Values $< 5\%$ of sample concentration values are acceptable.
8. For each triplicate, find the average and standard deviation. Standard Mean Error (SME) and 95% confidence intervals may be calculated. The representation of error for samples which were not triplicated must be consistent and the procedure noted.

9. Reproducibility can be checked from the relative standard deviation (RSD) which should be < 10%.
10. Calculate all the element concentrations as in step 3 above.

4.9.7 Compilation of the datasets

Two sets of data were produced. The first set contained morphological and colour characteristics. The second set contained the geochemical characteristics produced from the total digestion and ICP-MS measurements in sections 4.9.5 and 4.9.6. The geochemical data was assessed for accuracy through the recovery rates of the laboratory reference material compared to the certified elemental concentration values of the CRM. Based on the CRM recovery values, batch 1 concentrations were adjusted so the recovery for each element would match the average of the other batches. In a similar case, the samples in batch 5 were digested and measured a second time in batch 6 and measured a third time as batch 7. As a result, a compilation of well recovered elements from batch 5/6/7 was produced and will be referred to as batch 5mix onwards. As the recovery rate varied between elements, two datasets were produced. The first dataset, called A1 dataset, contains only the elements for which good CRM recovery was found. Good recovery is taken to be in the range of 80 - 120% of the CRM. This dataset also contained the corrected batch 1 values. The second dataset, called B2 dataset contained all elements, even those with poor recovery such as the REE (**Table 4-6**). ⁴³Ca, ⁴⁴Ca, Gd, Mo, Th and ⁴⁵Sc were the only elements left out due to their low recovery in all batches. Batch 1 is not corrected in the second dataset. In both datasets, batch 5mix is used according to the CRM recovery values. Data from batch 6 for EST15-1-A were erroneous, so batch 5 values were used for Na, Al, K, Mn and Fe.

Table 4-6 Geochemical datasets used in this study and the elements they contain.

A1 dataset	B2 dataset
Na, ⁵⁷ Fe, Ba, Ti, V, Co, Cu, Rb, Zr, La, Ce, Eu, Yb, Pb, U (15 elements)	Na, Mg, Al, K, Mn, ⁵⁷ Fe, Ba, Ti, V, Cr, Co, Cu, Zn, Rb, Zr, La, Ce, Pr, Nd, Sm, Eu, Gd, Ho, Tm, Yb, Pb, U (27 elements)

4.9.8 Data visualization and description

Line plots were produced for the A1 dataset only including the elements listed in Table 4-6. The line plots were made using the software Grapher. The lines indicate the signature of each tephra layer and are used to correlate between layers. To aid layer correlations, each tephra was described in terms of its location in the core, morphological features, colour and chemical analysis. An approximate age based on radiocarbon dating is also assigned.

4.9.9 Statistical analysis of the datasets and tephra classification

In order to correlate the tephra layers some exploratory data analysis was carried out on the A1 and B2 datasets as well as the colour and morphological dataset. The data was first screened for outliers using biplots and standardized to a mean of 0 and standard deviation of 1 to remove potential influence of scale. The standardized datasets were only used for certain methods such

as Principal Component Analysis (PCA) as well as constrained and unconstrained cluster analysis but not the similarity coefficient analysis.

Exploratory data analysis

Exploratory methods included using principal component analysis (PCA) to identify the important elements and reduce the dimensionality of the data. PCA was attempted for both geochemical datasets and the resulting principal components were listed and the loadings plotted as heat maps. In the first instance, the number of significant principal components was determined from the scree plot through the broken stick method. Investigating each pair of PC loadings would allow for the identification of pairs of elements which would show most discrimination of the tephra layers when plotted in elemental x-y biplots. The most discriminating pairs were those with opposite loadings in different PCs. The resulting biplots reduced the dataset to be analysed and were visually investigated for sample overlaps to help with the correlation.

Similarity coefficient (SC)

The SC developed by Borhardt et al. (1972) was used as a quantitative basis to correlate layers. The method uses a weighted average of ratios of each element between two pairs of layers. The result is a dimensionless number from 0 to 1 where 1 is an identical match. The SC was used on all elements which had good recovery. Weights were assigned based on the significance of the element and its analytical recovery. The standard deviation of the samples can also be included (e.g. Rodbell et al. 2002) but here standard deviations were only available for a fraction of the samples. The SC is calculated as:

$$d_{(A, B)} = \frac{\sum_{i=0}^n Ri}{n} \quad (11)$$

where $d_{(A, B)}$ is the similarity coefficient for comparison between sample A and sample B; i is the element number; n is the number of elements; $R_i = X_{iA} / X_{iB}$ if $X_{iB} \geq X_{iA}$ and $R_i = X_{iB} / X_{iA}$ if $X_{iA} > X_{iB}$; X_{iA} is the concentration of element i in sample A and X_{iB} is the concentration of element i in sample B. SC was attempted using the unstandardized geochemical A1 and B2 with all weights set to 1. Values equal or greater than 0.90 represent pairs which are very highly similar while those between 0.80 and 0.89 and represent those that are only highly similar. The resulting matrices were compared. Furthermore, spider diagrams were used to make sense of the results.

Cluster analysis

Cluster analysis was used to determine the number of possible tephra horizons as well as correlating between samples. During all analyses, stratigraphical constraints were kept in mind: a minimum of 7 tephra groups had to exist as this number of tephra layers were found in a single core. This prior knowledge was applied to the cluster analyses to discard results with fewer

groups. Both constrained and unconstrained methods were attempted on all three A1, B2 and morphological datasets. All methods were tried and compared.

Unconstrained cluster analysis

Unconstrained clustering analyses using average, complete and single linkages and Ward's method were employed to group the tephra layers based on their SC scores for the A1 and B2 datasets. Multiple techniques were tested in order to assess the robustness of the clusters. Three different programs were run: using the PAST software and two different functions in R called "hclust" and "pvclust" (Hammer et al., 2001; Suzuki and Shimodaira, 2006; R Core Team, 2015). The "pvclust" calculates p-values for hierarchical clustering via multiscale bootstrap resampling. It therefore gives probability values for each cluster. All methods were compared to one another to find the number of clusters possible and probable sample group members. Also known as agglomerative cluster analysis, this bottom up technique starts with single observations and pairs them to their nearest cluster. The result is an evolutionary tree or dendrogram which can be cut to obtain a number of clusters (Wilks, 2011). Unconstrained analysis means it is not forced to stay within stratigraphic order. Methods were discarded if the resulting number of groups was below 7.

K-means cluster analysis

In a further step, cluster plots using k-means clustering with k clusters was attempted for all datasets. K-means is a non-hierarchical clustering method which allows the reassignment of observations (Wilks, 2011). The number of groups must be specified in advance. The k clusters were determined from the dendrograms in the previous step. The clusters were calculate and plotted using the function "clusplot" with the R software (Pison et al., 1999).

4.9.10 Tephra stratigraphy

Tephra stratigraphy has been used successfully in the literature as described in Chapter 3. In this study, the statistical analysis of geochemical fingerprints as well as the colour and morphological classification were combined with the chronology produced from radiocarbon and ²¹⁰Pb dating. Always taking the layer stratigraphy for each lake into account as the main parameter, a tephrostratigraphy for CNP was attempted using all statistical methods and visual analyses mentioned above. As a last objective, the literature was scrutinized to find the source eruptions of these layers.

5 Results

5.1 Age-depth models of the Cajas NP lakes

5.1.1 L. Llaviucu

²¹⁰Pb model

The ²¹⁰Pb age-depth profile for L. Llaviucu was investigated using the CIC and CRS models. Supported activity averaged 29 ± 3.2 Bq/kg throughout the profile and the unsupported activity reached background level at 23.15 cm depth. The CIC model was discarded because this model assumes that the sedimentation rate remains constant which is not the case in this lake and resulted in age reversals at 0.25, 1.5, 2.75 and 4.25 cm depth. A missing inventory correction of 395.86 Bq/m^2 derived from an exponential trend over the whole profile was applied to the CRS model following the procedure by Tylmann et al. (2013) and Binford (1990). The correction reduces the tailing effect which is otherwise seen at the bottom of the other uncorrected CRS models. The corrected CRS yielded more plausible results than the other two models when considering the shape of the profile. **Fig. 5-1** shows the total ²¹⁰Pb activity, the supported activity as well as the CRS age-model and the resulting mass accumulation rate (MAR). The measured ¹³⁷Cs activity was low, averaging 2.5 ± 1.1 Bq/kg. As a result, the 1963 fallout peak could not be used as an event marker to constrain the ²¹⁰Pb CRS model. The MAR varied between 0.03 and 0.22 $\text{g cm}^{-2} \text{ yr}^{-1}$ through-out the profile with a sharp increase at a depth of 15 cm. From that depth onwards the MAR fluctuates widely.

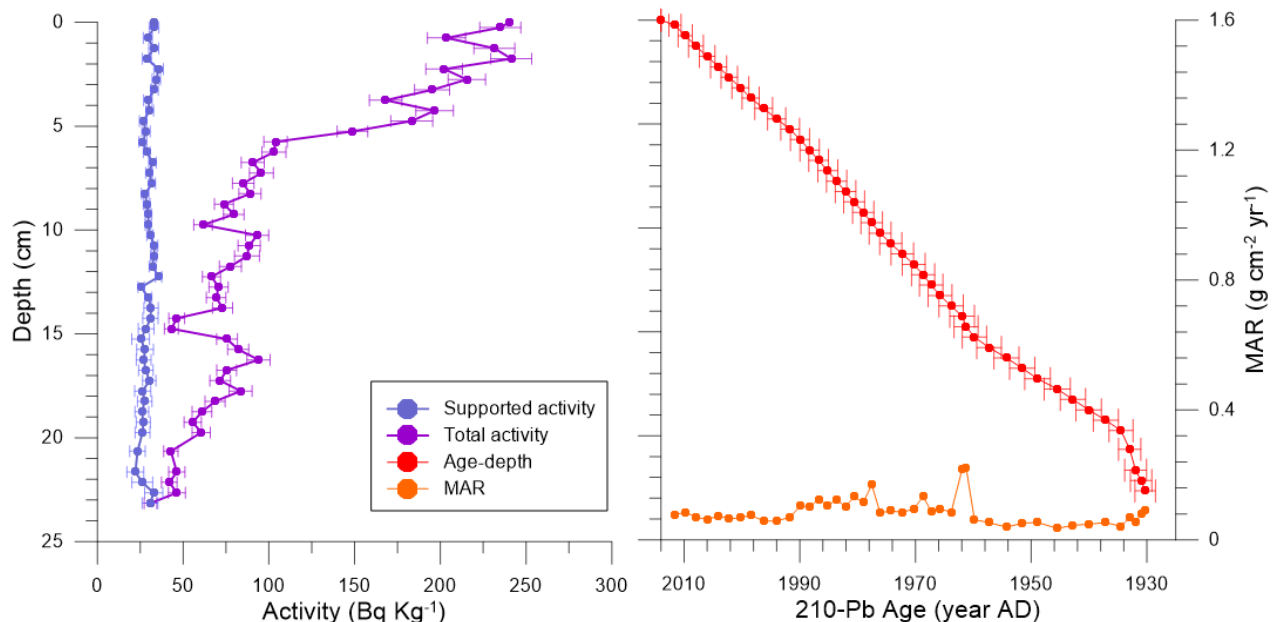


Fig. 5-1 Raw lead data and CRS age-depth model with missing inventory corrections for L. Llaviucu.

Combined age-depth model

An age-depth model was constructed for L. Llaviucu using ^{210}Pb to 23.15 cm and radiocarbon dating to 185 cm, close to the end of core LLA15-6-II using the BACON (**Fig. 5-2**) and the CLAM software (Blaauw and Christen, 2011; Blaauw, 2010). The BACON model was preferred over the CLAM model to produce the age-depth profile as one macrofossil date exhibiting age reversal at 21 cm depth could not be corrected. The reversal was assigned to a large age uncertainty of 150 years. However, the flood deposit corrected age model could only be produced using the CLAM model. The lowest sample (LLA15-6d) revealed a minimum age of 2923 (-615 +1062) cal. yr BP at 182.50 cm depth. The radiocarbon dates available as well as the material on which they were measured and the estimated total weights are detailed in **Table 5-1** and images of the samples can be found in **Plate I**. Samples LLA14-1b, LLA14-1d, LLA15-6b and LLA15-6d were removed from the model because they displayed age reversals caused by a reservoir effect. The reservoir effect did not appear to be constant in time (ranging between 300 and 500 years) so the ages could not be corrected. The ^{14}C yr BP dates were calibrated using IntCAL13.14C (Reimer et al., 2013).

Table 5-1 Organic material and their depths and radiocarbon calibrated ages based on IntCAL13.14C (Reimer et al., 2013) for L. Llaviucu. MF stands for macrofossil. The type of MF can be seen from Plates I and II.

Sample Label	Depth (cm)	Material	Total weight (μg)	uncal yr BP	\pm yr	Procedure	Cal. yr BP (max probability)	Min/max (1σ)
LLA14-1a	21.15	MF	405	157	78	Gas	154.5	-4, 313
LLA14-1b	21.15	Bulk	678500	682	34	Graphite	657.5	632, 683
LLA14-1c	55.45	MF	2804	317	22	Gas	402.5	348, 457
LLA14-1d	55.45	Bulk	868.6	891	22	Graphite	770.5	737, 804
LLA15-6a	59.50	MF	648	332	44	Graphite	397	306, 488
LLA15-6b	61.30	MF	65	2378	235	Gas	2419.5	1881, 2958
LLA15-6c	73.00	MF	27	1274	171	Gas	1219.5	905, 1534
LLA15-6d	110.55	Bulk	891500	2248	23	Graphite	2207	2158, 2256
LLA15-6e	182.50	MF	43	2923	356	Gas	3146.5	2308, 3985

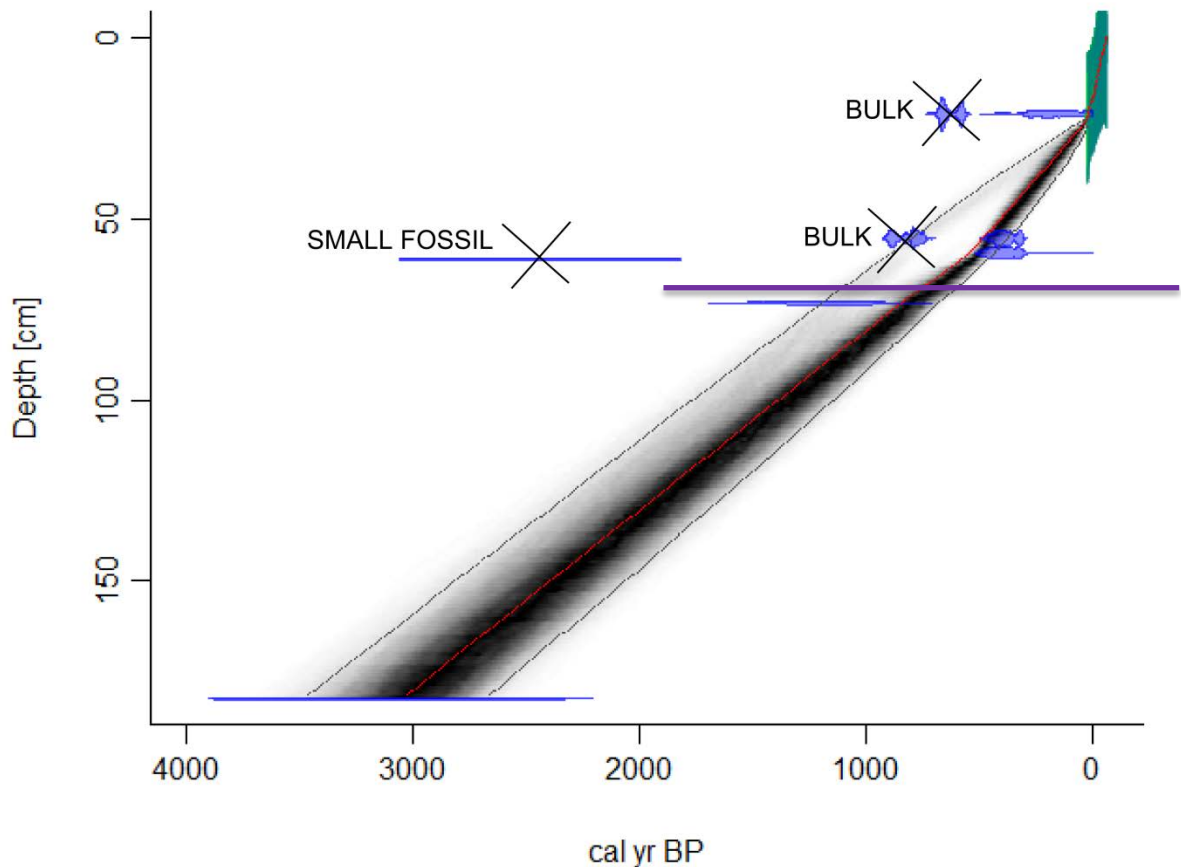


Fig. 5-2 Age-depth model for L. Llaviucu created from Markov Chain Monte Carlo iterations using the BACON software (Blaauw and Christen 2011). The darker shading represents the most likely age range at 95% confidence. The red line represents the weighted mean. The probability distributions of the radiocarbon calibrated dates upon which the model is based are displayed as light blue mirror histograms. Refer to Blaauw and Christen (2011) for further details of the method. The ^{210}Pb dates are shaded green. Samples above and below the purple line originate from different L. Llaviucu cores.

Flood layer corrected age-depth model

The CLAM model was preferred to produce a corrected age-depth model. Tephra and flood layers were removed from the CLAM modelling under the assumption that they deposited instantaneously (**Fig. 5-3**). The resulting age-depth profile is much flatter than the non-corrected version but this flattening is expected (e.g. Wirth et al. 2013) because depth is removed. However, the model still contained an age reversal at 21 cm depth which can be explained by the large age uncertainty of sample LLA14-1a (**Table 5-1**). The point at which the ^{210}Pb and the radiocarbon ages join may be coinciding with a sediment rate increase as seen from the steeper slope after the 1900s.

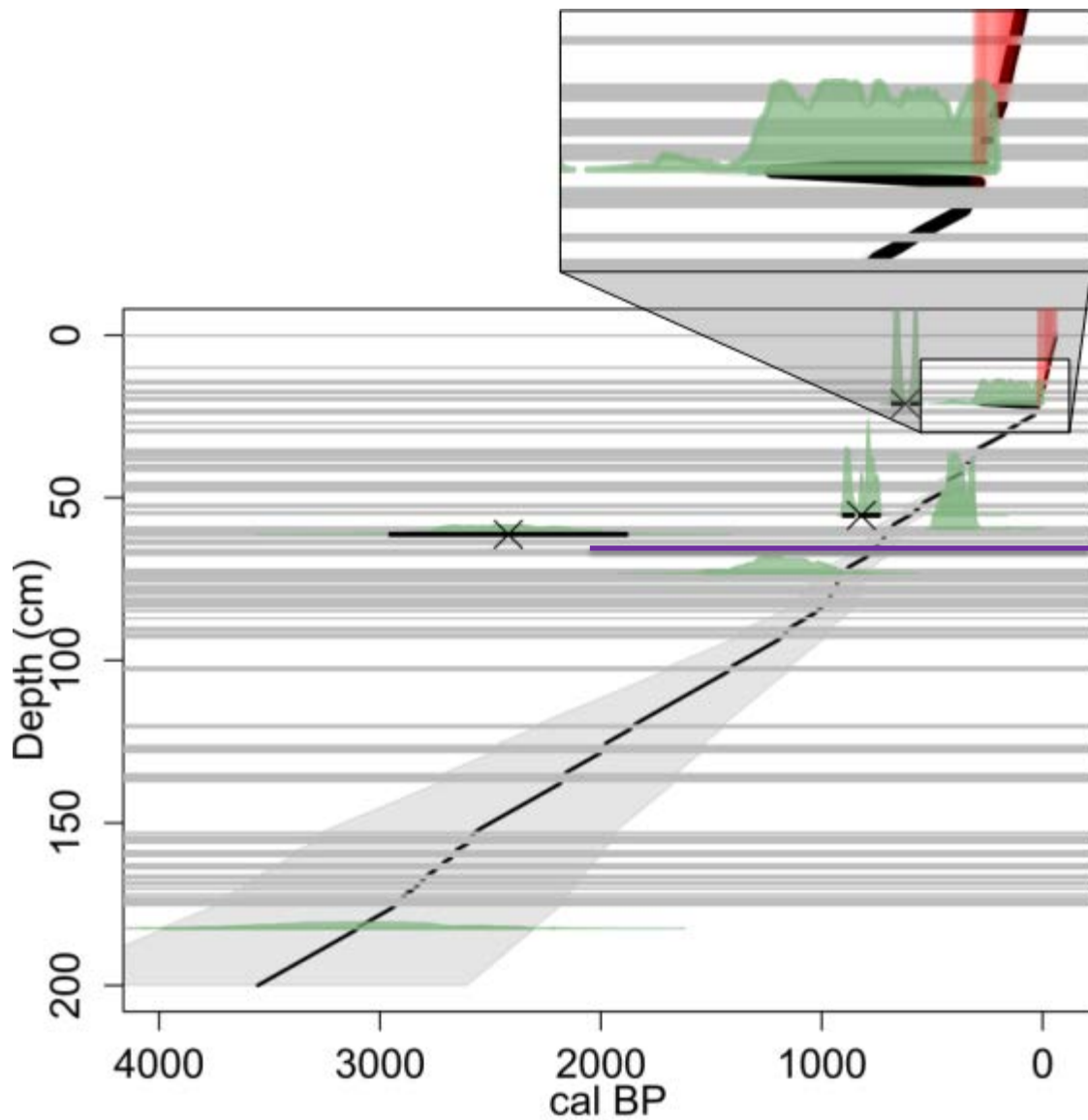


Fig. 5-3 Flood layer corrected age-depth model (linear regression) using the CLAM model (Blaauw 2010). The light grey area encloses the 95% confidence limits based upon 1000 iterations. The solid line represents the weighted mean. The probability distributions of the radiocarbon calibrated dates upon which the model is based are displayed as light green histograms. ^{210}Pb dates are displayed in red. Samples assumed to be outliers are crossed out. Age reversal can be seen at a depth of 21 cm in the inset zoom. Grey horizontal lines indicate the flood and tephra layers which have been removed. Samples above and below the purple line originate from different L. Llaviucu cores.

5.1.2 L. Fondococha

^{210}Pb model

The ^{210}Pb age-depth model for L. Fondococha was attempted using two different models: CIC and CRS (Fig. 5-4). Supported activity averaged 52.1 ± 4.8 Bq/kg throughout the profile and the unsupported activity reached background level at 8.25 cm depth. The CIC model was discarded because this model assumes that the sedimentation rate remains constant which is not the case in this lake and resulted in age reversals at 0.75, 3.25 and 5.50 cm depth. The CRS yielded more plausible results than the CIC model. Fig. 5-4

shows the total ^{210}Pb activity, the supported activity as well as the CRS age-model and the resulting sediment accumulation rate (SAR). A missing inventory correction of 38.8 Bq/m^{-2} derived from an exponential trend over parts of the profile was applied to the CRS model following the procedure by Tylmann et al. (2013). The measured ^{137}Cs activity was low, averaging $5.6 \pm 3.0 \text{ Bq/kg}$. As a result, the 1963 fallout peak could not be used as an event marker to constrain the ^{210}Pb CRC model. SAR showed little variation between 0.005 and $0.025 \text{ g cm}^{-2} \text{ yr}^{-1}$ throughout the profile. The CRS model gives an age of 1874 at a depth of 8.25 cm.

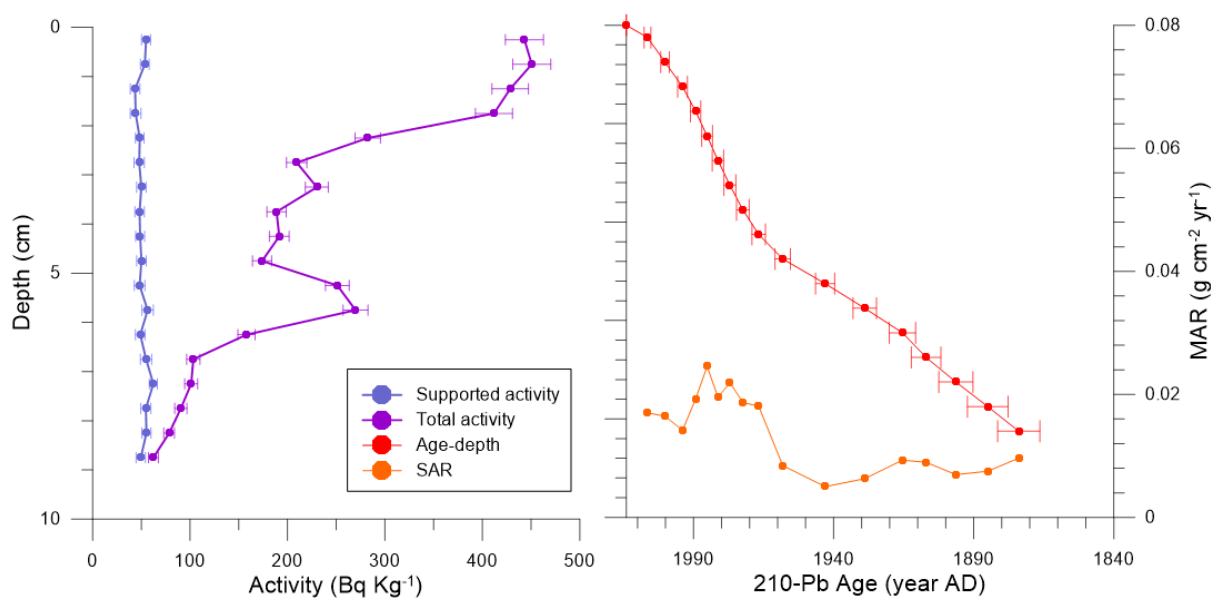


Fig. 5-4 Raw lead data, SAR stands for sediment accumulation rate and CRS age-depth model with missing inventory corrections for L. Fondococha.

Combined age-depth model

An age-depth model was constructed for L. Fondococha radiocarbon dating to 67.5 cm using the BACON (Fig. 5-5) and the CLAM programme. The radiocarbon dates available as well as the material on which they were measured and the estimated carbon weights are detailed in Table 5-2 and images of the samples can be found in Plate II: Macrofossils L. Fondococha. Sample FON14-2Bulk was removed from the model because it displayed an age reversal caused by a reservoir effect of approximately 500 years. No other bulk sample was measured to investigate whether the reservoir effect remained constant in time so the age could not be corrected. The ^{14}C yr BP dates were calibrated using IntCAL13.14C (Reimer et al., 2013). The age-depth model reveals a minimum age of 1121 (min 977, max 1255) cal. yr BP at 67.5 cm for the BACON model and 1012 (min 918, max 1138) cal. yr BP for the CLAM model at 67 cm depth. The results are very similar and Fränkl (*per. communication*) showed that the year 1986 would correspond to a depth of 2.5 cm in Fondococha based on a mercury concentration profile. This agrees well with both profiles. However, the BACON model is more conservative, giving wider age uncertainties. Based on this, and the observation that the age-depth profile is straighter, the BACON model was used further and the CLAM model discarded.

Table 5-2 Organic material and their depths and radiocarbon calibrated ages based on IntCAL13.14C (Reimer et al. 2013) for L. Fondococha. MF stands for macrofossils and the specific type of material is displayed in Plate II.

Sample Label	Depth (cm)	Material	Total weight (μg)	uncal yr BP	\pm yr	Procedure	Cal. yr BP (max probability)	Min/max (1σ)
FON14-2a	26.65	Bulk	963000	940	26	Graphite	857.5	795, 920
FON14-2b	26.65	MF	195	301	62	Gas	389.5	276, 503
FON15a	40	MF	1217	726	38	Graphite	688	648, 728
FON15b	67.50	MF	619	1080	51	Graphite	1003.5	919, 1088

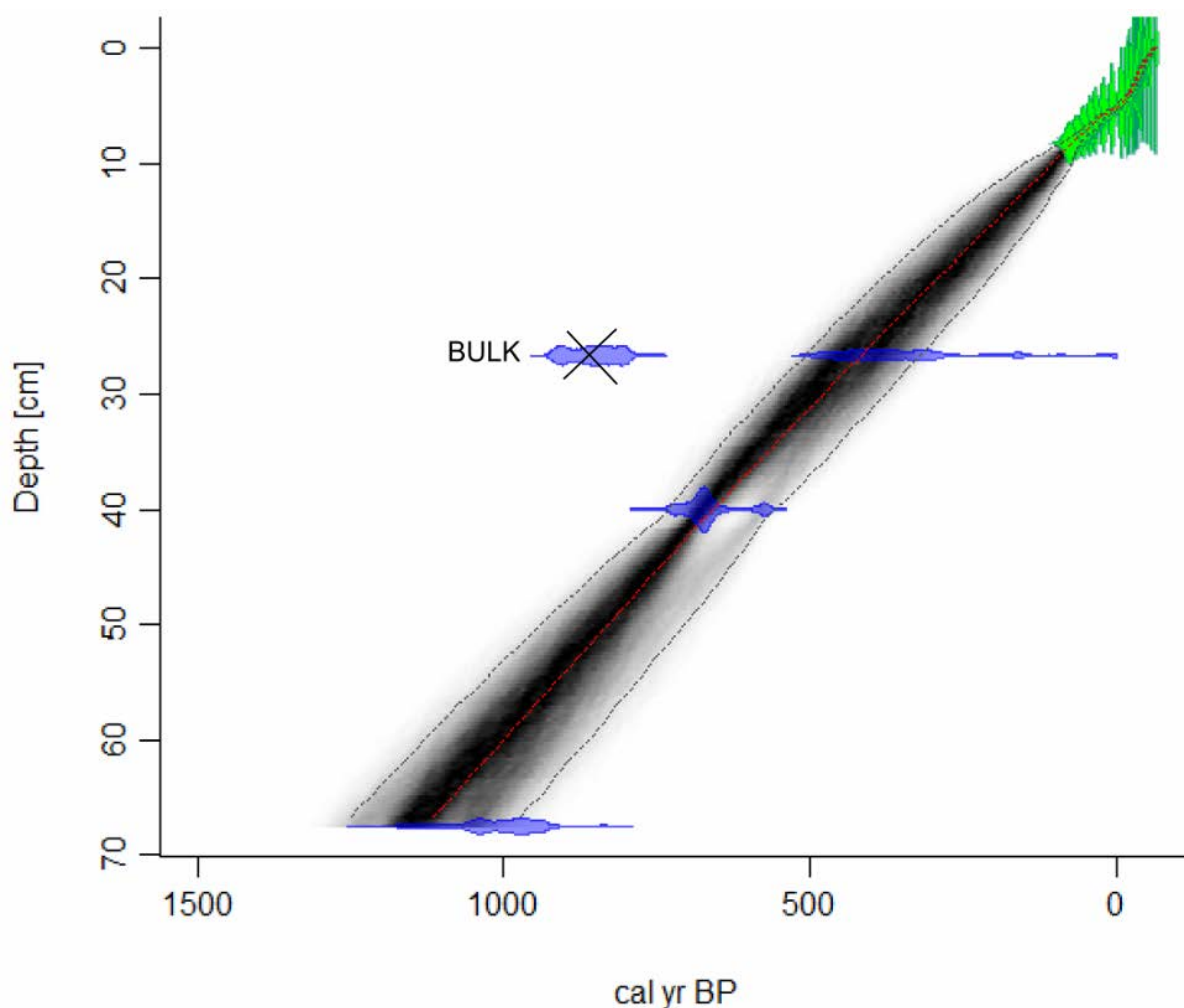


Fig. 5-5 Age depth model for L. Fondococha created from Markov Chain Monte Carlo iterations using the BACON software (Blaauw and Christen, 2011). The darker shading represents the most likely age range at 95% confidence. The red line represents the weighted mean. The probability distributions of the radiocarbon calibrated dates upon which the model is based are displayed as light blue mirror histograms. Refer to (Blaauw and Christen, 2011) for further details on the method. ^{210}Pb dates are shaded green.

5.2 L. Llaviucu flood frequency

5.2.1 L. Llaviucu sediment description

Three L. Llaviucu sediment cores have been described in detail (**Fig. 5-7**). The cores are composed of two units. The matrix of unit I is organic rich silt with layers of plant macrofossils (**Fig. 5-**). Silty lightly coloured bands are also visible within this unit. The Munsell colours range from brownish black (10 YR 3/1) for background sedimentation to olive yellow (5Y 6/4) for the laminae. Unit II is also organic rich silt but organic layers are no longer present. Banding and laminations become more frequent and range in their Munsell colour varying from light grey (10YR 7/2) to greyish olive (7.5 YR 6/2). Layers with gradual contacts are present in both units. Tephra layers are only present in unit II.

5.2.2 L. Llaviucu master core

A master core was produced for L. Llaviucu by combining LLA14-1, LLA14-2 and LLA15-6 by using two layers as tie points. These two tie point layers are highlighted in red and blue in **Fig. 5-6** and a more detailed correlation is also provided. The master core length is now 188.8 cm and is visualised in **Fig. 5-6**. The first break is at 60 cm in LLA14-1 and the second section is 62.3 – 84.8 cm in LLA14-2 and the third is 80 – 187 cm in LLA15-6. Depth correlations are listed in **Table A4-1**.

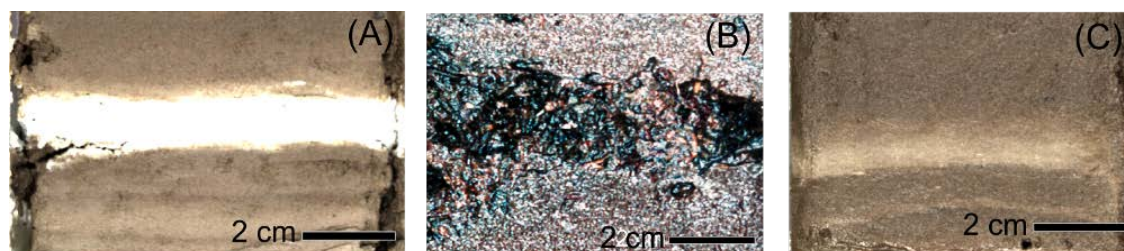


Fig. 5-6 Example of (A) tephra (Td in Fig. 5-), (B) organic rich (30 cm depth in LLA15-6 (top)) and (C) flood layer (130 cm depth in LLA15-6 (bottom)).

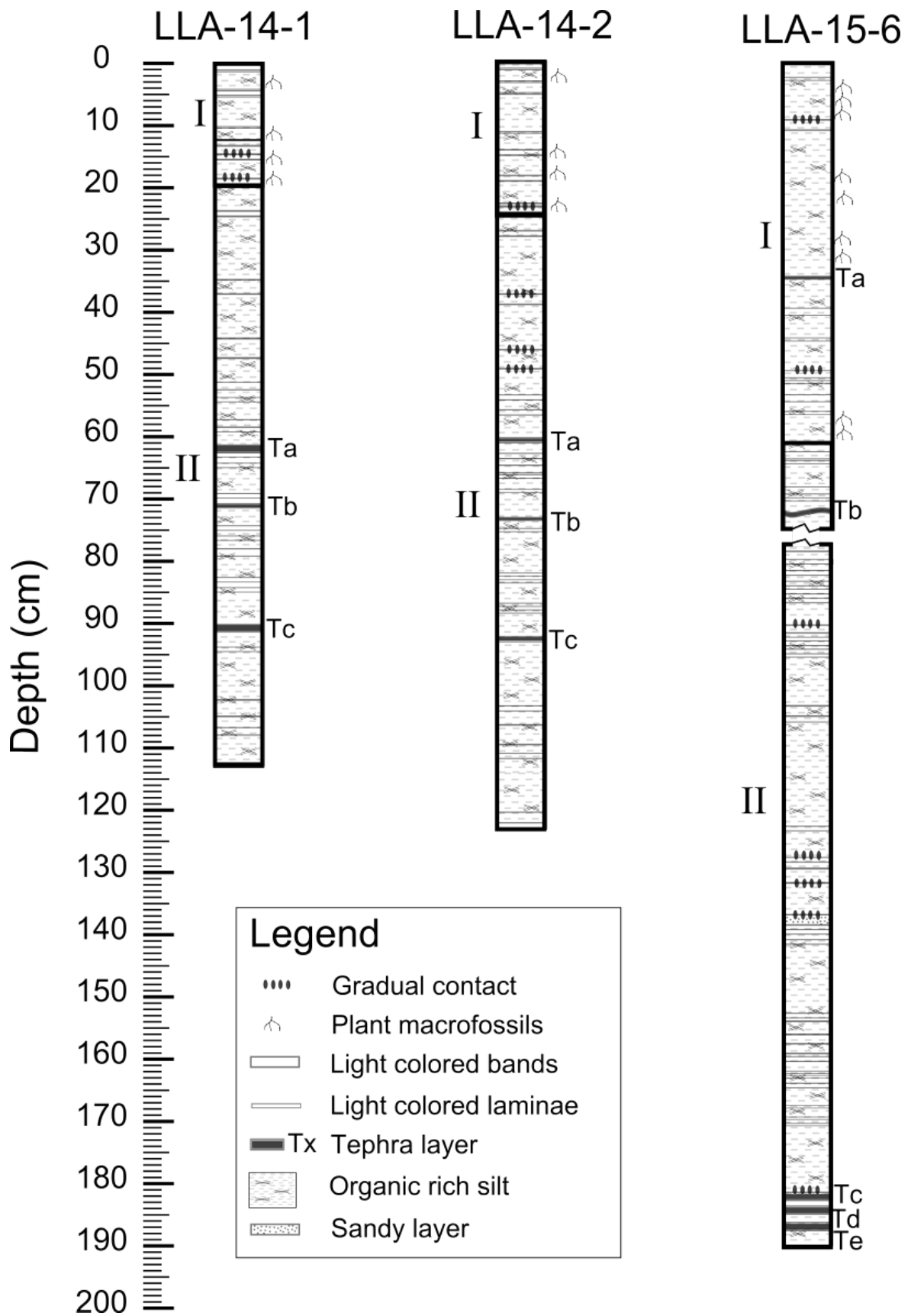


Fig. 5-7 Sediment descriptions of L. Llaviucu 2014 and 2015 cores. Descriptions of the 2014 cores were made in collaboration with T. Schneider.

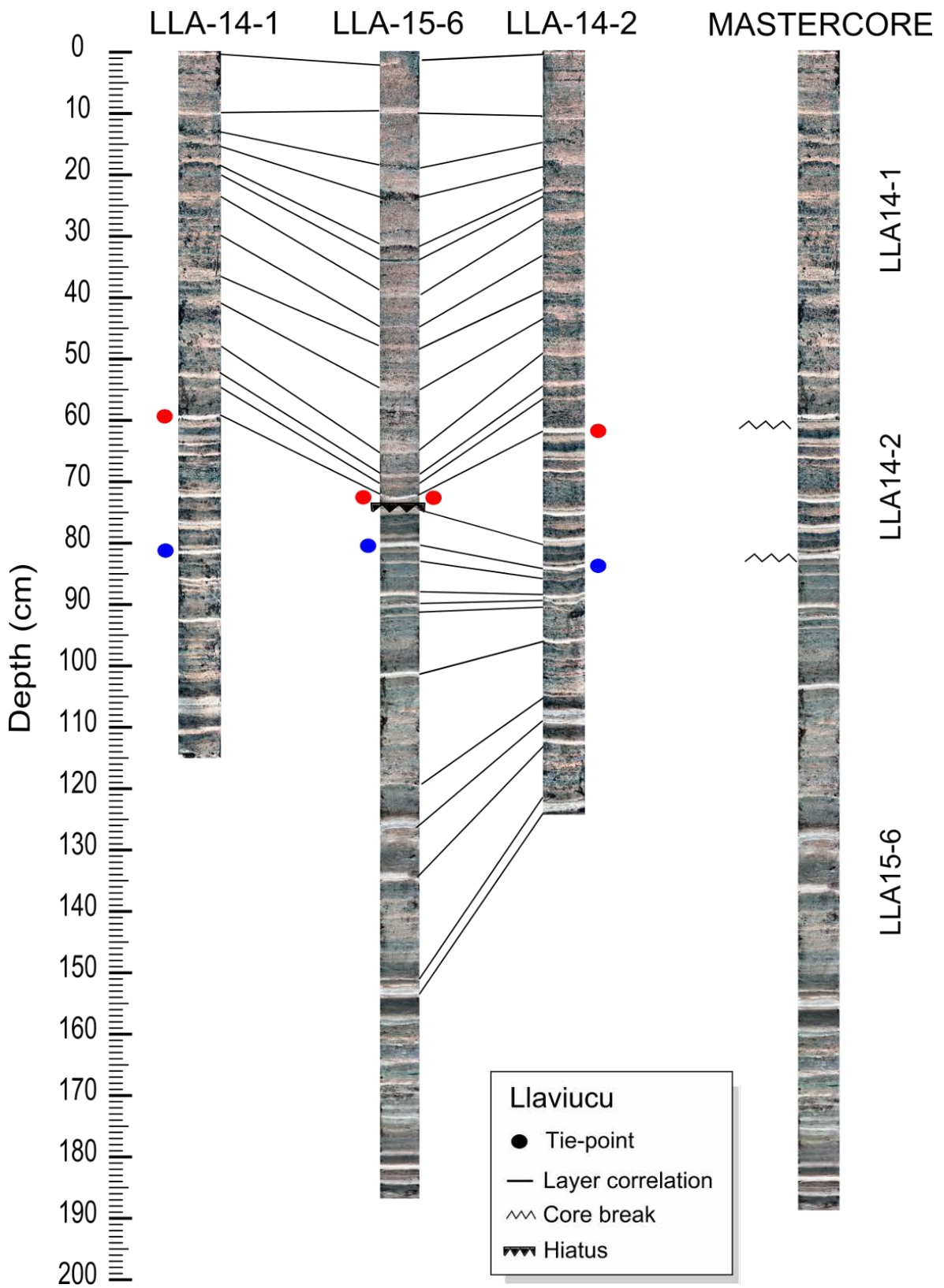


Fig. 5-6 Core correlation based on visual inspection and master core.

5.2.3 Flood layer classification

The flood layers in the sediment of the master core were determined visually with the support of supervised and unsupervised classification of the cores' spectral signatures using the ENVI image software, XRF data and visual inspection as described in section 4.5.

HI classification

The sediment cores were scanned with the HI scanner. During the normalisation routine, statistical analyses are calculated for quality control. The resulting TIFF-image displays mean spectral values which are lower than 7% reflectance in blue (Butz, 2016). Images with much blue coloration indicate very low reflectance and thus discrimination is problematic. **Fig. 5-7** shows examples of quality control for LLA-14-1, LLA14-2 and LLA15-6 (top). The images are largely covered in blue indicating a poor image quality. However, some of the flood layers show higher reflectance.

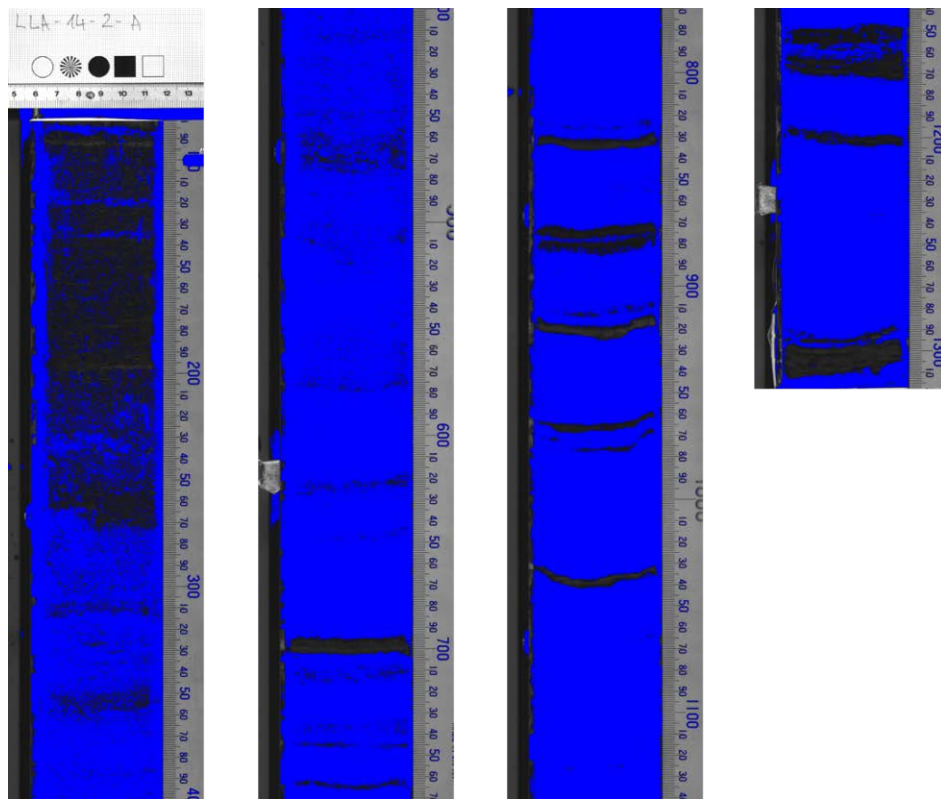


Fig. 5-7 Example of quality control for LLA14-2 (split for display). The blue areas indicate reflectance values <7%.

Bearing in mind the quality of the data, the hyperspectral core images have been analysed based on the different classification methods explained in section 4.5.3. The best results were retrieved from the unsupervised classification procedure (**Fig. 5-8**). The flood layers classified in this way resulted in incomplete identification as some layers were not “seen” by the statistical procedures as the layers were too thin or only faintly visible. In addition, the classification is likely to be different for LLA-15-6 (bottom) than for LLA14-1 or LLA14-2 as the range of spectral values is different. Thus

it is difficult to interpret the yellow zones between the former and the latter. In LLA-15-6 (bottom), yellow zones may relate to tephra while in LLA14-1 or LLA14-2 these may relate to clastic sediment.

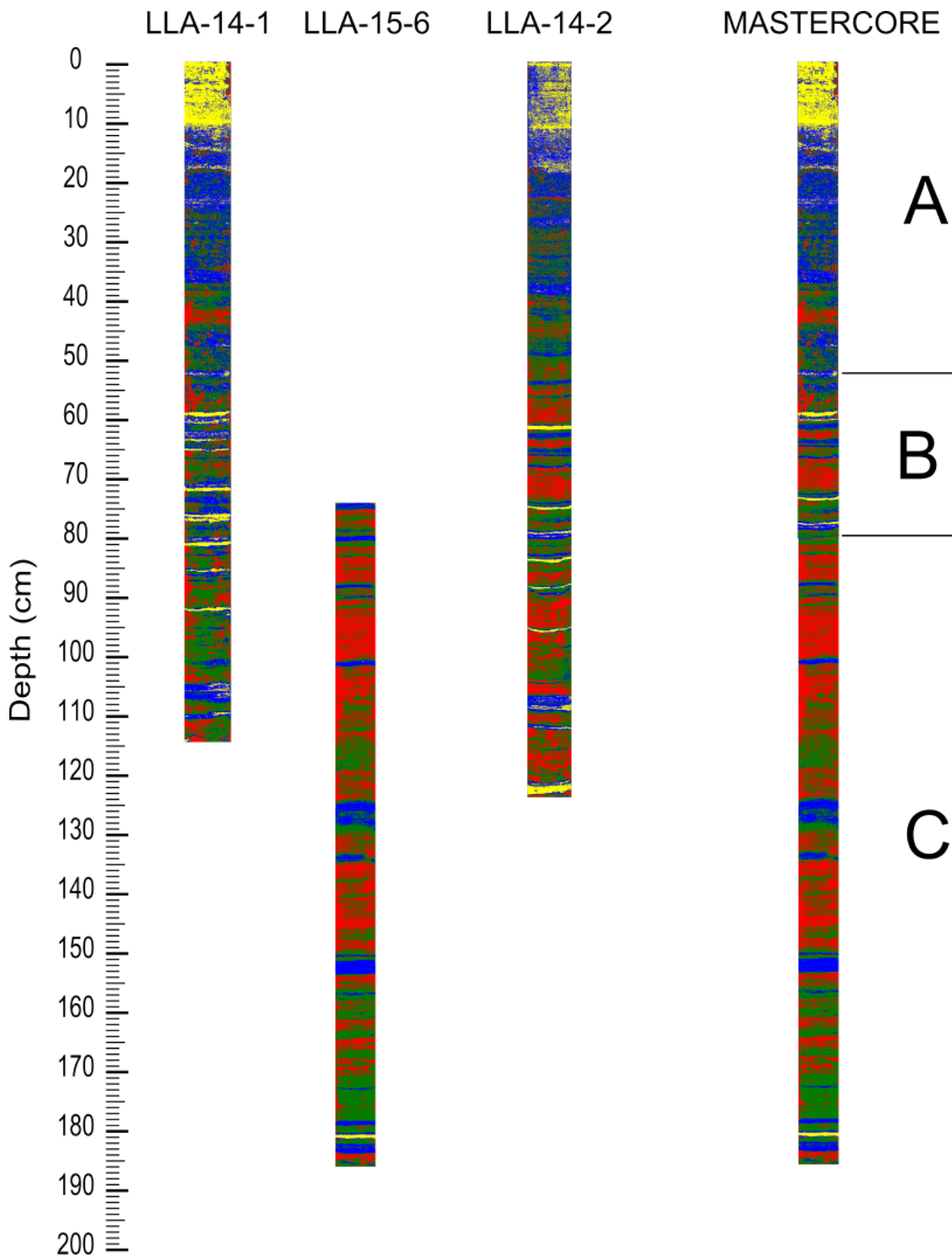


Fig. 5-8 Unsupervised layer classification of LLA14-1, LLA14-2 and LLA15-6 (bottom half) using the ISODATA classification workflow, 4 classes and 20 iterations for the threshold settings. Sections A, B and C in the master core relate to the sections from cores LLA14-1, LLA14-2 and LLA15-6 (bottom) respectively. Refer to the text for the colour interpretation.

XRF classification

The classification of the flood layers was also based on XRF data. Flood layers were found to contain higher counts of Ti, K, Fe and Rb. Zr was found to contain a low signal to noise ratio. The elements Ti and K were found to co-vary down core which is indicative of input from the catchment (**Fig. 5-9**). Problematically, the tephra layers were also found to contain high K and Ti. However, previously identified tephra layers can simply be removed, leaving only the flood layers. The single elements may be influenced by the matrix and should be analysed as element to element or element to coherent-scatter ratios.

Final flood layer classification

The final classification is found in **Fig. 5-10** which excludes the tephra layers identified in section 4.9.1.

5.2.4 Flood frequency reconstruction

The final flood layer classification was used in conjunction to the flood-corrected CLAM radiocarbon and ²¹⁰Pb age-depth model to produce a flood frequency reconstruction (**Fig. 5-11**). The results show two types of periods. Sections I and III show higher frequencies of flood layers than section II. Section I contains 39 layers in approximately 1300 years and it appears that a peak in layer frequency was reached at around 1000 C.E. This period may end with the most recent event in 2011 (black cross in **Fig. 5-11**) or may be continuing in the future. Likewise, section III saw many extreme events particularly during the period 580 to 1039 B.C.E. By contrast, the other period type (section II) contains relatively few extreme events with 4 events in 1300 years during the period 579 B.C.E. to 711 C.E. The last 150 years saw a sharp increase in events. The 100 year moving window, although long in comparison to the full record, was chosen so as to match the reconstruction by Moy et al. (2002).

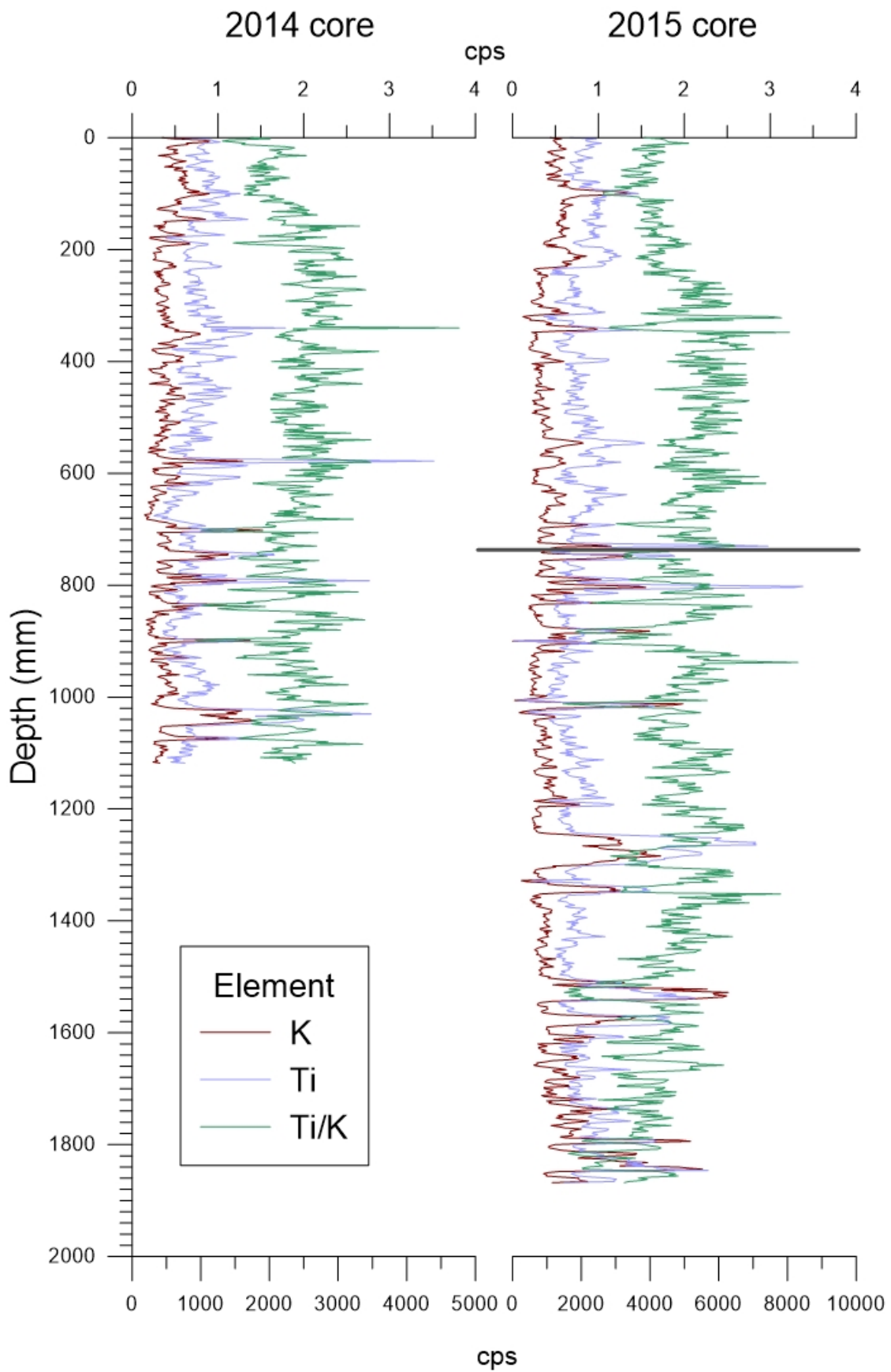


Fig. 5-9 Titanium (Ti) and potassium (K) XRF profiles for L. Llaviucu 2014 and 2015 cores. The grey line at 74 cm denotes the position where the 2015 core was split.

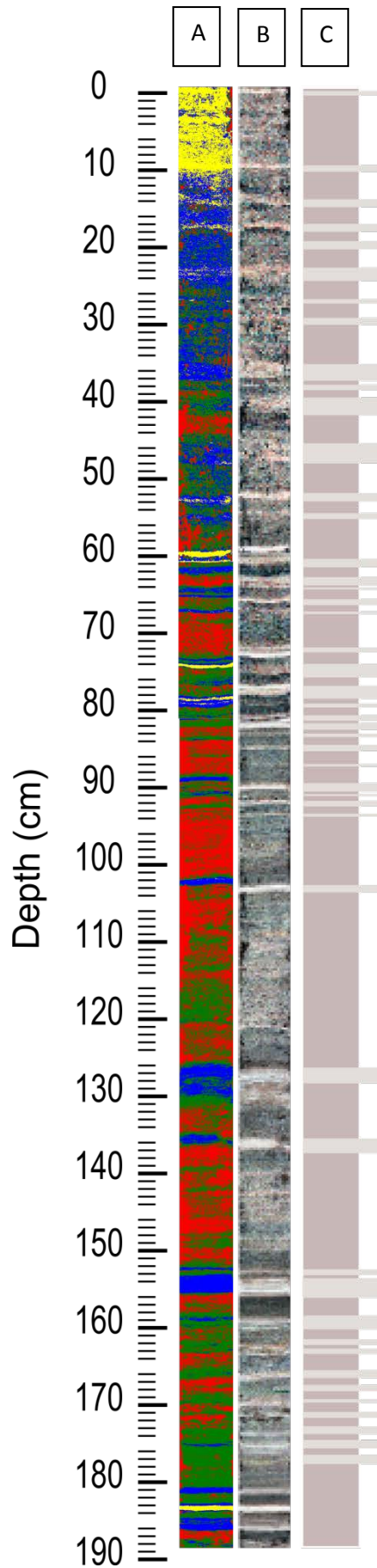


Fig. 5-10 Flood classification of the L. Llaviucu mastercore. Image A is the hyperspectral classification, image B is a colour infrared red image of the master core and C is a depiction of the flood layers excluding the tephra layers as produced from the combination of XRF, visual and HI.

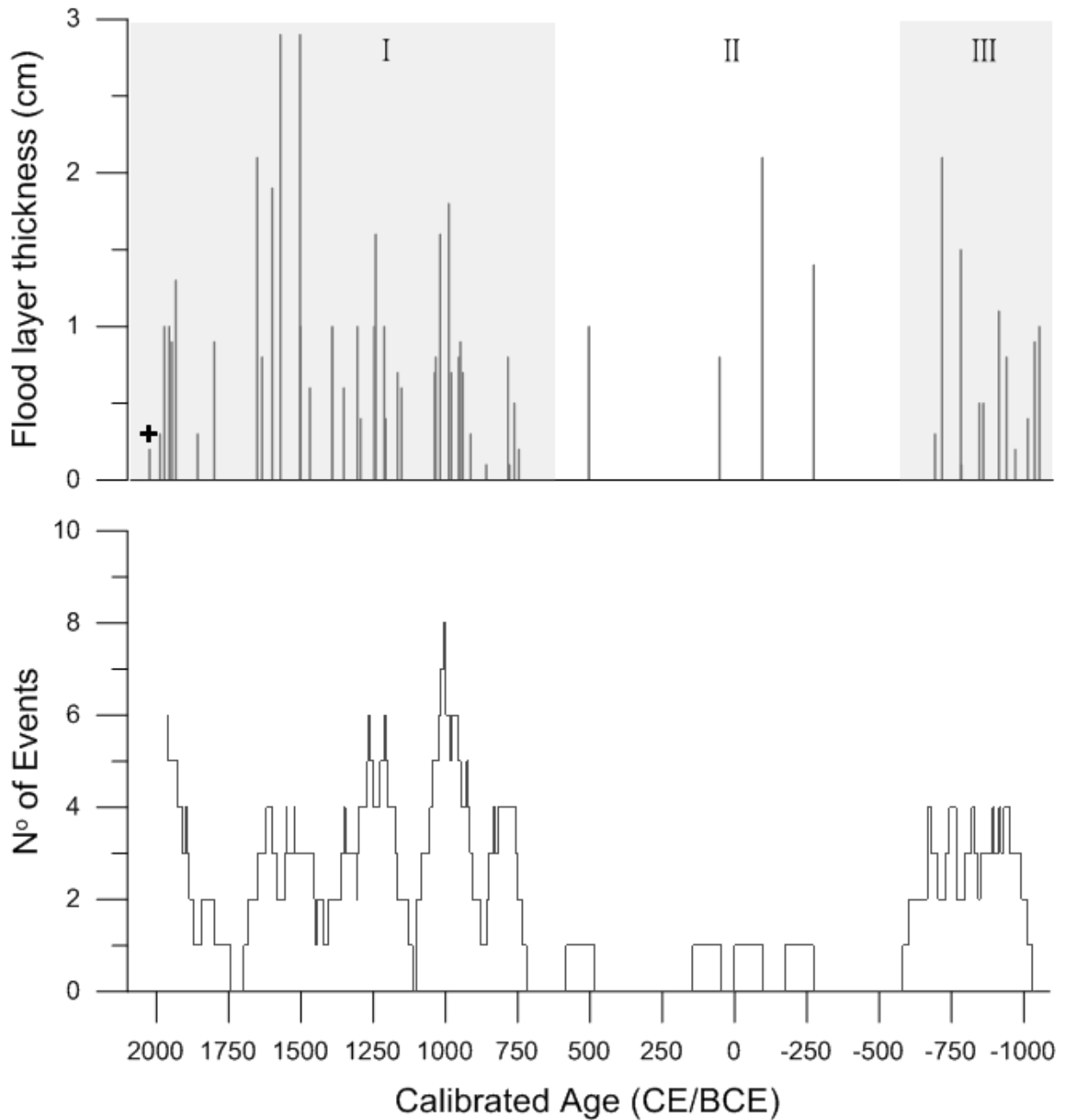


Fig. 5-11 Flood layer thickness (top) and flood frequency reconstruction (bottom) based on L. Llaviucu master core, XRF data and the unsupervised classification of spectral data. The frequency is based on the age-depth model from the combined radiocarbon and ^{210}Pb dating using a moving window of 100 years. Black cross in top graph represents the 2013 event.

5.3 Tephra Analysis

5.3.1 Tephra layer identification

Tephra layer identification was attempted using scanning methods (MSCL and ITRAX) as well as microscopic determination (binocular light microscope and SEM). In a first approach, MSCL parameters including gamma density and magnetic susceptibility (MS) (**Fig. 5-13**) were investigated for the 2014 cores. Typically, the MSCL profiles only showed the thicker tephra layers which are also visible with the naked eye and not the thinner more uncertain layers. In a second step XRF Sr profiles were investigated (**Fig. 5-13**) as this element was found to be the most diagnostic for tephra although this was not always the case. From this information micro-slides were screened for glass shards. These glass particles are clear to green in colour and have sharp to rounded features (**Fig. 5-14A, B and C**). The small size of the particles often made the identification difficult. The more rounded particles were assigned to being either pumiceous material or weathered tephra shards. The samples which passed this test were mounted on Scanning Electron Microscope holders for further identification.

A compilation of all the recovered tephra layers was created from the information gathered by the different techniques. The core overview contains the identified layers (**Fig. 5-15**). A compilation of the tephra layers can be found in **Table 5-3** which also includes an approximation of the percentage volume below 41 μm as well as a written description of the colour before the material was ground up for total digestion. On average, the layers contained over 70 % of particles < 41 μm in size. Thickness varied from 0.2 to 1.4 cm. The tephra colour was in general light to dark grey. The core overview contains both the tephras which were extracted and measured with ICP-MS but also those layers which were not investigated further but which may still be tephra. On the other hand, **Table 5-3** contains only those layers which were investigated further.

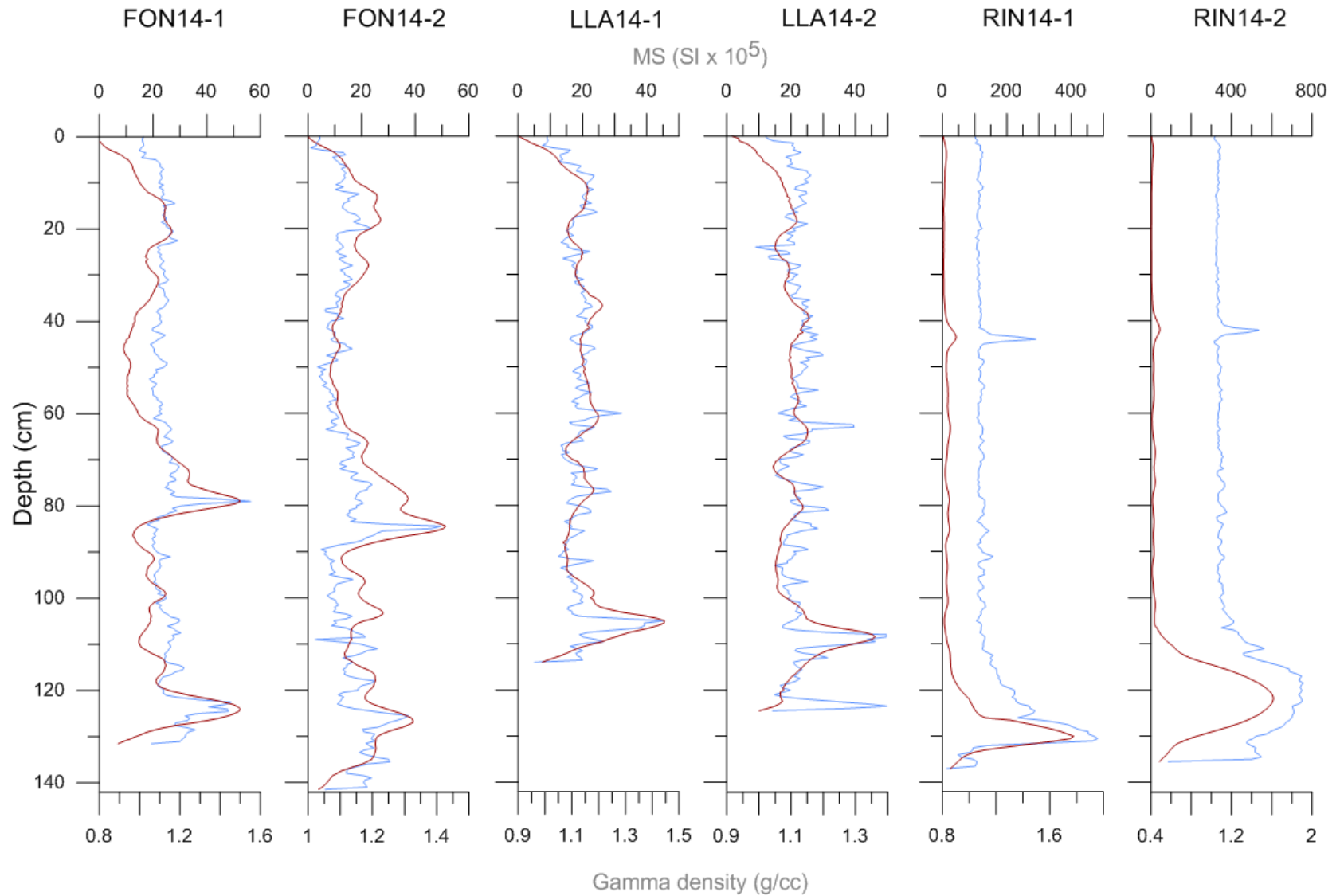


Fig. 5-12 Profiles of magnetic susceptibility (MS, red) and gamma density (blue) as measured with the MSCL for the 2014 cores from L. Llaviucu, Fondococha and Riñoncocha. Values on the x-axis are not on the same scale.

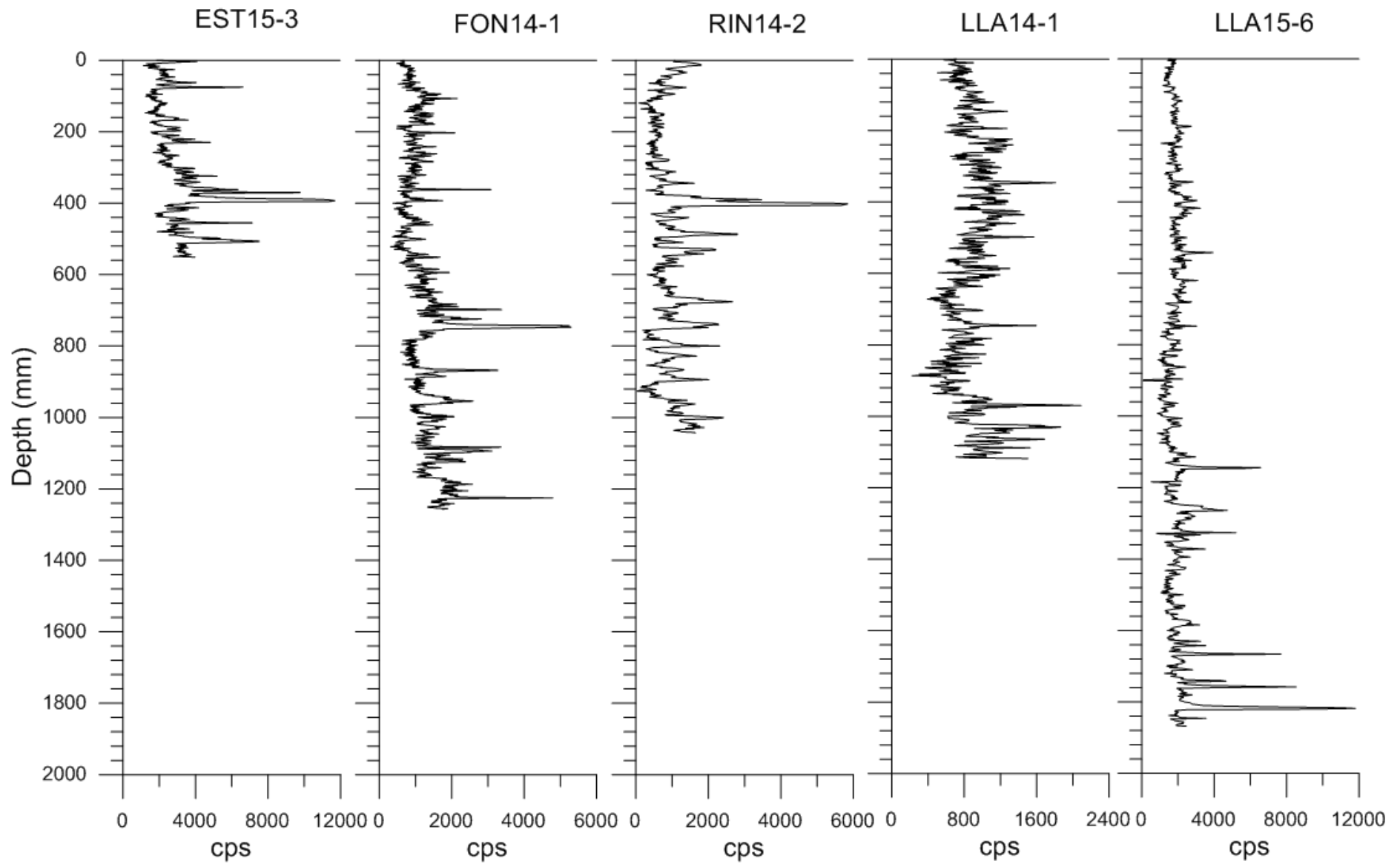


Fig. 5-13 Profiles of Sr counts per second (cps) as measured from the XRF scanner for the 2014 and 2015 cores from L. Llaviucu, Fondococha, Riñoncocha and Estrellascocha. The values on the x-axis are not on the same scale.

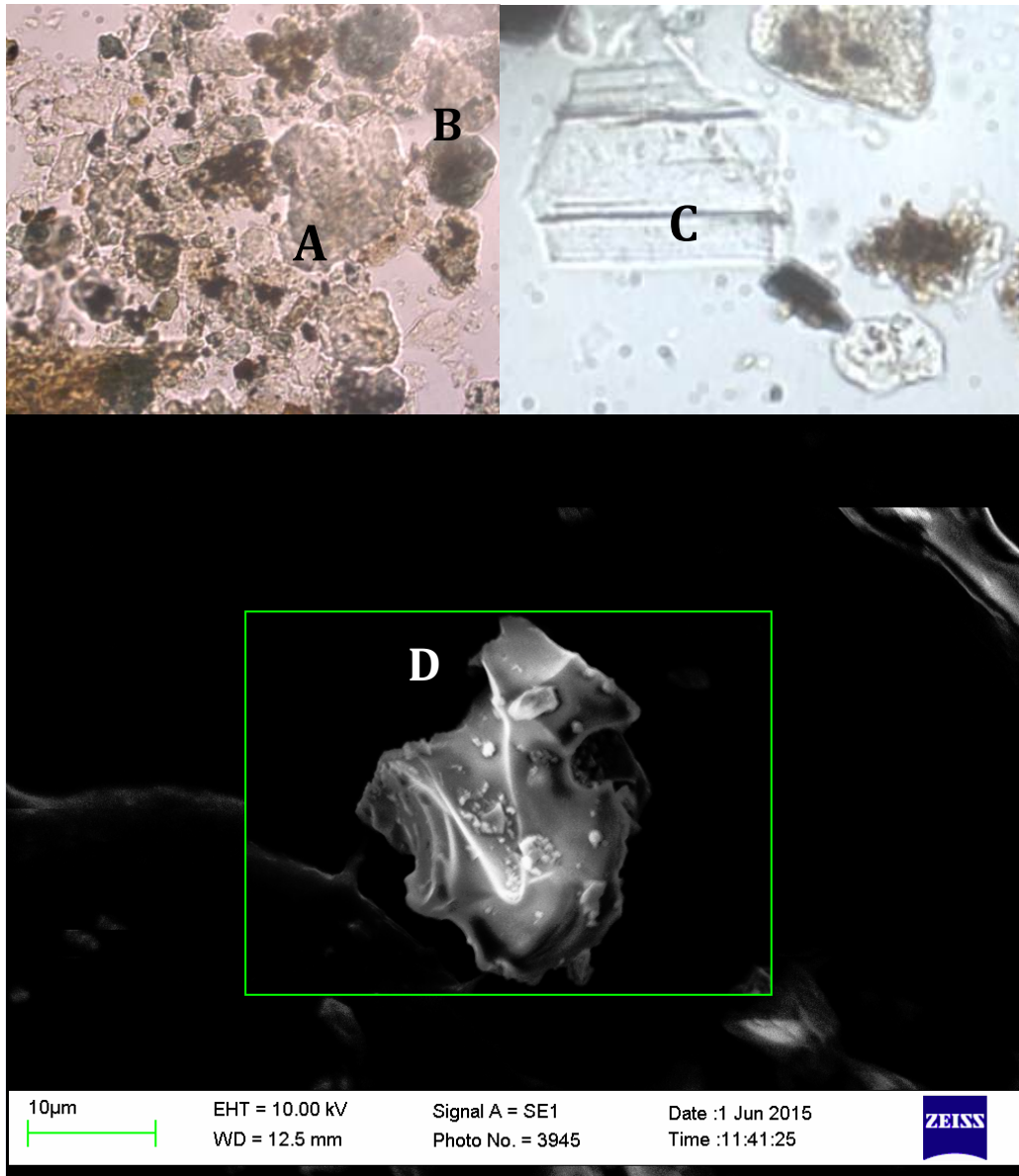


Fig. 5-14 Examples of light (A-C) and scanning microscope (D; FON14-2A) investigation. Tephra shards are clear (C; FON14-1A) and sharp (C; FON14-1A). Weathered tephra or pumiceous material is also shown (A-B; LLA14-2A).

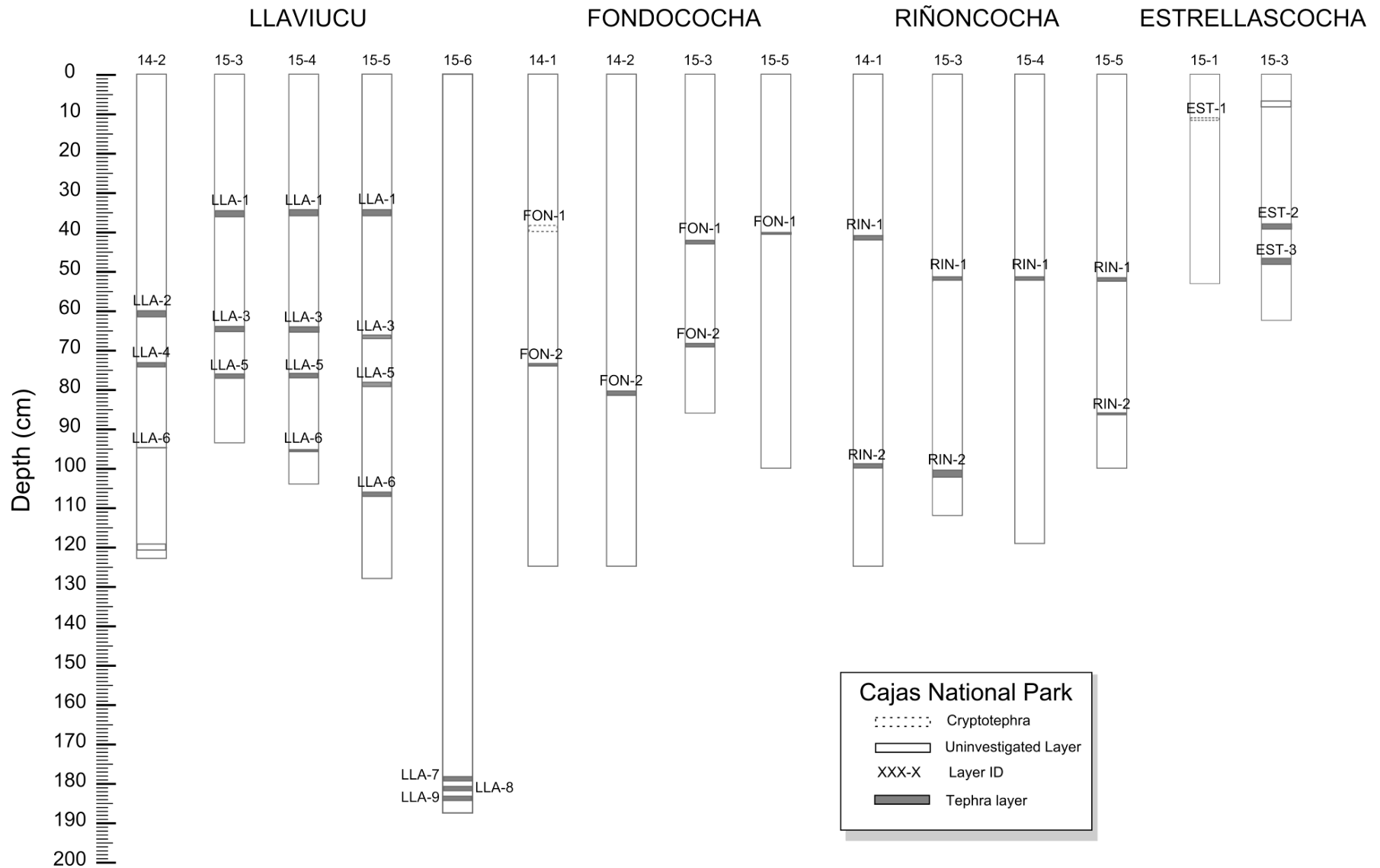


Fig. 5-15 Cores overview containing the tephra layers which were extracted and measured with ICP-MS and layers which were not investigated further but which may still be tephra.

Table 5-3 Compilation of the tephra layers as well as their percentage volume < 41 µm and colour. The depth to the bottom of the layer and its thickness are also indicated.

Sediment core ID	Sample name	Tephra ID	Composite depth (cm)	Thickness (cm)	Volume <41µm (%)	General colour
LLA15-3	LLA15-3 A	LLA-1	35-36	1	65	Light to medium
	LLA15-3 B	LLA-3	64-65	1	75	Medium to dark grey
	LLA15-3 C	LLA-5	77-78	1	80	Light to dark grey
LLA15-4	LLA15-4 A	LLA-1	34-35	1	65	Light to medium
	LLA15-4 B	LLA-3	64-65	1	75	Medium to dark grey
	LLA15-4 C	LLA-5	75-76	1	80	Light to dark grey
	LLA15-4 D	LLA-6	95-95.5	0.5	65	Light to dark grey
LLA15-5	LLA15-5 A	LLA-1	35-36	1	65	Light to medium
	LLA15-5 B	LLA-3	66-67	1	75	Medium to dark grey
	LLA15-5 C	LLA-5	78-79	1	80	Light to dark grey
	LLA15-5 D	LLA-6	106-107	1	65	Light to dark grey
LLA15-6	LLA15-6 A	LLA-7	178.9-179.75	0.85	75	Medium grey
	LLA15-6 B	LLA-8	180.9-182.1	1.2	80	Medium to dark grey
	LLA15-6 C	LLA-9	183.7-184.5	0.8	65	Medium to dark grey
LLA14-2	LLA14-2 A	LLA-2	60-60.8	0.8	80	Light to brow grey
	LLA14-2 B	LLA-4	73.7-74.1	0.4	75	Medium grey
	LLA14-2 C	LLA-6	94.8-94.4	0.4	90	Light grey
RIN15-3	RIN15-3 A	RIN-1	51-52	1	75	Light to dark grey
	RIN15-3 B	RIN-2	100-102	2	50	Medium to dark grey
RIN15-4	RIN15-4 A	RIN-1	51-52	1	75	Light to dark grey
RIN15-5	RIN15-5 A	RIN-1	51-52	1	75	Light to dark grey
	RIN15-5 B	RIN-2	86.5-86.7	0.2	50	Medium to dark grey
RIN14-1	RIN14-1 A	RIN-1	41.5-42.7	1.2	60	Light to dark grey
	RIN14-1 B	RIN-2	99.6-100.1	0.5	30	Medium to dark grey
FON15-3	FON15-3 A	FON-1	42.5-42.7	0.2	90	Light to dark grey
	FON15-3 B	FON-2	68-69	1	80	Light to dark grey
FON15-5	FON15-5 A	FON-1	40-40.2	0.2	90	Light to dark grey
FON14-1	FON14-1 A	FON-1	38-40	2	80	Medium grey
	FON14-1 B	FON-2	73.8-74.8	1		
FON14-2	FON14-2 A	FON-2	80.3-81.3	1	75	Light to medium
EST15-1	EST15-1 A	EST-1	11.5-11.9	0.4	70	Dark grey
EST15-3	EST15-3 A	EST-3	38.5-39.9	1.4	75	Medium to dark grey
	EST15-3 B	EST-4	47.6-48.6	1	95	Light grey

5.3.2 Physical characteristics of tephra and their classification

Tephra morphological type

Each tephra layer was analysed under the SEM for the percentage of lithics, glass and pumiceous fragments (**Fig. 5-17, Plate III** and **Plate IV**) by using twenty images as

tested (**Fig. 5-16**). Using twenty images was found to overestimate the mean slightly but a two-tailed Student's t-test showed that the means were not significantly different ($p > 0.05$). As seen from **Fig. 5-17**, most layers consisted of all three types (pumice, lithics, glass) to varying degrees, but some such as RIN15-3/4/5-A, RIN14-1-A, EST15-3-B and FON14-1-B were 100% glassy. Pumice was a minor component of some of the samples, not reaching 50% of the compositions. On the other hand, lithics were prominent in many samples, at times reaching 90% of the composition.

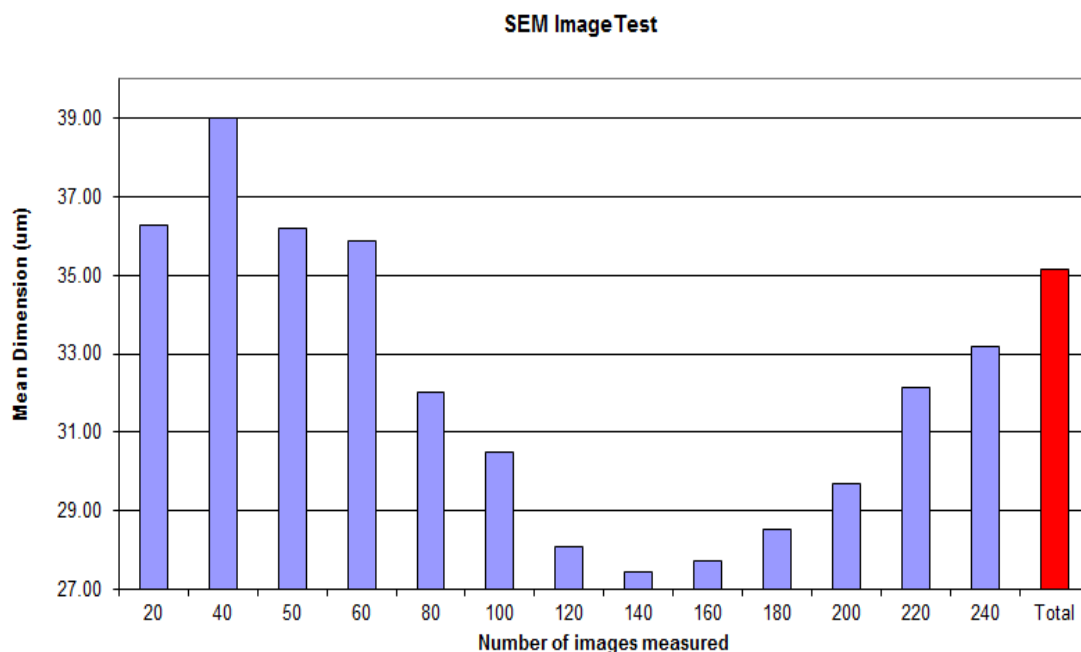


Fig. 5-16 Results of the test used to determine the most appropriate number of images. Two hundred forty images were taken and the mean dimension of particles after 20, 40, 50, 60, 80, 100, 120, 140, 160, 180, 200, 220 and 240 pictures was calculated.

Each tephra layer was also analysed for the degree of vesicularity and crystallinity (**Fig. 5-18, Plate III, Plate IV**) according to the classification scheme described in section 4.9.4. Half of the samples (12 out of 23) contained over 50 % dense fragments. Moderate and vesicular fragments were abundant in several samples such as RIN15-3/4/5-A, RIN14-1-B, RIN14-1-A, FON14-1-A, FON14-2-A, FON15-3-B and FON14-1-B. Few samples contained bubble shards. The fragments were predominantly crystal poor as the samples contained an average of 94% crystal poor fragments. Samples with higher counts of microlite rich fragments were LLA15-6-B, EST15-3-A, FON15-3-B and RIN15-3/5-B. No sample contained fragments which were crystal rich.

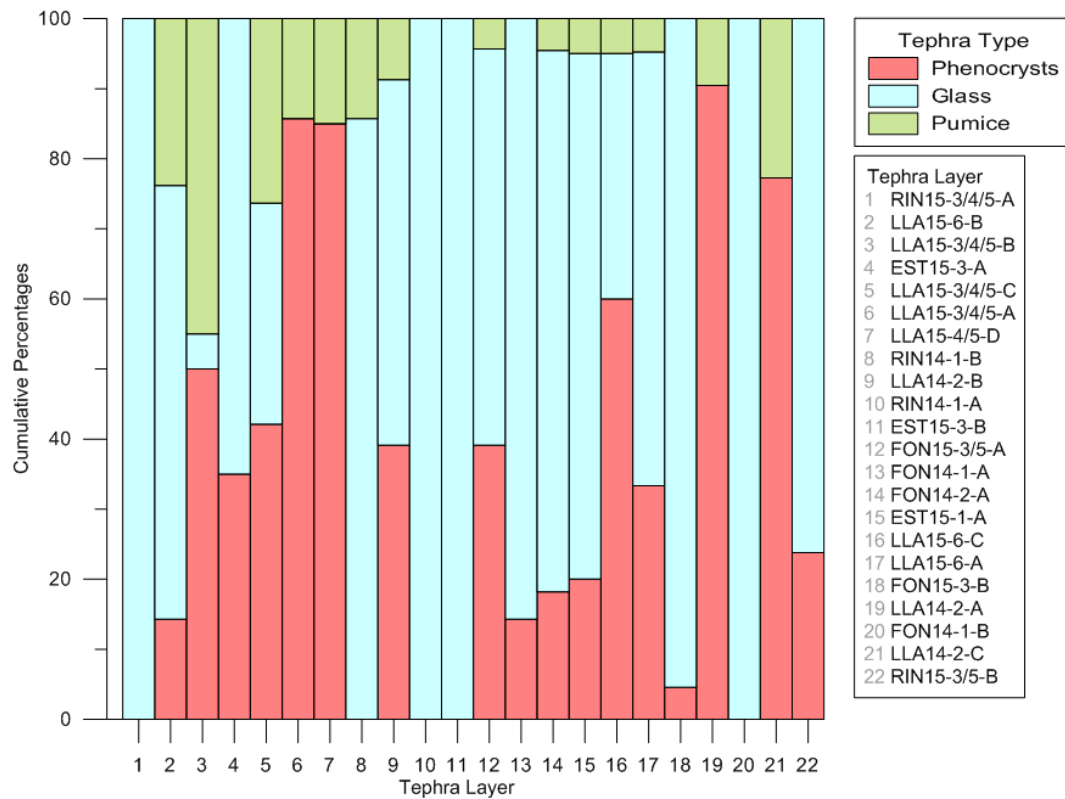


Fig. 5-17 Results of the analysis of tephra morphological type using SEM imagery and Scandium software.

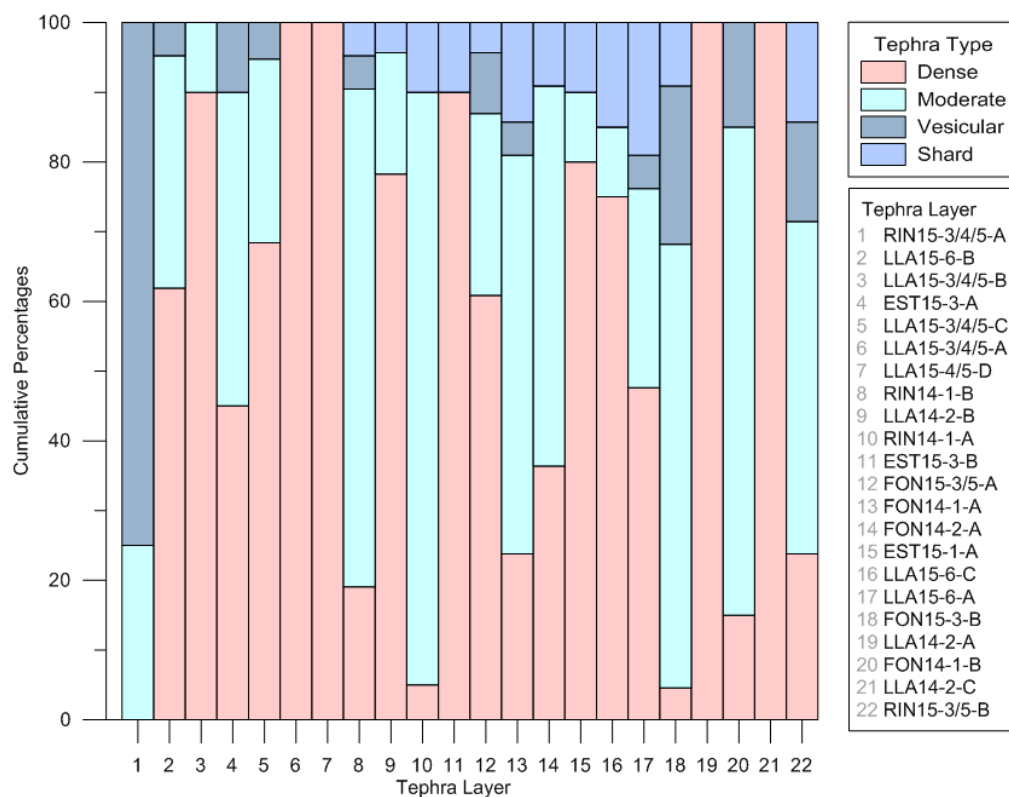


Fig. 5-18 Results of the particle surface analysis using SEM imagery and Scandium software.

Tephra morphological size

Tephra length and breadth were measured and showed a wide range of sizes (**Table A5-1**). The average length and breadth were 78.28 and 54.18 μm with a standard deviation of 58.5 and 43.6 μm respectively. The minimum length and breadth reached were 3.05 and 2.10 μm . Maximum length and breadth attained were 433.28 and 336.27 μm respectively. Only 6 out of 23 samples had average lengths greater than 100 μm . Layers LLA15-3/4/5-A and LLA15-4/5-D had the largest particles while EST15-3-B had the smallest.

Tephra classification based on morphological features

Tephra classification was attempted through statistical means. Unconstrained clustering analysis using average (UPGMA), complete and single linkages as well as Ward's method were employed to group the tephra layers based on their morphological features. The morphological features included were maximum, minimum and average length and breadth, the occurrence of lithics, glass or pumice fragments as well as the occurrence of fragments in terms of vesicularity and crystallinity. The number of clusters created varied from 4 to 12. Based on stratigraphy, a minimum of 7 tephra groups must exist. This prior knowledge was applied to the cluster analyses to discard dendrograms with fewer groups. **Table 5-4** shows the working group results for all methods. Unusable methods included the PAST software (Hammer et al., 2001), complete and single linkage methods (R hclust and pvclust functions; Suzuki and Shimodaira 2006) as they both yielded fewer than 7 groups. In general the single linkage method performed more poorly than the other methods, creating very large groups and many single sample groups which are not expected to be the case. Some layers such as RIN15-3/4/5-A were always found to be alone. Other layers such as LLA15-6-B, EST15-3-B, EST15-1-A, RIN14-1-A, FON15-3-B, FON14-1-B and RIN15-3/5-B were uncertain and often switched groups.

In a further step, cluster plots using k-means clustering with k clusters was attempted on the morphological dataset. The k clusters were determined from the dendrogram analysis in the previous step. K values of 7, 8, 9 and 12 were tested. **Table 5-5** displays the working results of the cluster plot analysis. Certain groups remained the same in all k-clusters and would be described as higher certainty groups. The total number of clusters was ambiguous but may be 9.

Table 5-4 Tephra groups according to morphological features. Analysis based on four clustering methods (Ward's method, single, average and complete linkages) in three different ways (PAST software, R hclust and pvclust functions; (Hammer et al., 2001; Suzuki and Shimodaira, 2006).

Morphology dataset			
High certainty groups	Comments	Uncertain layers	Comments
LLA15-3/4/5-B LLA15-3/4/5-C	Always together except in single method	LLA15-6-B EST15-3-B	Mostly together
LLA15-3/4/5-A LLA15-4/5-D	Always together	EST15-1-A	Often with EST15-3-C, LLA15-6-C, LLA15-6-A or with LLA14-2-B, FON15-3/5-A, RIN14-1-B, FON15-3-B, RIN15-3/5-B, RIN14-1-A, FON14-1-B
EST15-3-C LLA15-6-C LLA15-6-A	Always together	RIN14-1-A FON15-3-B FON14-1-B RIN15-3/5-B	Often with RIN14-1-B, EST15-3-A, EST15-1-A, LLA14-2-B, FON15-3/5-A
LLA14-2-B FON15-3/5-A	Always together		
LLA14-2-A LLA14-2-C	Always together except in single method		
RIN15-3/4/5-A	Always alone		
RIN14-1-A FON15-3-B FON14-1-B RIN15-3/5-B	Always together but split in the Ward probability method		
RIN14-1-B FON14-1-A FON14-2-A	Mostly together but once RIN14-1-B separate from FON14-1-A, FON14-2-A in the complete method		

Table 5-5 Results of the unconstrained k-means analysis of the morphological dataset using four clustering methods (Ward's method, single, average and complete linkages) in three different ways (PAST software, R hclust and pvclust functions; Hammer, Harper, and Ryan 2001; Suzuki and Shimodaira 2006).

Morphology dataset			
High certainty groups	Comments	Uncertain groups	Comments
LLA14-2-A LLA14-2-C		RIN14-1-A	With RIN14-1-B, FON15-3-B, FON14-1-B, LLA14-2-A or just FON15-3-B and LLA14-2-A or with FON14-1-A and FON14-2-A
RIN15-3/4/5-A		RIN14-1-B FON14-1-B	Alone or with FON15-3-B and LLA14-2-A
LLA15-3/4/5-B LLA15-3/4/5-C LLA15-3/4/5-A LLA15-4/5-D	Separate when k=12	FON15-3-B LLA14-2-A	Alone or with RIN14-1-B and FON14-1-B
LLA15-6-B EST15-3-B	Separate when k=12	EST15-3-B LLA15-6-C LLA15-6-A	Alone or with LLA14-2-B, FON15-3/5-A, EST15-1-A and/or FON14-1-A, FON14-2-A
EST15-3-B LLA15-6-C LLA15-6-A			
LLA14-2-B FON15-3/5-A EST15-1-A			
RIN14-1-B FON14-1-B			
FON15-3-B LLA14-2-A			
FON14-1-A FON14-2-A			

Biplots were also used to classify the tephra layers but were found to yield ambiguous results. However, it becomes apparent that many of the L. Llaviucu layers are different from the others as the particle sizes are much larger.

Tephra Munsell colour

The colour of tephra layers was identified using the Munsell colour chart (Fig. 5-19). Only twelve types of colours were found varying from greyish white to yellowish grey. The most prominent colours were greyish white (N8; 34.8%) followed by grey white (N7; 13%) and light grey (2.5Y 7/1; 8.7%). Two layers had a yellow hue (5Y 8/2 and 5Y 7/3).

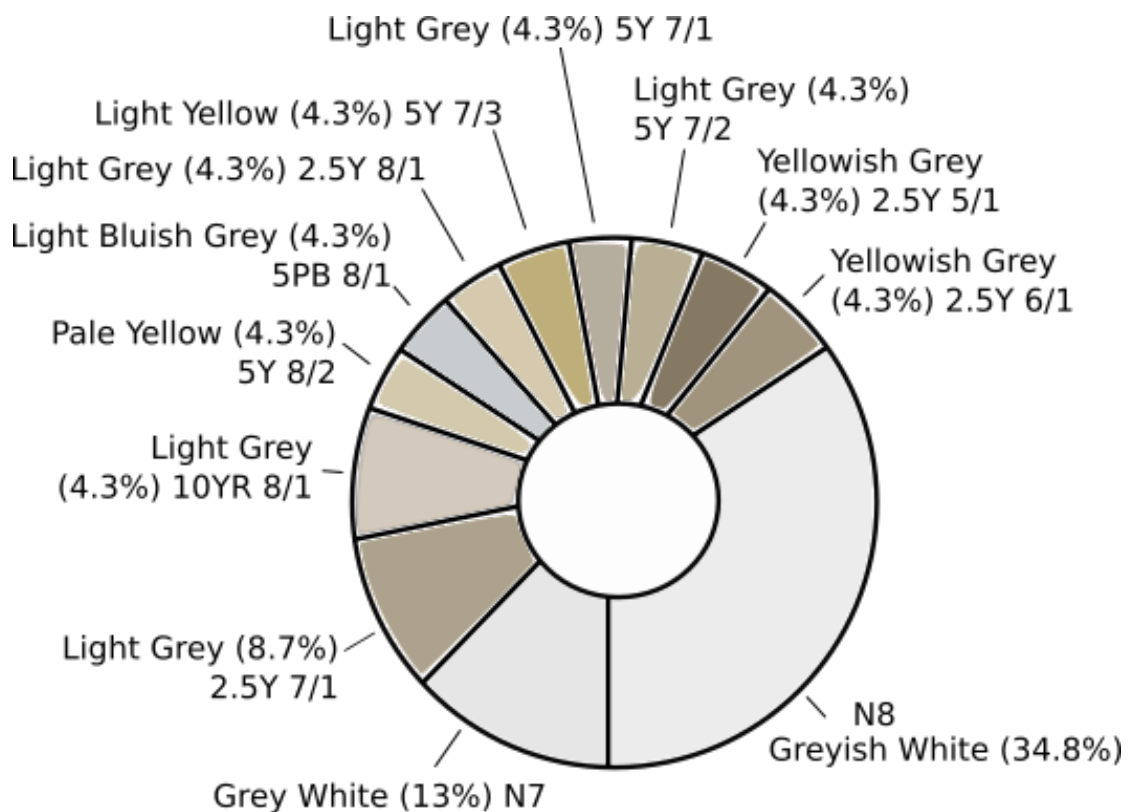


Fig. 5-19 Colour wheel of tephra samples based on the Munsell colour classification. Colours are approximations of the original Munsell colour. Percentages denote the proportion of layers which had that colour.

Tephra classification based on colour

Tephra layers were grouped based on their Munsell colours. Twelve groups were identified (Table 5-6).

Table 5-6 Tephra groups according to their Munsell colour.

Colour Dataset			
Group	Layers	Munsell Code	Munsell Colour
1	RIN14-1-A	N8	Greyish white
	EST15-3-A	N8	Greyish white
	RIN15-3/4/5-A	N8	Greyish white
	FON14-2-A	N8	Greyish white
	LLA15-6-B	N8	Greyish white
	FON15-3-B	N8	Greyish white
	FON14-1 B	N8	Greyish white
2	EST15-1-A	N7	Greyish white
	RIN15-3/5-B	N7	Greyish white
	RIN14-1-B	N7	Greyish white
3	LLA15-6-A	2.5Y 7/1	Light grey
	LLA15-4/5-D	2.5Y 7/1	Light grey
4	FON15-3/5-A	10YR 8/1	Light grey
	FON14-1-A	10YR 8/1	Light grey
5	LLA14-2-B	5Y 8/2	Pale yellow
6	EST15-3-B	5PB 8/1	Light bluish grey
7	LLA14-2-C	5Y 8/1	Light grey
8	LLA14-2-A	5Y 7/3	Light yellow
9	LLA15-6-C	5Y 7/1	Light grey
10	LLA15-3/4/5-B	5Y 7/2	Light grey
11	LLA15-3/4/5-C	2.5Y 5/1	Yellowish grey
12	LLA15-3/4/5-A	2.5Y 6/1	Yellowish grey

5.3.3 Qualitative tephra elemental composition

Qualitative data from the XRF measurements were used to determine the main geochemical component of each tephra layer. Elemental ratios of Ti/Ca, K/Sr, Mn/Ca, Ca/Ni and Zn/Ca were then calculated based on the most deterministic element peaks (**Fig. 5-20**). Three tephra types can be identified. The first layer has high Mn values, the second with high K, Mn and Ti and lastly with high Ca values. Layers in L. Llaviucu were the most ambiguous to identify.

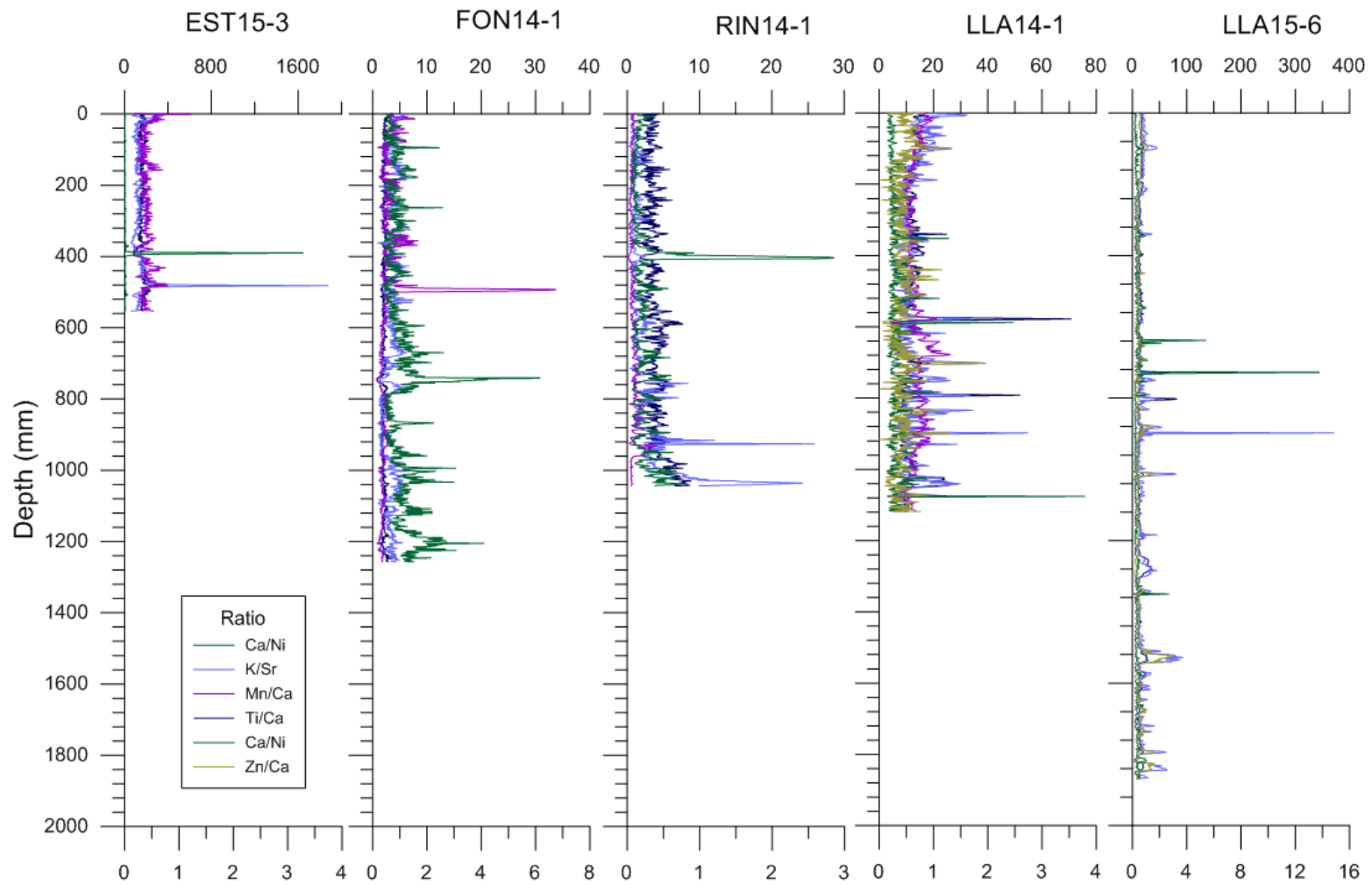


Fig. 5-20 Elemental ratios of Ti/Ca (dark blue), K/Sr (light blue), Mn/Ca (purple), Ca/Ni (light green) and Zn/Ca (orange) for Estrellascocha, Fondocochoa, Riñoncocha and Llaviucu 2014 and 2015 cores.

5.3.4 Quantitative tephra geochemistry

Result accuracy of geochemical fingerprinting

Aliquots of each tephra layers were chemically fingerprinted for a range of major and minor elements using the ICP-MS after total digestion. The accuracy of the method was assessed through the recovery rates of the laboratory reference material compared to the certified elemental concentration values of the CRM. Recovery rates ranged widely depending on the element and the batch. In general batch 1 generated systematically slightly elevated values (125.61 %) compared to the CRM. The concentrations of batch 1 were adjusted so the recovery for each element would match the average of the other batches. Batch 5 significantly underestimated values (86.69 %). The samples in batch 5 were digested and measured a second time in batch 6 and measured a third time as batch 7. The second digestion showed improved recovery rates for some elements and the third measurement was better still. Therefore a compilation of well recovered elements from batch 5/6/7 was produced and will be referred to as batch 5mix onwards. Batches 2 to 4 yielded the most accurate values (106.79, 102.95 and 98.99 % respectively) on average. The recovery rate for major elements was in general better than for the minor elements. However, ^{43}Ca and ^{44}Ca were particularly underestimated (21.19 and 32.07 % respectively) on average by all batches. Some elements particularly the rare earth elements such as ^{139}La , ^{141}Pr , ^{146}Nd , ^{147}Sm , ^{153}Eu , ^{157}Gd , ^{165}Ho , ^{169}Tm , ^{172}Yb and ^{175}Lu yielded low values (70.11% on average) in batch5mix even after the second digestion's second measurement.

Data visualisation through elemental line plots

Line plots were produced for a subset of the A1 dataset containing all rare earth elements (REE) (**Fig. 5-21**). The lines indicate the signature of each tephra layer based on the REE. The samples were ordered based on the shape of the lines. The REE line plot reveals that possibly four types of tephra are present as four patterns are visible. The first pattern (blue line) is composed of most of the tephra layers (LLA15-3/4/5-B, LLA15-3/4/5-C, LLA15-3/4/5-A, EST15-3-A, FON15-3/5-A, LLA15-4/5-D, LLA15-6-C, FON14-1-A, FON14-2-A, LLA14-2-B, RIN14-1-B, RIN15-3/4/5-A, and RIN14-1-A), the second pattern (red line) consists of a few with a wider range (RIN15-3/5-B, FON15-3-B and FON14-1-B) while the third (green line) contains even fewer (LLA14-2-A, LLA15-6-A and LLA14-2-C). Layer EST15-1-A (purple), although similar to the others in the second (red) group in terms of the line pattern, shows concentration values which are higher for all elements.

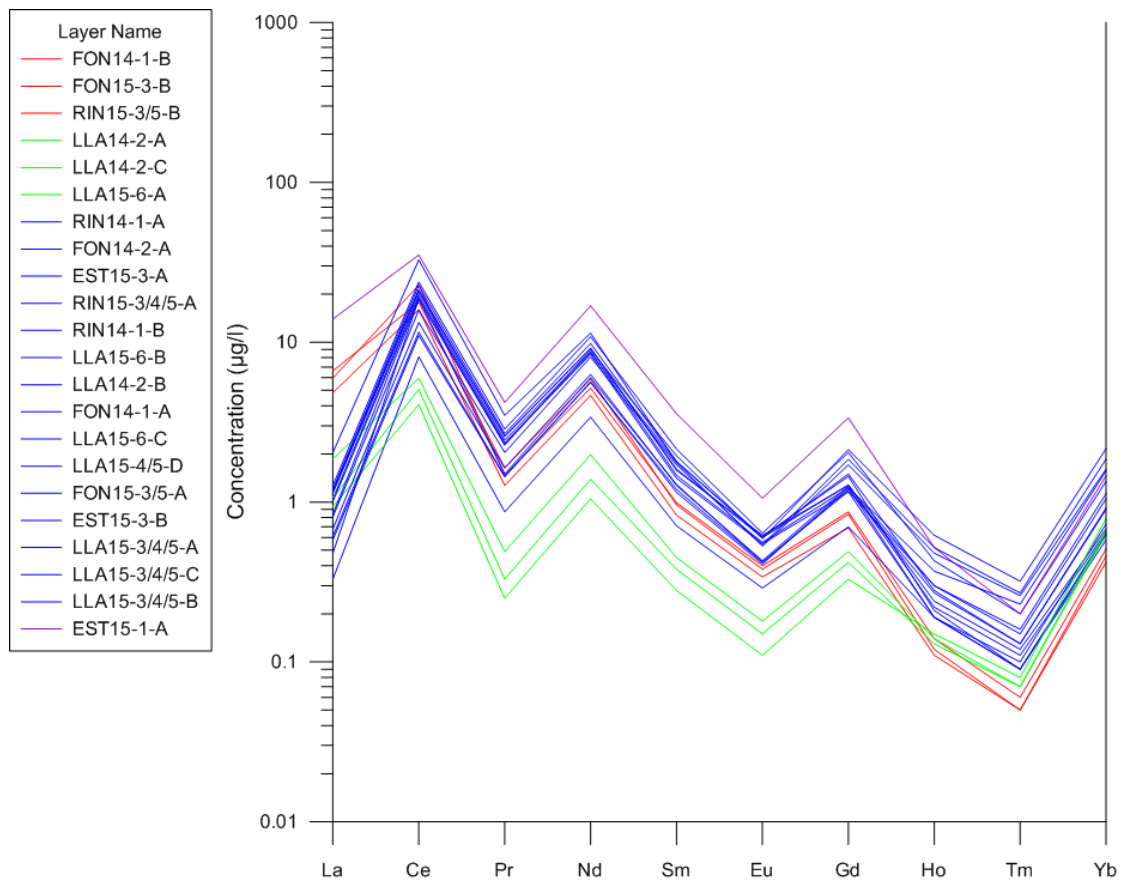


Fig. 5-21 Line plot of the REE in the A1 dataset. The layers are grouped based on the shape of the line. The y-axis has a log scale.

5.3.5 Statistical analysis of the geochemical datasets and tephra classification

Statistical methods were employed to correlate the tephra layers and the results are described in the following section.

Tephra classification based on Principal Component Analysis (PCA)

The geochemical datasets (A1 and B2) were investigated using PCA. Two and four PCs were found to explain 70.8 and 86.6 % of the total variance in the A1 and B2 datasets respectively (**Table 5-7**). Once this was identified, the two and four PC loadings for the A1 and B2 datasets respectively were plotted as heat maps. The PCA reduced the number of elemental biplots to investigate from 105 to 4 for the A1 dataset and from 351 to 24 for the B2 dataset.

Table 5-7 Number of significant principal components (PC) for each dataset as identified from the broken stick method and scree plots. The percentages of variance explained as well as the total variance are also given.

Dataset	Number of significant PC (Broken stick)	% Variance explained				Total % Variance
		PC1	PC2	PC3	PC4	
A1	2	45.82	24.98			70.8
B2	4	37.5	30.2	10.4 9	8.41	86.6

Elemental biplots resulting from PCA

All biplots with the pairs identified through PCA can be found in section 0. Tephra layers tend to plot with different layers when plotted with each different pair of elements. Some layers such as EST15-1-A are always outside of the cloud. Other layers, such as RIN14-1-A, EST15-3-A, RIN15-3/4/5-A always plot together in the major elements. According to Pearce et al. (2008), an overlapping composition in all biplots is a very strong indication of correlation. However, any clear separation rules out the possibility of a correlation. Triplicates of the same layer often plot in straight lines which are to be expected if the ratio remains the same. Replicates of each layer would be assessed to judge the spread of the element composition variation which in all cases appears to be wide. Strikingly, L. Llaviucu layers always plot apart from the other layers.

REE ratios of incompatible elements were also plotted (Nd/La-Ce/La, Eu/La-Pr/La, Ho/Yb-Tm/Yb) as seen in section 0. According to Pearce et al. (2008), ratio would help differentiate layers with similar compositions. From both Nd/La-Ce/La and Eu/La-Pr/La plots the layers mentioned above show overlaps. However, Ho/Yb-Tm/Yb plot shows much scattering even for triplicate samples. This would further indicate heterogeneity and makes the correlation more challenging.

Tephra classification based on similarity coefficient (SC) analysis

Similarity coefficient (SC) designed by Borchartd et al. (1972) with all weights set to 1 was performed on both the A1 dataset and B2 datasets. The values represent the likelihood of a tephra layer being similar to each other. The evaluation of the SC analysis showed that in general triplicate samples from the same tephra layer were very highly similar to each other. In some cases (LLA15-3/4/5-B, RIN15-3/4/5-A and RIN14-1-A) the triplicate samples were only highly similar to one another. Each layer was at least highly similar to one other layer except for EST15-3-B, EST15-1-A and LLA14-2-A which showed no similarity to any other layer. Making sense of the results was done through a spider diagram where correlating samples are linked. The working results can be found in **Table 5-8**.

The same analysis was attempted for the B2 dataset. Similar to the previous dataset, in some cases (LLA15-3/4/5-B, RIN15-3/4/5-A and RIN14-1-A) the triplicate

samples were only highly similar to one another. As opposed to the previous dataset, in no case were the triplicates less than highly similar to one another. Once again the evaluation of the SC analysis showed all layers were highly similar to at least one other layer except for LLA14-2-B, EST15-3-B, FON15-3/5-A, FON14-1-A, LLA14-2-A, EST15-1-A, RIN15-3/5-B and RIN14-1-B. The number of uncorrelated samples is higher in the B2 dataset than the A1 dataset. A comparison of the two datasets showed that using all elements rather than just the well recovered ones makes a difference. In the first instance, fewer pairs were very highly similar when incorporating all elements than found in the A1 dataset. Similarly to the above, a spider diagram was also used here. The synthesis showed that at least 9 groups are possible although many are uncertain.

Table 5-8 Synthesis of the results of the SC analysis of the A1 and B2 datasets after using the spider diagram for support.

Very high correlation groups/pairs (>0.9)	High correlation groups/pairs (>0.8)	Uncertain
EST15-1-A	RIN15-3/4/5-A FON14-2-A	LLA15-3/4/5-C LLA15-3/4/5-A
EST15-3-C	RIN15-3/4/5-A LLA15-3/4/5-B	RIN14-1-A and EST15-3-A with LLA15-6-C
LLA14-2-A	LLA14-2-C LLA15-6-A	RIN14-1-A FON14-1-B
RIN14-1-A EST15-3-A RIN15-3/4/5-A LLA15-6-B FON15-3-B	LLA14-2-B LLA15-6-C LLA15-4/5-D	RIN15-3/5-B RIN14-1-B
	FON15-3-B FON14-1-B	FON14-1-B EST15-3-B
	LLA15-3/4/5-B LLA15-3/4/5-C	LLA15-6-C with RIN14-1-A, EST15-3-A, RIN15-3/4/5-A, LLA15-6-B and FON15-3-B
		FON14-2-A with RIN14-1-A, EST15-3-A, RIN15-3/4/5-A, LLA15-6-B and FON15-3-B
		FON15-3/5-A and FON14-1-A with LLA15-3/4/5-A

Further analysis through unconstrained clustering analysis using UPGMA, complete and single linkages and Ward's method were employed to group the tephra layers based on their SC scores for the A1 and B2 datasets. The dendrogram analysis showed that 7 to 16 clusters were possible. The working results are found in **Table 5-9**. The unusable dendrogram methods (Ward's method using R hclust, complete linkage using the PAST

software, single linkage using R pvclust for the B2 dataset and Ward's method using R hclust for the A1 dataset) did not remain constant in both the A1 and B2 datasets. Although more tephra layers remain clustered by themselves using the B2 dataset than the A1 dataset, using both datasets allows for better cluster identification for problematic layers. Tephra layers LLA14-2-B, FON15-3/5-A and RIN14-1-B remained problematic but were assigned to a certain cluster although these are found either alone or switching between different groups. Some layers are rarely found in any cluster such as EST15-1-A and LLA14-2-A. Other layers are unambiguously assigned to the same cluster in both datasets using the SC values.

Table 5-9 Synthesis of the dendrogram clustering results of the SC values A1 and B2 datasets.

High certainty groups	Low certainty groups	Comments
EST15-3-B FON15-3/5-A FON14-1-A	RIN15-3/5-B	Can be with EST15-1-A or LLA14-2-C and LLA15-6-A
RIN14-1-A RIN15-3/4/5-A FON14-2-A LLA15-6-B	EST15-1-A	Can be with LLA14-2-A or LLA14-2-C and LLA15-6-A or alone
LLA14-2-C LLA15-6-A	LLA14-2-B	Can be with LLA14-2-C, LLA15-6-A and LLA15-6-C or LLA15-4/5-D or alone
FON15-3-B FON14-1-B	LLA15-3/4/5-A	Can be with EST15-3-C, FON15-3/5-A and FON14-1-A or LLA15-3/4/5-B and LLA15-3/4/5-C
LLA15-3/4/5-B LLA15-3/4/5-C	EST15-3-B	Can be with RIN14-1-A, EST15-3-A and RIN15-3/4/5-A or alone or with FON15-3-B and FON14-1-B
LLA15-6-C LLA15-4/5-D		

Tephra classification based on cluster analysis

Cluster analysis was used to determine the number of possible tephra horizons as well correlating between samples. The number of clusters created varied from 2 to 16 depending on the method. As established in the methods section, according to the stratigraphy, a minimum of 6 tephra groups must exist. The working results are found in **Table 5-10**. The dendrogram methods (Ward's method using R hclust, complete linkage

using the PAST software, single linkage using R pvclust and average linkage using pvclust) remain constant in both the A1 and B2 datasets. Although more tephra layers remain clustered by themselves using the B2 dataset than the A1 dataset, using both datasets allows for better cluster identification for problematic layers. For example, EST15-3-A could be assigned to the same group as layers RIN14-1-A, RIN15-3/4/5-A, FON14-2-A and LLA15-6-B when both datasets were investigated. Tephra layers EST15-3-B, FON15-3/5-A, FON14-1-A, LLA14-2-A, LLA15-3/4/5-B, LLA15-3/4/5-C, LLA15-3/4/5-A and RIN14-1-B cannot be unambiguously assigned to a certain cluster but these are found either alone or switching between different groups. Some layers are never found in any cluster such as EST15-1-A. Other layers are unambiguously assigned to the same cluster in both datasets.

Table 5-10 Dendrogram clustering result analysis using the A1 and B2 datasets, four clustering methods in three different ways.

High certainty groups	Comments	Uncertain layers	Comments
EST15-1-A	Alone in all methods	LLA15-3/4/5-C	Mostly alone but once seen with LLA14-2-C and LLA15-6-A
RIN14-1-A, RIN15-3/4/5-A, FON14-2-A, LLA15-6-B, EST15-3-A	Together in all methods	EST15-3-C	Alone or in group with EST15-3-B, FON15-3/5-A, FON14-1-A, LLA15-3/4/5-A or RIN14-1-B
LLA14-2-C, LLA15-6-A	Together in all methods	FON15-3/5-A	Alone or in group with EST15-3-B, FON15-3/5-A, FON14-1-A, LLA15-3/4/5-A or RIN14-1-B
FON15-3-B, FON14-1-B	Together in all methods	FON14-1-A	Alone or in groups with EST15-3-B, FON15-3/5-A, FON14-1-A, FON15-3-B, 16 and LLA15-3/4/5-A
LLA14-2-B, LLA15-6-C, LLA15-4/5-D	Together in all methods	LLA15-3/4/5-A	Alone or in group with EST15-3-B, FON15-3/5-A, FON14-1-A
		RIN14-1-B	Alone or with EST15-3-B, FON15-3/5-A or RIN15-3/5-B
		RIN15-3/5-B	Alone or with FON14-1-A, FON15-3-B, RIN14-1-B or FON14-1-B
		LLA15-3/4/5-B	Mostly alone, but switches a lot
		LLA14-2-A	Mostly alone, but switches a lot

In a further step, cluster plots using k-means clustering with k clusters was attempted on both the A1 and the B2 datasets. The k clusters were determined from the previous step. K values of 8, 9, 10, 12, 14, 15 and 16 were tried.. **Table 5-11** below displays the results of the cluster plot analysis for each dataset while **Table 5-12** highlights the synthesis results. The A1 and B2 dataset analysis produced different results although certain groups remained the same and would be described as higher certainty groups. In both dataset analyses, the total number of clusters was ambiguous but may be 8 for the

A1 dataset and 7 for the B2 dataset. More high certainty groups were produced using the A1 dataset than the B2 dataset.

Table 5-11 Results of the cluster plot analysis using k-means with k number of clusters determined from the dendrogram analysis. Results for both the A1 and B2 datasets are displayed.

B2 dataset		A1 dataset	
High certainty groups	Uncertain groups	High certainty groups	Uncertain groups
EST15-1-A	FON14-2-A, LLA15-6-B, RIN14-1-A, EST15-3-A, RIN15-3/4/5-A	FON15-3/5-A, LLA15-3/4/5-A	LLA15-6-C, LLA14-2-B and LLA15-4/5-D
LLA14-2-A LLA14-2-C LLA15-6-A	LLA15-3/4/5-C and LLA15-3/4/5-A or LLA15-3/4/5-C and LLA15-3/4/5-B	LLA15-6-A LLA14-2-C	EST15-3-B, FON15-3/5-A, FON14-1-A and LLA15-3/4/5-A
LLA14-2-B LLA15-6-C LLA15-4/5-D	EST15-3-B, FON15-3/5-A, LLA15-3/4/5-A and RIN14-1-B	RIN15-3/5-B, RIN14-1-B	LLA14-2-A, LLA15-3/4/5-B and LLA15-3/4/5-C
RIN14-1-A RIN15-3/4/5-A EST15-3-A	EST15-3-B, FON14-1-A	EST15-1-A	
	FON14-1-A, FON15-3-B, RIN15-3/5-B, FON14-1-B	LLA15-4/5-D LLA14-2-B	
		RIN14-1-A, EST15-3-A, RIN15-3/4/5-A, FON14-2-A, LLA15-6-B	
		FON15-3-B, EST15-3-A, FON14-1-B	

Table 5-12 Synthesis of the cluster plot analysis with k-means with k determined from the dendrograms.

Results from both analyses	
High certainty groups	Uncertain groups
EST15-1-A	EST15-3-B, FON14-1-A
RIN14-1-A	FON15-3/5-A, LLA15-3/4/5-A
EST15-3-A	
RIN15-3/4/5-A	
LLA14-2-B	EST15-3-B, FON15-3/5-A, FON14-1-A, LLA15-3/4/5-A, RIN14-1-B
LLA15-4/5-D	
LLA14-2-C LLA15-6-A	FON14-2-A, LLA15-6-B, RIN14-1-A, RIN15-3/4/5-A, EST15-3-A LLA15-3/4/5-B, LLA15-3/4/5-C FON15-3-B, FON14-1-B LLA14-2-A LLA14-2-B, LLA15-6-C, LLA15-4/5-D FON15-3-B, RIN15-3/5-B, FON14-1-B

5.3.6 Tephra layer descriptions

Each layer in each lake core has been described stratigraphically. Layers which are expected to be the same within each lake amongst different cores are grouped under one tephra ID number.

5.3.7 Tephra correlation

The statistical analysis of geochemical fingerprints as well as the colour and morphological classification were combined with the chronology produced from radiocarbon and ²¹⁰Pb dating. Always taking the layer stratigraphy for each lake into account as the main parameter, a tephrostratigraphy for CNP was attempted using all statistical methods and visual analyses. Two tephrochronomarkers were identified with different certainty and these are labelled A and B in **Fig. 5-22**.

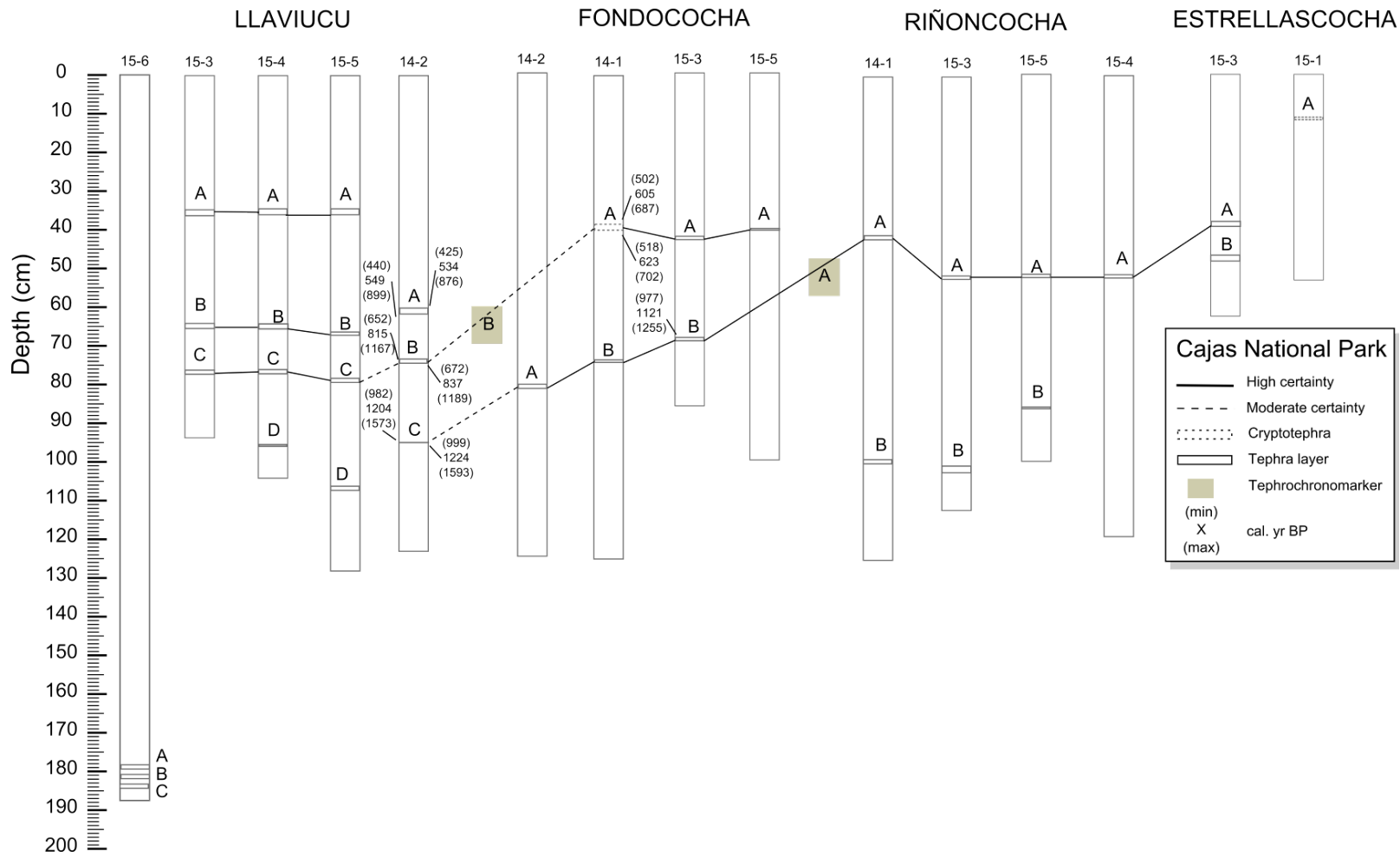


Fig. 5-22 Tephrochronology of Cajas National Park for the last 2000 years based on all available evidence (geochemistry, colour and morphology) as well chronology based on radiocarbon dating of some of the layers. The dashed lines joining different tepha layers represent moderate certainty correlations.

5.4 Wet chemistry analysis

5.4.1 Modern algae

Modern algae were investigated under the microscope so as to give an indication of the kind of material was analysed for isotopes. The sample of modern algae collected is considered to be a periphyton biofilm or an algal mat (**Fig. 5-23A**) consisting of extended filamentous growth (Bellinger and Sigeo, 2010). The algal mat consisted of mostly diatom species including *Tabellaria* sp. (**Fig. 5-23B, C and E**) and *Synedra* sp (**Fig. 5-23E**). Blue-green algae species of the order Chroococcales were also present in minor quantities (**Fig. 5-23D**).

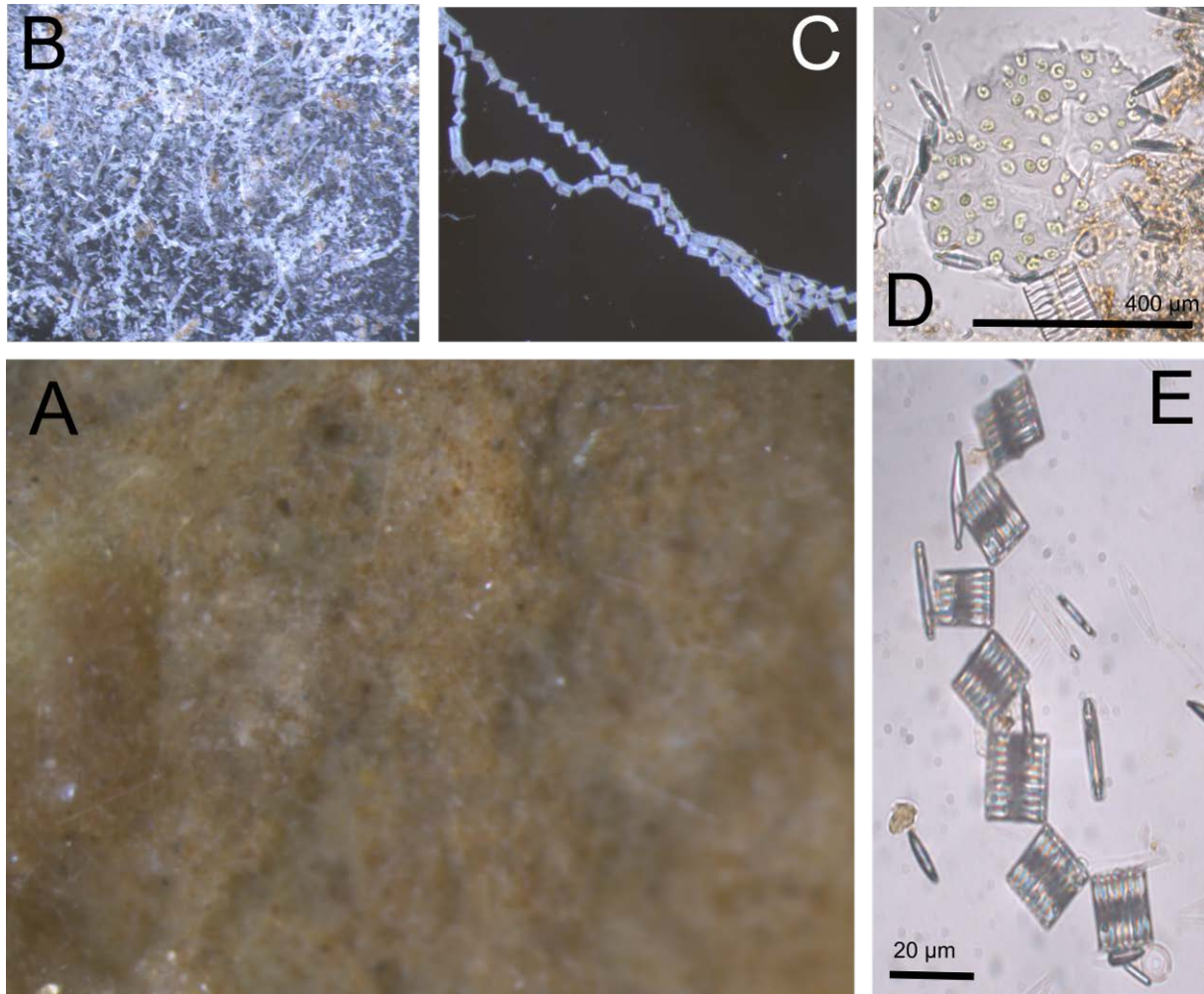


Fig. 5-23 Some of the organisms found in the modern algae sample. Specimens B-E were found within the biofilm A.

5.4.2 Elemental analysis and water content

L. Llaviucu samples were analysed at 6 mm resolution for the top 20 cm. Carbon and nitrogen were converted to fluxes and the C:N ratio was calculated (**Fig. 5-24**). Both curves display little variability before the 1960's. A significant peak can be seen in the C:N curve in 1961, after which variability starts to increase. A few years later, the C flux decreases suddenly. The C:N ratio is seen to decrease to the surface with another sharp peak in the year 2000. Meanwhile, the flux of carbon is gradually increasing to reach its highest value at the sediment surface. This is also

evident for nitrogen flux although the changes are small for both proxies. Water content was also measured for all L. Llaviucu samples. The water content is high, averaging 74% for the top 20 cm and is lowest between the years 1960 and 1988.

5.4.3 Stable isotopes

Stable isotopes of ^{13}C and ^{15}N were measured at a resolution of 6 mm along with the elemental concentration (**Fig. 5-24**). Both isotopes show similar results with a decrease in the ratios after 1968 and 1987 for carbon and nitrogen respectively. The decrease is gradual for nitrogen but abrupt for carbon although the overall changes are small. The change is on the order of -0.67‰ for ^{15}N and -0.60‰ for ^{13}C (change from the average of the 1984 - 1934 to 1985 - 2015). The $\delta^{13}\text{C}$ and $\delta^{15}\text{N}$ values can be plotted against one another to help visualize the changes through time (**Fig. 5-25**). The three different clusters identified by cluster analysis (see section 4.6.3) can be seen from the x-y biplot. The lower part of the sediment is clustering at higher $\delta^{13}\text{C}$ and $\delta^{15}\text{N}$ values and progressively moves to lower values during the late 1990s to the 2000s. The year 2013 yields very different values to the rest of the sediment. The sediment isotope signatures do not compare to modern algae values possibly because the (periphytic) biofilm may differ from planktonic communities.

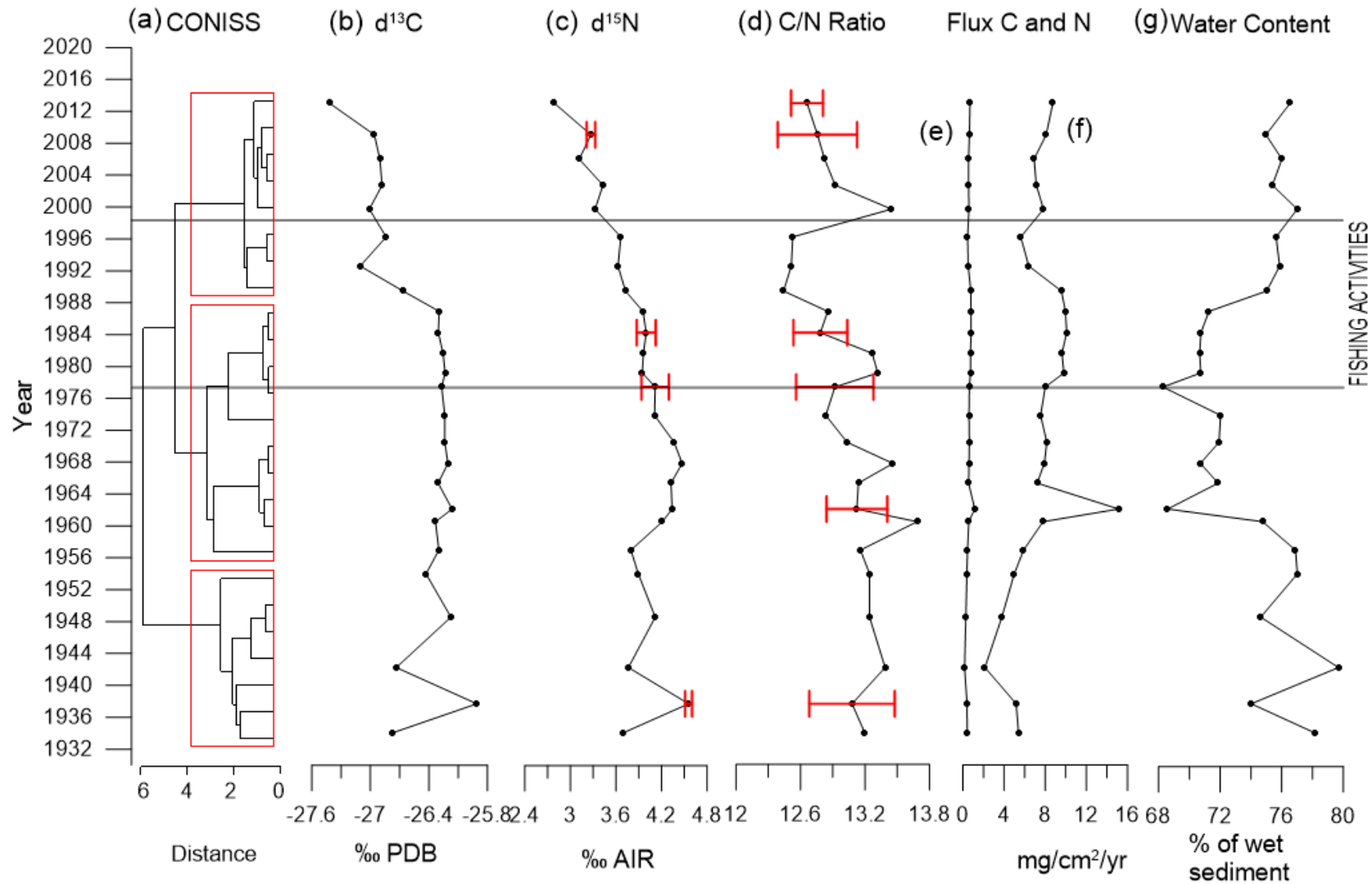


Fig. 5-24 . L. Llaviucu physiochemical profiles for (a) Constrained incremental sum of squares hierarchical clustering, (b) $\delta^{13}\text{C}$ profile, (c) $\delta^{15}\text{N}$, (d) C:N ratio, (e) nitrogen flux, (f) carbon flux and (g) water content. The datasets have been regularized in order to produce the dendrogram. Red error bars are calculated as the standard deviation from triplicate results.

5.4.4 Statistical analysis

Different constrained hierarchical clustering methods were tested on all the datasets mentioned above. Constrained incremental sum of squares (CONISS) and unweighted pair group method with arithmetic mean (UPGMA) were used. Both methods showed three clusters precisely at the same depth. Therefore, for simplicity of plotting, CONISS using R was favoured (Fig. 5-24a). No change in sediment was visible from neither the core description nor the core colour. The three clusters (1934 to 1952, 1953 to 1988 and 1989 to 2014) correspond well with changes in the physiochemical properties of the sediment. Clustering methods were also attempted on the isotope ($\delta^{13}\text{C}$ and $\delta^{15}\text{N}$) datasets only (Fig. 5-25). The resulting three clusters (1934 to 1977, 1978 to 1998 and 1999 to 2014) are not similar to the clusters visible from the dataset containing all proxies indicating the changes in isotopes in the profile are not significant (Fig. 5-24a). Interestingly, these isotope clusters fall in with the period of fishing activity (to the limits of the dating uncertainty). The same clustering periods were applied to a biplot of C:N ratio against $\delta^{13}\text{C}$ (Fig. 5-26).

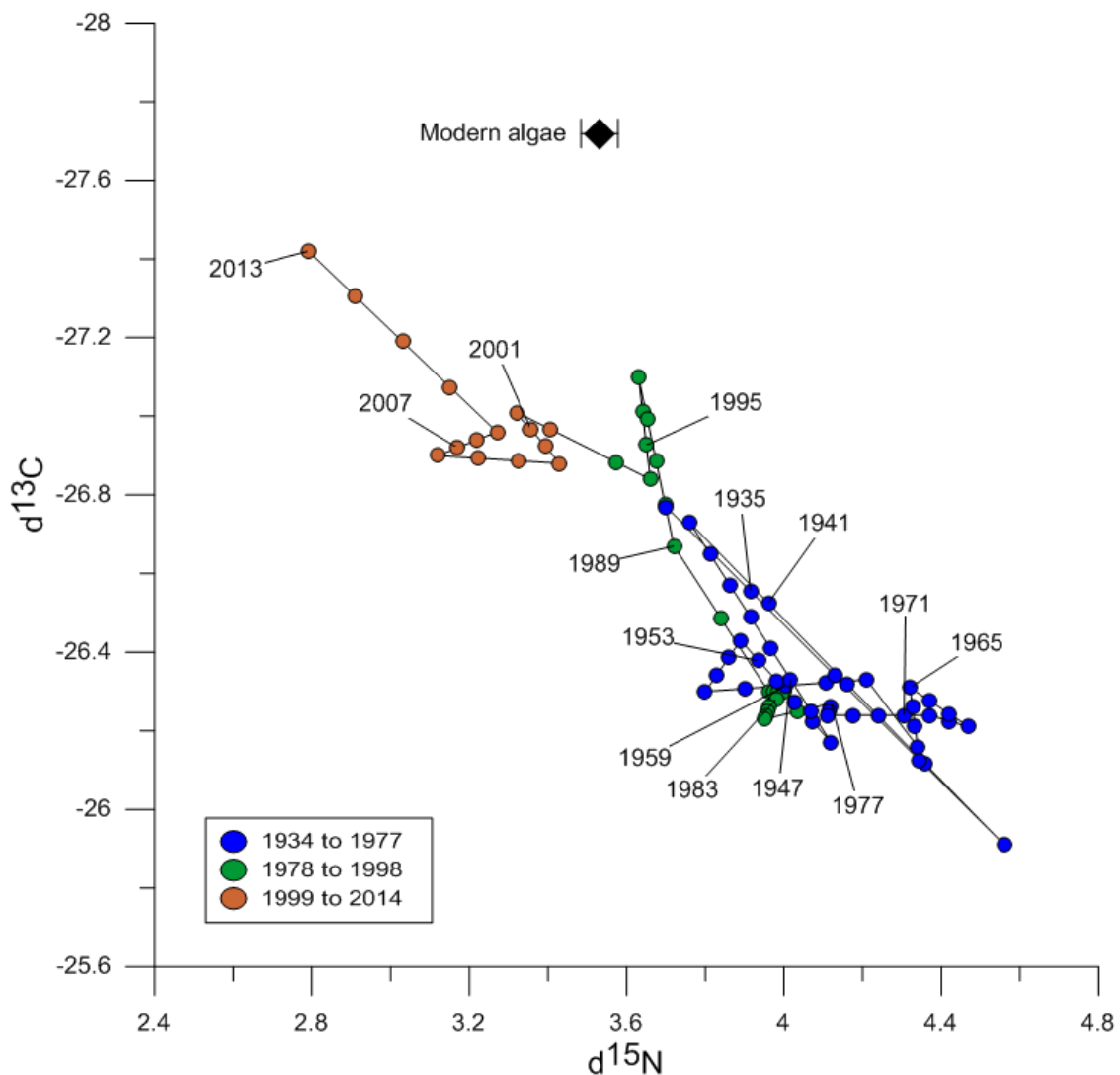


Fig. 5-25 $\delta^{13}\text{C}$ and $\delta^{15}\text{N}$ biplot using age regularized data. The colours correspond to the clusters identified through CONISS using only the isotope data. Modern algae isotopic values are also plotted. Algae $\delta^{15}\text{N}$ error is given.

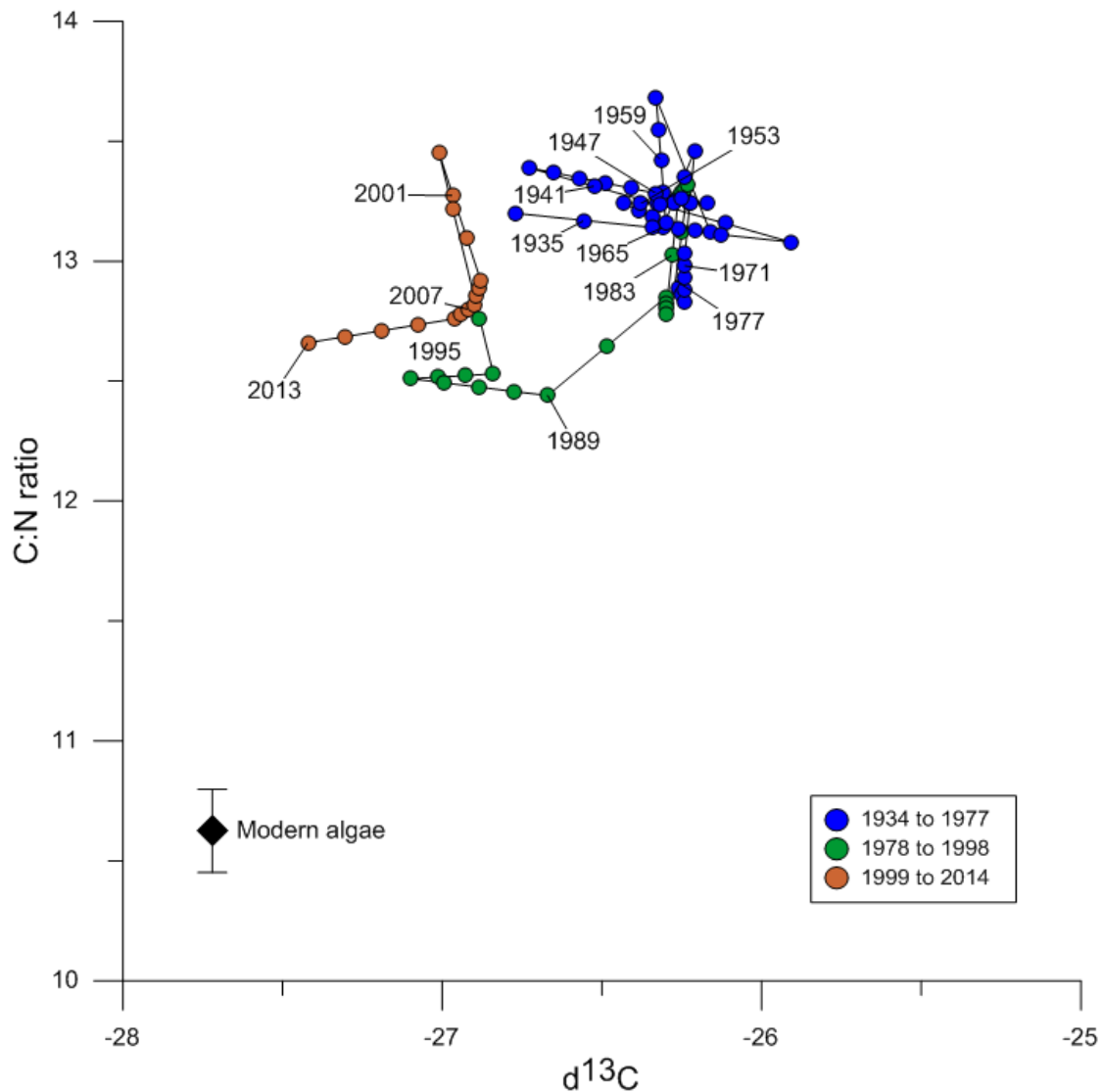


Fig. 5-26 $\delta^{13}\text{C}$ and C:N ratio biplot using age regularized data. The colours correspond to the clusters identified through CONISS using only the isotope data. Algae C:N error is given.

The past decade is very different to the rest of the record as seen in both biplots (**Fig. 5-25** and **Fig. 5-26**). However, the two decades of fishery activities also stand out from the background sedimentation mostly when looking at C:N against $\delta^{13}\text{C}$ (**Fig. 5-26**). It is very likely however, that the proxies are influenced by a mixed signal of the fishing and some other environmental changes.

5.4.5 Hyperspectral images

The sediment core of L. Llaviucu was scanned with the hyperspectral scanner and the spectral data was classified. Although the core sediment did not show any colour change, the top 10 cm is clearly different from the rest of the core (**Fig. 5-27**). Considering the age uncertainty in the ^{210}Pb age-depth model, the start of the geochemical change occurs at 1976 ± 1.8 years which coincides with the start of the fishing industry. Colour or geochemical hyperspectral change due to anthropogenic impact has been previously demonstrated on Antarctic and Chilean cores (Arcusa et al., 2015).

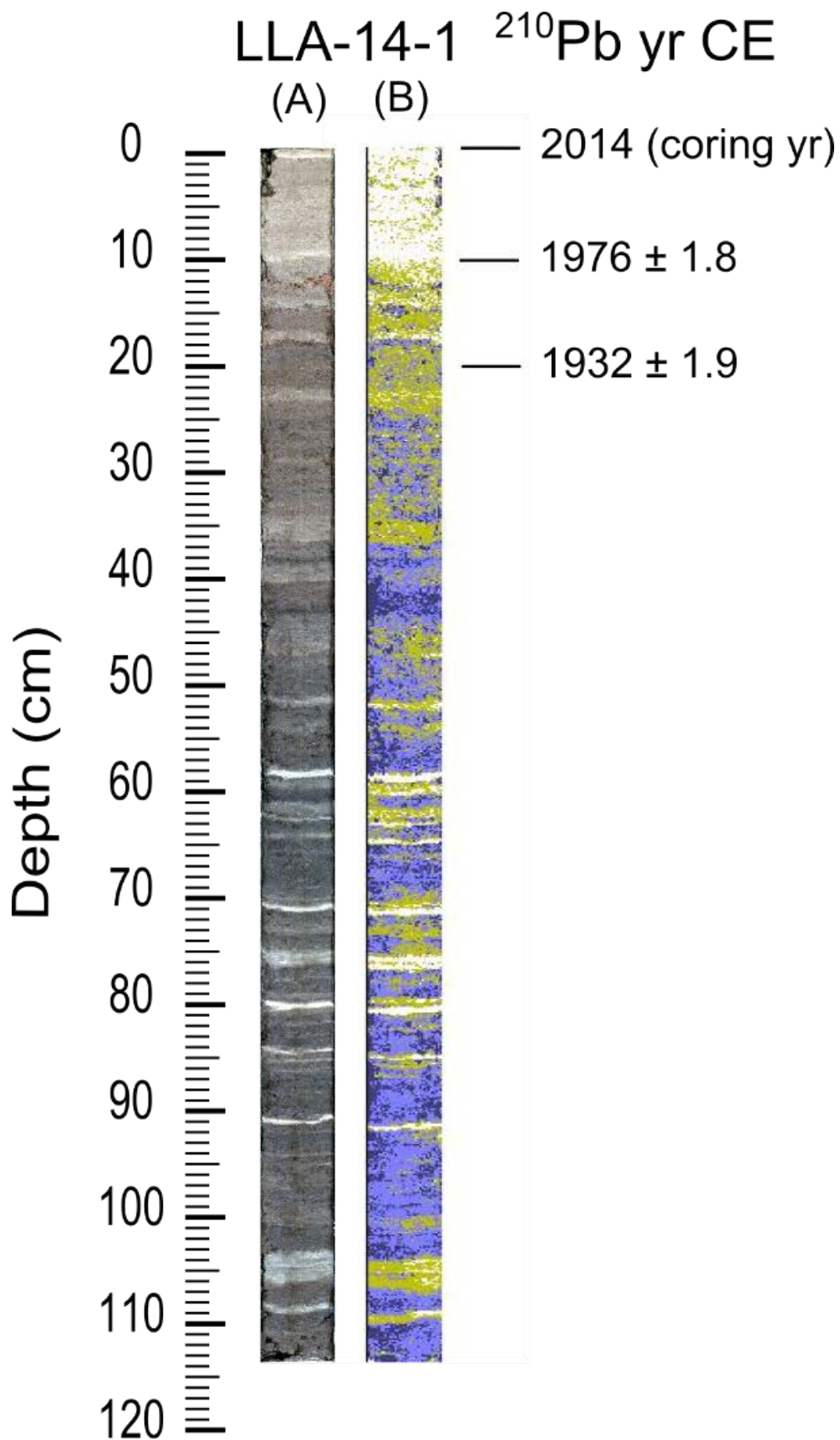


Fig. 5-27 . Image (A) and hyperspectral (B) scans of L. Llaviucu sediment core LLA14-1. The colours in B correspond to the classification from section 4.5.3. The corresponding ²¹⁰Pb years are given with their uncertainty.

6 Discussion

6.1 Age-depth profiles of Llaviucu and Fondocochoa

The limitations of any age-depth profile should always be taken into consideration. The CRS model was used to estimate the age-depth profile of L. Llaviucu and L. Fondocochoa for the most recent sediment. Both models also included a correction of the missing inventory, without which a tailing effect due to “old-date error” would remain for the lowest sediment (Binford, 1990; MacKenzie et al., 2011). The testing of numerous models (CIC versus several CRS) is not widespread in the literature but does offer significant improvements in the accuracy of the chronology (Tylmann et al., 2013; von Gunten et al., 2012). This is especially necessary in the absence of available independent chronomarkers as was the case for both profiles. The low ^{137}Cs concentrations (2.5 ± 1.1 Bq/kg in Llaviucu and 5.6 ± 3.0 Bq/kg in L. Fondocochoa) may be due to the location of CNP within the Cordillera corridor which French (1960) showed to receive much lower quantities of ^{90}Sr . ^{137}Cs is likely to behave similarly as both isotopes are produced from nuclear fallout. While no ^{210}Pb profile for L. Fondocochoa exists for comparison, Michelutti et al. (2015) measured a profile for L. Llaviucu which is significantly different to the profile presently presented. In fact, their CRS model did not take into account the missing inventory and thus a tailing effect becomes significant after 6 cm depth (Fig. 6-1). An uncorrected CRS model produces a systematic error during the calculation of the dates closer to the end of the profile which if not corrected shows increasing divergence from the true date (Appleby, 1998; Binford, 1990; Butz et al., 2015; MacKenzie et al., 2011; Tylmann et al., 2014).

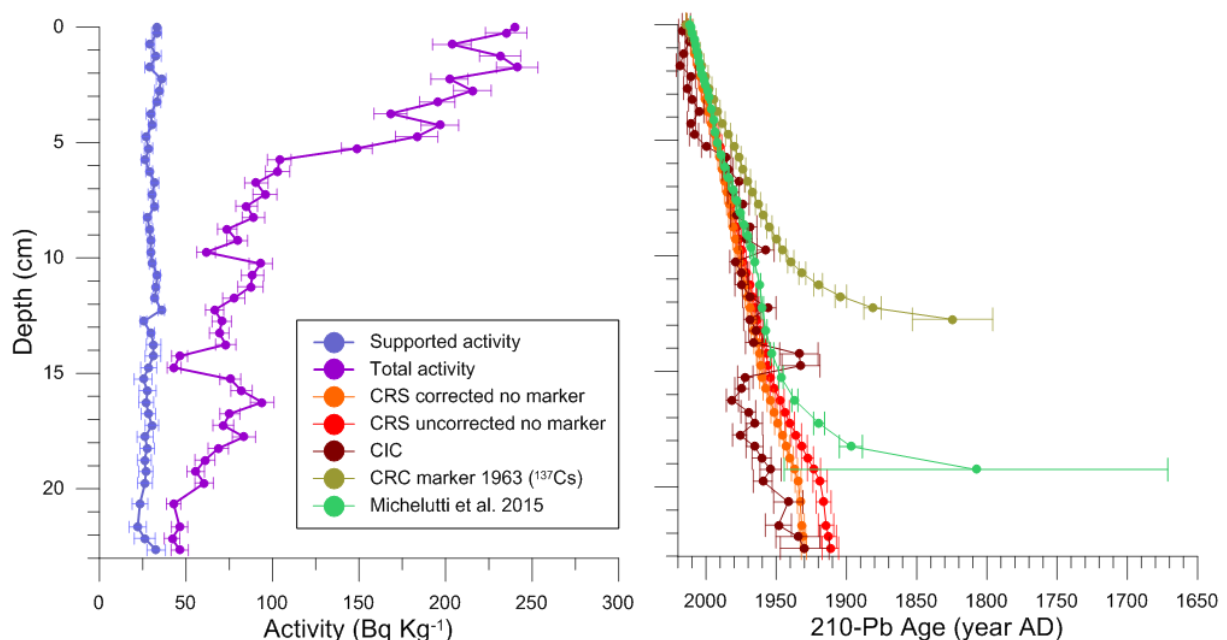


Fig. 6-1 Comparison of the different ^{210}Pb age-depths models for L. Llaviucu produced in this study with the CRS model from Michelutti et al. (2015). The CRS corrected no marker was used as the final product for this study.

As ^{210}Pb is limited to the last 85 and 141 years for Llaviucu and Fondococha respectively, radiocarbon dating of terrestrial macrofossils was used to extend their profiles to the last approx. 3000 years. The combination of both ^{210}Pb and radiocarbon profiles produces an apparent increase in sedimentation rates where the two models join (**Fig. 5-2** and **Fig. 5-5**). This is a phenomenon observed in other profiles (e.g. De Jong et al. 2013; Elbert et al. 2013) which may either be an artefact produced by the method or represent an actual change at the turn of the century. Dating of the last three thousand years presents some challenges such as large age uncertainties particularly due to plateaus within the ^{14}C calibration curve. In addition, carbon content of macrofossils <1.4 mg shows larger age deviations (Wohlfarth et al., 1998). In the case of Llaviucu however, the small macrofossil LLA15-6e (**Table 5-1**) was nonetheless useful to indicate a possible age. This age falls within the uncertainty of a similar depth in an age profile produced by Rodbell et al. (2002). The observed reservoir effect from bulk sample measurements indicate a possible input of old carbon from the recycling of up-river peatland organic matter as was indicated by Rodbell et al. (2002) for L. Chorreras also located in CNP. Consequently, the age depth profile produced by Colinvaux et al. (1997) which is based on bulk samples is considerably older by approx. 300 years and may need to be updated.

Event-deposit free sediment sequences are necessary to produce the best age-profile estimate (Gilli et al., 2013). Slump correction based on the thickness of flood and tephra layers effectively improved the sediment deposition profile of L. Llaviucu as was previously shown by Wirth et al. (2013). A slump-corrected profile would have implications for the calculation of mass accumulation rates used for example, in clastic sediment flux estimations (e.g. Rodbell et al. 2008). This correction would also improve the profile of L. Fondococha which also contains many layers.

6.2 Flood reconstruction of the last 3000 years

Extreme precipitation events are anticipated to increase in frequency with a warming climate (Kämpf et al., 2012; Schillereff et al., 2014). However, instrumental or observational data are not available for longer than a few decades for the area around CNP. This makes future predictions problematic. Flood reconstructions from clastic layers in lake sediment provide a proven alternative (e.g. Rodbell et al. 1999; Wirth et al. 2013).

Reconstructions using XRF, visible imagery and magnetic susceptibility have been previously attempted (see Gilli et al. 2013 for further reading). Here, the Ti/K ratio, visible observation and hyperspectral classification were used. Increases in Ti/K ratio values have been shown to relate to grain-size variations with Ti particularly relating to changes in catchment runoff (Davies et al. 2015). In L. Llaviucu, the co-variance of Ti and K was useful to identify influx of clastic sediment, although the changes in grain size between flood layers and background sedimentation (coarse to fine silt respectively) were subtle. However, peak values did not always correspond to visible layers and occasionally coincided to tephra layers.

Hyperspectral imaging has been shown to distinguish between different types of materials based on their spectral signatures (Mix et al., 1992). Using supervised and unsupervised classification, it was hoped that a more comprehensive identification of flood layers could be reached. This method was hypothesized to support the discrimination between flood and tephra layers, which in L. Llaviucu appear very similar to both the naked eye and microscopic analysis. However, due to its location in a volcanic catchment, the spectral signature

of weathered clastic material is very much related to what a tephra layer would show. Supervised classification based on classes of background sedimentation as well as organic flood and tephra layers was attempted using training areas (**Fig. 4-1**). However, the input of catchment material hindered the discrimination between the different classes i.e. the signal was mixed. Additionally, the darkness of the sediment further blurred the hyperspectral signal (Butz et al., 2015). Unsupervised classification was also attempted and resulted in a more useful classification although the finer clastic layers were not recognized by the statistical method. Furthermore, tephra layers were not all classified accordingly, which once again pointed to the problem associated with erosion from volcanic bedrock.

Visible measurements were thus combined with the XRF and hyperspectral results to map the layers. Layer thickness which has been hypothesized to reflect flood discharge volume (Wirth et al. 2013) was also measured. However, Kämpf et al. (2012) showed that the thicker layers are found nearest to the inflow and do not necessarily correlate to the discharge. Although the three methods were considered, the core correlation highlighted a real problem of heterogeneous sediment deposition along the lake basin and the consequent absence of flood layers. While every care was taken to include all flood layers, missing events remain a possibility. This problem has been highlighted by Kämpf et al. (2012) and Gilli et al. (2013). Interpreting sediment deposition as representing a single flood event necessitates confidence that material accumulation reflects hydro-geomorphic processes occurring in the catchment (Schillereff et al., 2014). In order to verify the flood reconstruction, a comparison to discharge or local precipitation data should be attempted. However, this was beyond the scope of this study.

Two further issues with the reconstruction have been identified. Firstly the chronology contains some uncertainty which was discussed in section 6.1. This would directly affect the flood frequency reconstruction as well as any comparisons made. Secondly, dense organic layers (**Fig. 5-**) have been identified throughout the cores both visually and through higher C:N ratios (**Fig. 5-24d**). Whether or not these can be interpreted as flood layers is undefined. By definition, a flood layer is composed of purely clastic, coarse material low in organic content (Gilli et al., 2013; Schillereff et al., 2014) with a different structure to a mass movement deposit which would contain reworked lacustrine sediment (Gilli et al., 2013). L. Llaviucu is surrounded by dense vegetation (**Fig. 2-5**) with few exposed surfaces, but the inflow of Rio Taitachugo would bring material from the whole catchment area. It may be possible that a particularly windy precipitation event might disturb the local vegetation and produce these layers. However, no examples of organic flood layers have been found in the literature.

One attempt to validate the L. Llaviucu flood reconstruction was to compare it to existing records (**Fig. 6-2**). A flood reconstruction has previously been attempted for L. Pallcacocha in CNP (Moy et al. 2002; Rodbell et al., 1999) which is located at higher altitude in a different ecotope than L. Llaviucu. A comparison of L. Llaviucu to L. Pallcacocha flood frequency (Moy et al., 2002) shows that much fewer events have been recorded in the former than the latter for the same period of time when considering the same time-averaging window. Additionally, the L. Pallcacocha fails to record the sharp increase in events over the last 150 years. However, a broad similarity could be visualized with lower frequencies around 1200 C.E. and around 0 C.E. While Rodbell et al. (1999) and Moy et al. (2002) have attributed their L. Pallcacocha record to moderate to strong El Niño events, there is mounting evidence that La Niña might in fact be responsible. Based on instrumental and reanalysis data, Vuille et al. (2000) and Morán-Tejeda et al. (2016) have indicated that the Ecuadorian Inter-Andes receive more precipitation during La

Niña events than during El Niño events. This observation however, complicates the L. Pallacocha interpretation which has been linked to El Niño events. This could be partly explained by issues in the methods employed in producing the chronology. Namely, that the event model used assumes each laminae to be deposited during an ENSO event.

Based on the El Niño hypothesis, Rein (2007) has brought to attention the so called “Medieval El Niño anomaly” where fewer or no events have been reconstructed during the period 800 - 1250 C.E. While the L. Llaviucu reconstruction does see fewer events, this is limited to the period 1000 - 1200 C.E. This interpretation differs widely from reconstructions by Ledru et al. (2013) who showed enhanced ENSO variability during the Medieval Climatic Anomaly. The difference might be a result of the proxies used. Rein (2007) used reflectance spectra from a marine core off the coast of Peru while Ledru et al. (2013) used a transported pollen/*Poacea* ratio from Ecuadorian eastern Andes cores. This opposite interpretation might further support a La Niña flood layer hypothesis in the Inter-Andean region. Much more striking is the paucity of events during the period 500 B.C.E. to 500 C.E. which is also visible from the Moy et al. (2002) record. However, comparison to instrumental data will be necessary for validation.

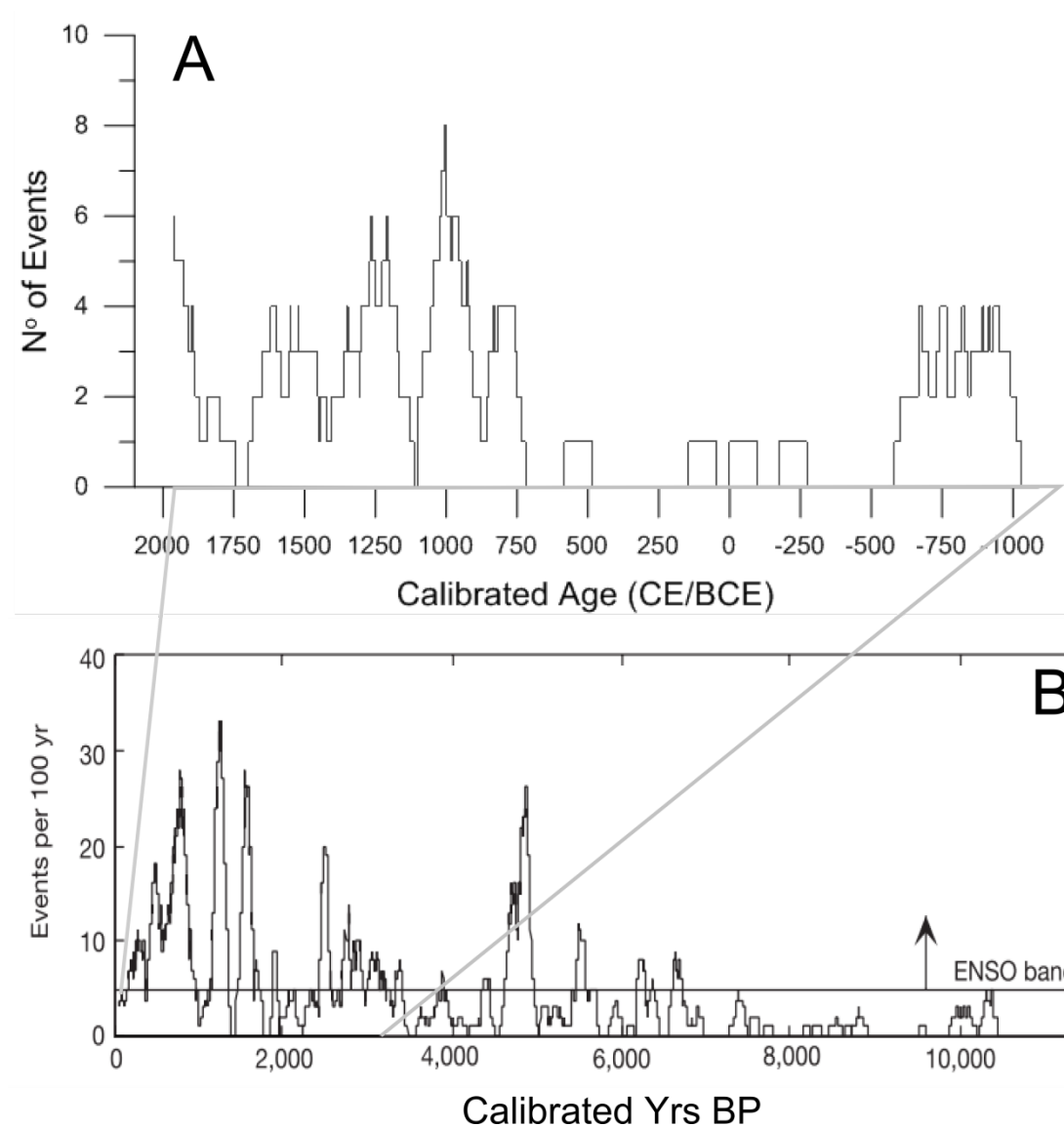


Fig. 6-2 Flood event comparison of this study (A) to Moy et al. (2002) (B) for the last 3000 years.

6.3 Tephrochronology of CNP

Two tephrochronomarkers were identified based on age, stratigraphy, morphology, colour and geochemistry (**Fig. 5-22**). Tephrochronomarker A links tephra layers LLA14-2-B and LLA15-3/4/5-C to cryptotephra FON14-1-A and the thick layers of FON15-3/5-A. On the one hand, the linkage between the L. Fondococha layers is based on their similarity coefficient, their geochemistry and their colour. On the other, the linkage between the L. Llaviucu layers is based solely on stratigraphy when considering LLA1 is visually missing from core LLA14-2. However, this layer might still be present as cryptotephra but was not identified by the scanning methods, as is further discussed later. Similarly, the correlation between the two lakes is based on a chronology which, when taking the age uncertainty of 200-500 years into account, weakens the correlation certitude of tephrochronomarker A. However, the two dated layers are in good age agreement with the ages of 837 (min 672, max 1189) cal. yrs BP for L. Llaviucu and 623 (min 518, max 702) cal. yrs BP for Fondococha. Taking the age uncertainties into account, marker A thus has an upper and lower bound of 518 and 1189 cal. yrs BP respectively. The second tephrochronomarker B links tephra layers LLA14-2C, FON14-2A, FON14-1B, FON15-3B, RIN14-1A, RIN15-3/4/5A and EST15-3A. The linkage has high certainty amongst all except for LLA14-2C. While the highly certain correlation is based on their similarity coefficient, colour and geochemistry but not their morphology, the correlation of LLA14-2C to these other layers is based solely on chronology. Like the uncertainty in the age for tephrochronomarker A, the age bracket for the second marker is of the order of 400-600 years. However, LLA14-2C is in good age agreement with the other L. Fondococha dated layer with a minimum age of 1204 (min 982, max 1573) and 1121 (min 977, max 1255) cal. yrs BP, respectively. The L. Llaviucu layer gives a maximum age of 1224 (min 999, max 1593) cal. yrs BP. As only a minimum age is available for the Fondococha layer, this dating gives a minimum and maximum age of 977 and 1593 cal. yrs BP respectively, to tephrochronomarker B.

6.3.1 Volcanic origin of the layers

An important aspect of tephrochronology is the attribution of layers to a volcanic eruption. Fine-grained tephra may travel thousands of kilometres as deposition of Indonesian Agung tephra in Antarctica ice cores attest (Alloway et al., 2013; Lowe, 2011). As a result, the possible origin of the CNP tephra layers extends over a wide area. Within the scope of this thesis, the literature was searched for geochemical data available for Ecuadorian volcanoes, in particular Tungurahua, Sangay, Cotopaxi and Quilotoa which are some of the closest volcanoes to the park (**Table 6-1**). Rare earth elements (REE) and some minor element concentrations measured by ICP-MS were found although most of these were measured from the volcanoes themselves and not specific eruption events. REE concentration for Sangay, Cotopaxi and Tungurahua volcano cones are plotted in **Fig. 6-3** with the CNP tephra layers. As will be discussed further in section 6.4.1, the REE compositions of all these volcanoes are highly similar. However, they are most comparable to layer EST15-1-A in CNP in terms of the REE and the composition of Cotopaxi (CTX-50) measured by Garrison et al. (2011) shows the closest statistical similarity (unpaired t-test, $df = 18$, $p > 0.01$). Further analyses on minor elements as well as thorough statistical analyses should be attempted to validate this claim. Unfortunately, this Estrellascocha layer is not correlated to any other CNP layer.

In 1280 C.E. an enormous Plinian eruption of Quilotoa occurred (Mothes and Hall, 1998; Stewart and Castro, 2016). Minor element x-y biplots (**Fig. 6-4**) show that this eruption

corresponds closely to tephrochronomarker B as compared to the other volcanoes. This dacitic eruption ejected fine white ash which has been identified in 1 cm thick layers around Ecuador (Mothes and Hall, 1998). The colour of tephrochronomarker B is greyish white which would also correspond. However, this eruption was dated to 785 ± 50 uncal. yr BP as best estimate (Mothes and Hall, 1998) which would correspond to approximately 1280 C.E. (Stewart and Castro, 2016). The age of marker A would correspond better given the age uncertainty but the geochemistry is equivocal. It therefore remains uncertain from which volcanoes these chronomarkers originated.

Table 6-1 Origin and reference of comparison data of tephra from Ecuadorian volcanoes.

Volcano	Sample Name	Material	Reference
Sangay	SAN26B-WPL-F	Sangay III white	Monzier et al. (1999)
Cotopaxi	CTX-50	Cotopaxi IIB rock	Garrison et al. (2011)
Quilotoa	Pumice1	Pumice	Mothes and Hall (1998)
	Pumice2	Pumice	Mothes and Hall (1998)
	Ash1	Ash	Mothes and Hall (1998)
	Ash2	Ash	Mothes and Hall (1998)
	Ash3	Ash	Mothes and Hall (1998)
Tangurahua	TUNIIIAA	acid andesite rock	Hall et al. (1999)
	TUNIIIBA	basaltic andesite rock	Hall et al. (1999)
	TUNIIID	Dacite rock	Hall et al. (1999)

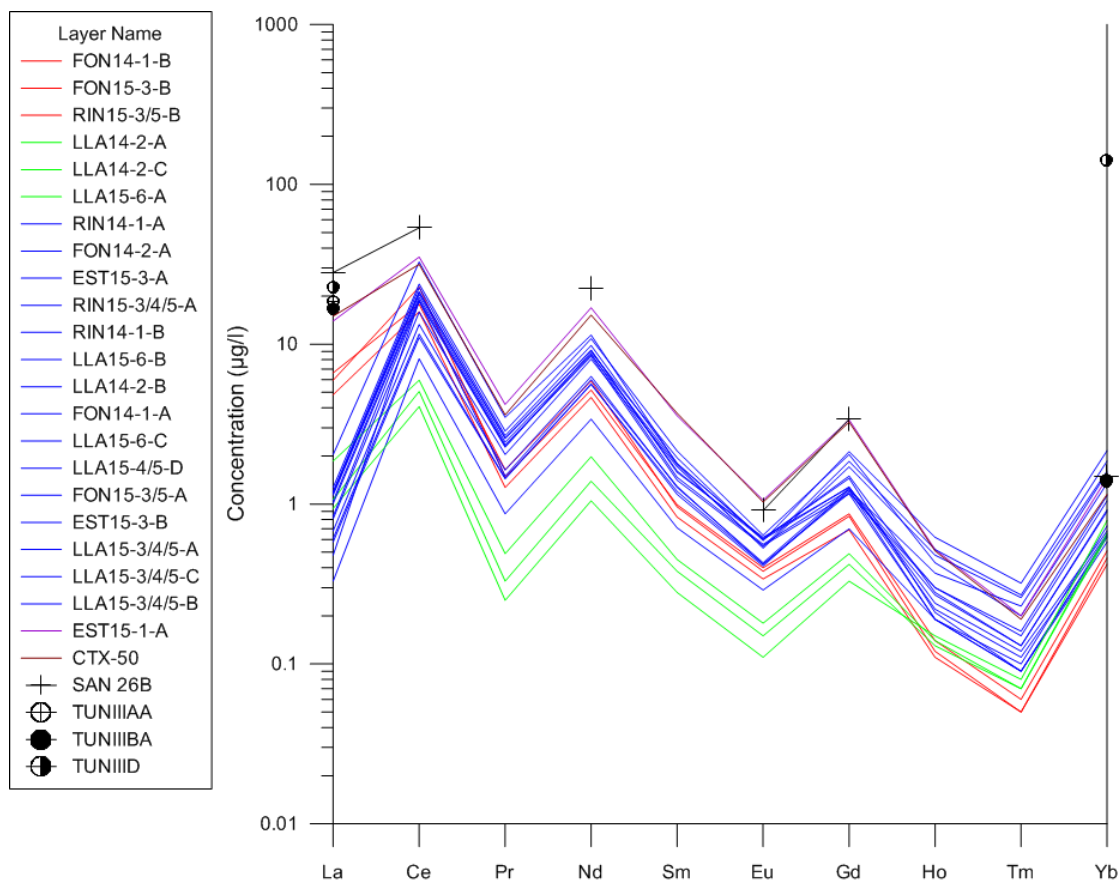


Fig. 6-3 Line plot of the REE of the A1 dataset. The layers are grouped based on the shape of the line. The y-axis has a log scale. The concentrations of available volcanic REE measurements by Monzier et al. (1999), Hall et al. (1999) and by Garrison et al. (2011).

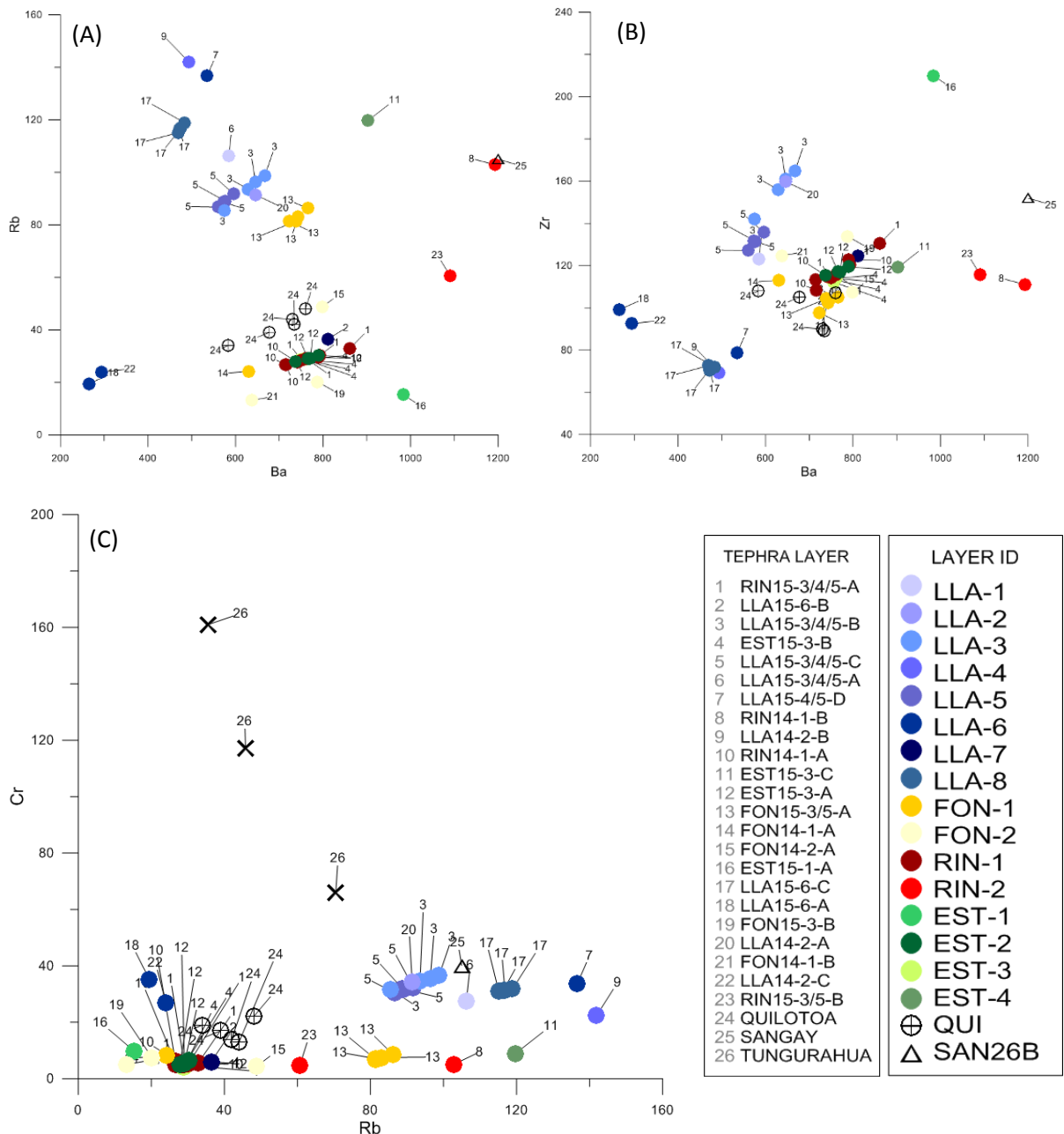


Fig. 6-4 Elemental x-y biplots of Ba against Rb (a) and Zr (b) for the CNP layers. The Quilotoa 1280 C.E. eruption fingerprinted by Mothes and Hall (1998) is labelled as QUI. The youngest Sangay cone composition by Monzier et al. (1999) is labelled SAN. The Tungurahua cone composition by Hall et al. (1999) is plotted in (c) and labelled as TUN.

6.4 Uncertainties and limitations of the tephrochronology

6.4.1 Tephra type

Tephra correlations can only be firmly established if their stratigraphy, age relations and glass properties agree (Lowe, 2011; Pearce et al., 2008). Tephrochronomarker B, discussed above, shows clear signs that many aspects agree. On the contrary, marker A is more uncertain. The difficulty in correlating the different tephra layers is related to a few conditions. Firstly, CNP is located on volcanic bedrock which according to Lim et al. (2008) already poses difficulties in terms of erosion. Shane (2000) indicated the higher potential of distal (>100 km from source)

horizons to contain mobilized material, often by fluvial processes. Furthermore, Ecuadorian volcanoes produce andesitic tephra which is more prone to weathering. This influences the geochemical fingerprint, unless the weather layer can be successfully removed (Pollard et al., 2003; Shane, 2000). In fact, andesitic tephra have been recognized as being notoriously difficult to fingerprint (Shane, 2000). Moreover, individual tephra composition are not always unique and in many sequences the same composition may be located at various stratigraphic levels (Shane, 2000). Although in theory trace elements are useful in differentiating amongst volcanic events (see Pearce et al. 2008 for examples), this is not always the case (e.g. Brendryen et al. 2010; Lowe 2011; Shane 2000). Shane (2000) gives the example of Okataina eruptions in New Zealand having the same composition as the Taupo volcano over the last 22 ka. In the context of Ecuadorian volcanoes, available REE concentrations (**Fig. 6-4**) have shown that Turungahua, Cotopaxi and Sangay, have similar fingerprints. On the other hand, Quilotoa appears to be different in terms of minor element composition. The dissimilarity between the volcanoes may be influenced by their location as Quilotoa is located in the Western Cordillera unlike the others. Additionally, elemental and REE ratio x-y biplots have shown from triplicates a wide heterogeneity within the samples. It is thus likely that some of the non-replicated samples may have a more heterogeneous nature than cannot be distinguished from the available data.

6.4.2 Tephra deposition

Tephra layers are usually assumed to have been deposited rapidly, without reworking and uniformly (Pyne-O'Donnell, 2011). Although the first assumption might hold true at CNP until evidence shows otherwise, the latter two assumptions are not supported. The intra-core correlations revealed in L. Llaviucu demonstrate a replication of tephra in a setting conducive to reworking. Conditions which may lead to both catchment and basin reworking may include the lake's small size (0.14 km²) relative to its catchment (51 km²; Barros and Carrasco 2006), the narrow and steep sided (45° approx.) valley in which it is located, as well as its high sedimentation rate (mean 0.5 g cm⁻² yr⁻¹). In particular, the large drainage basin relative to the surface area might produce a focusing effect from both runoff and fluvial processes. A similar observation was made by de Fontaine et al. (2007) for two closely located lakes in Alaska, one of which contained almost five times more tephra layers. The effect of catchment size was also mentioned by Pyne-O'Donnell (2011) along with the proximity to the river inlet as primary variables influencing deposition. The Llaviucu cores were, however, retrieved from the deepest part of the basin which might not be influenced by Rio Taitachugo.

The third assumption of uniform blanketing is likewise not supported based on intra and inter-basin correlations. Parallel cores from Fondococha and Riñoncocha (and to a lesser extent also Estrellascocha because of the assumption of very low sedimentation rate) did not possess the same number of tephra layers. Furthermore, thick visible layers such as FON15-3/5-A was only located as a cryptotephra in FON14-1-A and not at all in FON14-2. Variable deposition within the same lake indicates causes that are limnologic. Micro-basin morphological variations may allow deposition in one location but not another while sub-lacustrine currents may influence erosion. These effects have all been described in the literature for various site locations (e.g. Boygle 1999; de Fontaine et al. 2007; Pyne-O'Donnell 2011; Watson et al. 2016). In particular, Watson et al. (2016) make the point that small fallout events might produce thick tephra layers at one lake location due to redistribution. This type of redistribution might explain patchiness in the intra-basin deposition records. Inter-basin deposition also appeared irregular as younger tephra records were not found in all the lakes. For example, tephrochronomarker A

was only found in L. Llaviucu and L. Fondococha but not in L. Riñoncocha or L. Estrellascocha. The very low sedimentation rate might explain the absence in Estrellascocha. Therefore, only large scale processes such as wind patterns, vegetation cover, local weather or geomorphological barriers and mechanisms could explain this variation. A plausible reason why marker A was not found in Riñoncocha might be that the lake is a closed system with a small catchment area. Little soil is exposed and vegetation cover in the form of páramo might be trapping and preventing tephra from being transported into the lake by runoff. Additionally, the basin is exposed to stronger winds which might prevent deposition. The importance of fluvial transport and deposition was discussed in detail by Shane (2000) as a plausible cause for contemporaneous sequences containing different numbers of layers. Uneven distribution of tephra layers clearly demonstrates that the use of parallel cores is crucial to produce a complete tephrochronology (Boyle, 1999; Pyne-O'Donnell, 2011; Shane, 2000; Watson et al., 2016)

6.4.3 Methodology: tephra identification

Although a range of techniques was used to find tephra layers, the actual identification was challenging. Scanning techniques such as XRF, MS and visible reflectance have been shown to rapidly indicate the location of tephra and in particular cryptotephra (Gehrels et al. 2008; Lowe 2011; Davies et al. 2015). However, the scanning techniques were only partly successful for the CNP cores. MS data could only locate the thicker visible tephra, a limitation also acknowledged by Gehrels et al. (2008). This is likely to be the result of the coarse scanning resolution of 0.5 cm. Furthermore, the statistical procedures using hyperspectral data could not differentiate between the different sediment types. This is likely a consequence of the high water content at the surface of the core (e.g. Gehrels et al. 2008) as well as the darkness of the sediment (Butz et al., 2015). However, visible to near infrared hyperspectral images have never been previously used to detect tephra. The only example found is from Caseldine et al. (1999) who used long-wave ultraviolet and blue wavelengths with a spectrophotometer on peat cores. On the contrary, XRF data was the most optimised method, especially the element Sr which located several cryptotephra. It is however likely that not all cryptotephra were located due to their thinness compared to the scanning resolution. It is also possible as Gehrels et al. (2008) and Kylander et al. (2012) pointed out, that low concentrations of shards away from the sediment surface may also be a limiting factor. Nevertheless, the hyperspectral method showed some promising results which would require some fine-tuning. A combination of both this and XRF scanning would optimise the non-destructive search for cryptotephra.

Identification challenges were not limited to the scanning but also to the visual observation under light and scanning electron microscope. The potential for misidentification arose due to several aspects. Firstly, the cleaning technique discussed below was not optimal and non-tephra material remained. Especially, the occurrence of phytoliths (plant biogenic silica) which appears and behaves the same as tephra remained abundant. This was also an issue encountered by Blockley et al. (2005) but would mostly affect the Si concentration which in any case could not be measured with total digestion. Minerogenic particles such as pyroxene and amphiboles of non-tephra fallout origins may also have looked similar to tephra. Secondly, many tephra particles demonstrated varying degrees of weathering with very few fresh glass particles present. This effect of grading into glass-free, clay bearing bentonites was highlighted by Pearce et al. (2004) and impeded both the identification and the geochemical fingerprinting. The andesitic nature of the volcanoes in Ecuador means the tephra is commonly mineral-rich, glass-poor and weathers rapidly (Shane, 2000). Fourthly, the very small size (<100 µm) of the tephra

particles made the identification through light microscopy alone problematic. Scanning electron microscope analysis provided much clearer identification possibilities although the degradation of the particles added some difficulties. Finally, it became clear that tephra reworking especially in a volcanic landscape was a real endeavour as discussed by Lim et al. (2008). The soils in CNP contain > 5% volcanic grains as identified by Buytaert et al. (2006). The uncertainty was greatest in L. Llaviucu where thin, fine grained but nonetheless clastic laminae are abundant and easily misinterpreted to be a tephra layer from the composition. The problem was also noted by Rodbell et al. (2002) for L. Pallcacocha in the same park. Crucially, Lowe (2011) warned that if tephra is reworked or too extensively dispersed then interpretation of material becomes complex and less viable as an isochron. All CNP layers sampled showed clear lower boundaries indicating discreet events, although the upper part was sometimes diffuse indicating later reworking. However, the material within some of the layers might have eroded from the volcanic bedrock and due to their degraded condition, in general, could have been misidentified as tephra. There was thus the potential to confuse primary from secondary tephra (Boygale, 1999).

6.4.4 Methodology: cleaning and measurement

Although the study found two potential tephrochronomarkers, it must be pointed out that the correlations between some of the layers remain uncertain. This uncertainty arises mainly from the methodology which only partly succeeded in extracting an unmixed signal. The limitations in the methodology followed two main aspects. The first involved the cleaning procedure of the bulk sample while the second concerned the measurement process. First and foremost, most of the CNP tephra were <42 μm in size. Very fine-grained material is difficult to work with and mostly point to distal volcanic sources. Such small particles have often been described in Antarctic ice core studies (e.g. Basile et al., 2001; Palais et al., 1990) where site locations are >500 km from the nearest volcano. Although single shard analysis on such small surfaces is nowadays possible, it is difficult and time consuming. Kuehn and Froese (2010) established a flexible method to prepare fine (3-5 μm) grains for electron micro-probe analysis. Furthermore, Hayward (2012) has shown that precise and accurate measurements are now possible down to 3 μm . Similarly, Pearce et al. (2004) did demonstrate the opportunities that laser ablation ICP-MS can provide for high precision analysis of particles as small as 40 μm . Yet, these methods all rely on the necessity to pick numerous micron-sized grains by hand.

In consequence to the size problem, bulk chemical analyses have been attempted in the past (e.g. Arculus et al., 1995; Bryant et al., 1999; Straub 1997) and have shown promising results according to Pearce et al. (2004). However, as many authors have remarked, tephra purification is a crucial prerequisite for reliable correlation of layers (Blockley et al., 2005; Bryant et al., 1999; Lowe, 2011; Pearce et al., 2004; Shane, 2000; Turney, 1998). Explicitly, a tephra layer is often composed of a mixture of glass, lithic fragments and microlites (Basile et al., 2001). However, the further away from the volcanic source, the stronger the contamination by other detrital material such as diatoms, biogenic silica, and xenoliths (Blockley et al., 2005; Pearce et al., 2004; Shane, 2000). This material is not representative for the tephra (Bryant et al., 1999) and only the glass shards have been shown to be suitable for correlation (Daga et al., 2014; Pollard et al., 2003; Shane, 2000). In consequence to the small particle size and in response to the findings from other researchers, it was attempted in this study to find a more thorough cleaning procedure.

The separation into different density fractions using heavy liquids have been shown to be an efficient procedure to remove unwanted material (Blockley et al., 2005; Eden et al., 1992; Straub, 1997; Turney, 1998). The changes made in this study from the original method by Turney (1998) enhanced the removal of clay particles which were highly abundant, which Pearce et al. (2004) suggested might be in fact altered tephra. Nevertheless, this cleaning procedure had several limitations. Firstly, no sample was completely devoid of foreign material by the end of the procedure as mentioned by Bryant et al. (1999) and Shane (2000). Secondly, even subtle changes in the heavy liquid density had drastic effects on the recovery, a problem also noted by Blockley et al. (2005). Furthermore, the density procedure would have needed to be adapted for every tephra layer (Turney, 1998) and the procedure does not capture the basaltic denser component (Blockley et al., 2005; Mackie et al., 2002; Turney, 1998). The attempt to concentrate these basaltic shards using the magnetic separator following the method by Mackie et al. (2002) failed due to the small particle size. Finally, no liquid medium is ever chemically inert (Blockley et al., 2005). Like Turney (1998) who found sodium polytungstate coated particles for a minimum of three washes, we found the samples needed at least ten washes to be rid of this coating. However, from ICP-MS results it did not appear that any contamination was present.

Solution nebulisation ICP-MS is generally considered to be an accurate analytical method (Pearce et al., 2004). However, limitations do exist both in sample preparation and in the sample measurements which may explain some of the poorer elemental recoveries in this study for ^{43}Ca (21.19%) in particular. On the one hand, total digestion may sometimes not fully dissolve resistant minerals which may explain low CRM recoveries (Briggs and Meier, 2002). Furthermore, low abundance elements (e.g. Tm and Zr) are unlikely to reach dissolved concentrations which would allow for precise measurement (Pearce et al., 2004). Moreover, microwave malfunction, insufficient cooling time and inaccurate weighing may also cause discrepancies. As a consequence of any of these limitations, this study showed poorer recoveries for the REE in Batch 5mix (lower than 80%). Additionally, the total dissolution of tephra which is Si based precludes the measurement of this element. In acidic environments, ionic exchange of Si starts to occur and a solution of $\text{Si}(\text{OH})_4$ is produced which at high temperature may be lost as volatiles to varying amounts (Blockley et al., 2005). On the other hand, high recovery values might be related to insufficient dilution or contamination. A systematic increase as was the case in Batch 1 might on the contrary be a sign of mis-calibration warranting the correction that was made.

Limitations in sample measurement with the ICP-MS relate to various types of spectral and non-spectral interferences (Rüdel et al., 2011). Matrix effects, carry-over, instrumental drift and isobaric overlap all affect the analytical precision (Briggs and Meier, 2002; Rüdel et al., 2011). Many of these can be minimised through cleaning, internal standards and blank solutions (Rüdel et al., 2011). Furthermore, measurement uncertainty increases as the concentration in the sample decreases (Pearce et al., 2004; Rüdel et al., 2011). Importantly, the total dissolved solids must be in the 2 - 3% range (Pearce et al., 2004; Rüdel et al., 2011) as anything higher would increase the possibility of physical and spectral interferences significantly (Rüdel et al., 2011). Various studies which have used a version of solution nebulisation have measured sample weights from 6 mg (Straub, 1997) to 200 mg (Briggs and Meier, 2002). The present study used samples of 50 mg so as to make the analysis of triplicates possible. Finally, poorer CRM recoveries were attained in this study for rare earth elements but this is an issue discussed by Pearce et al. (2004) who indicate that for low abundance elements, precision reaches $\pm 20\%$

and becomes most imprecise for elements La to Lu. While taking these limitations into account, many of the elements were recovered to high confidence levels and produced robust elemental data.

6.4.5 Statistical correlation

Statistical methods have often been used as correlation aids with many positive results (Lowe, 2011). However, in the context of this study, conflicting results were obtained. Several datasets were investigated (A1 and B2 geochemistry, colour, size and morphology) and many different statistical methods have been employed (similarity coefficient, PCA, cluster analysis using various linkages) yet conclusive results were made with difficulty. Although Liu et al. (2015) used several datasets (componentry and composition) they did not use many methods, while Kuehn and Foit (2006) and Xia et al. (2007) used several statistical procedures (dendrograms and similarity coefficient) but on a single dataset. As a consequence, perhaps many datasets and procedures masked any relationship that could be found within CNP, but any one method on any one dataset actually produced conflicting results i.e. the correlation of layers which are not possible stratigraphically or in terms of age. For this reason, the use of multiple approaches was warranted. A closer look at simpler XRF data did support the conclusions drawn but even these showed inconsistencies, indicating that simpler data and procedures could not be used to correlate CNP layers. These conflicting aspects would explain why some layers within the same core appear similar and why drawing clear high confidence tephrochronomarkers was challenging.

6.4.6 Remarks to the limitations and uncertainties

It is necessary to be conscious of the limitations and uncertainties in tephrochronologies as were discussed extensively in the previous sections. However, it remains that this study established the first basis for a tephrochronology for south central Ecuador using lake sediments for the late Holocene. Not only did no previous study investigate this time period at this location, but it was suggested that the lack of layers may be indicative of fewer large eruptions or even a change in the wind direction during the last two millennia (Rodbell et al., 1999). The tephrochronologies presented in this study demonstrate this may not be the case and warrants for further investigations.

6.5 The impact of fishing and environmental and climatic change on lake geochemistry

The geochemistry of a lake is influenced by many different processes such as changes in the watershed as well as in-lake processes, anthropogenic impacts or climate change (Fig. 6-5). Geochemical analyses are necessary to disentangle them but this is often complicated. Significantly (unpaired t-test, $df = 13$, $p < 0.01$) decreasing trends in $\delta^{15}\text{N}$, $\delta^{13}\text{C}$ and C:N ratios were found for the top 20 cm of L. Llaviucu (Fig. 6-5) and the possible reasons are discussed in turn, particularly in relation to the impact the fishing activities might have had on the lake environment.

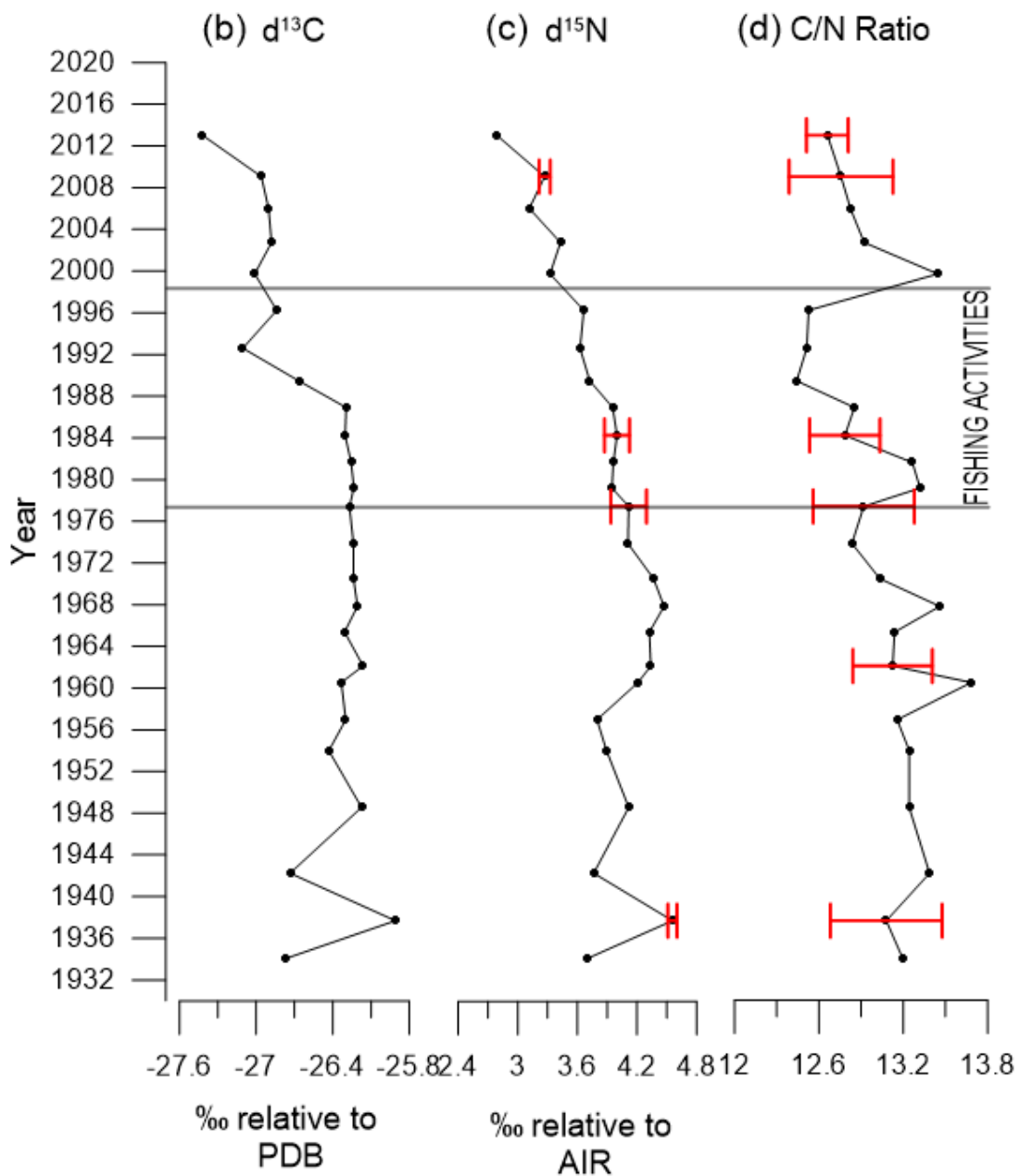


Fig. 6-5 Summary plot of the analytic analysis of ^{13}C , ^{15}N and C:N ratio for the top 20 cm of L. Llaviucu. Data from Fig. 5-24. Red error bars are standard deviations calculated from triplicates. No error data is available for $\delta^{13}\text{C}$.

The depletion of $\delta^{13}\text{C}$ over a short time (approx. 4 years) may point to an increased input of C3 plants. Vascular plants discriminate against ^{13}C so the organic matter produced has isotopic values of -32 to -25‰ (Meyers and Ishiwatari, 1993) which are similar to those found in L. Llaviucu. However, phytoplankton also discriminates against ^{13}C and fractionate dissolved inorganic carbon by $\sim -20\text{‰}$ so are likewise expected to show depleted values (-28.8 to -6.8‰) (Meyers 1994; Torres et al. 2012). The similarity in $\delta^{13}\text{C}$ values makes the discrimination using carbon isotopes alone, impossible (Cohen, 2003). Nitrogen isotopic values can be explored instead as C3 plants typically show values of +1‰ while phytoplankton generally ranges from +2 to +14‰ (Cohen, 2003). The input of both C3 and increased phytoplankton would thus decrease $\delta^{13}\text{C}$ values over time but increase the $\delta^{15}\text{N}$ signal which is not seen to be the case. Similarly, increased input from soil erosion which in terms of $\delta^{13}\text{C}$ is similar to both C3 plants and phytoplankton (-26 to -24‰) does have a high $\delta^{15}\text{N}$ signature (+5‰) (Cohen, 2003). Yet, the C:N ratio does show periodically small increases in values which may indicate a higher input of C3 plants (Brenner et al., 1999). Consequently, the input of C3 plants and soil or an increase in phytoplankton cannot be disentangled, but they all may be influencing the record. However, the gradual $\delta^{15}\text{N}$ depletion must be the result of another process which masks the enrichment that increasing C3 and phytoplankton would produce.

The introduction of Rainbow trout into L. Llaviucu is hypothesised to have had an effect on the environment of the lake. The results of $\delta^{15}\text{N}$, $\delta^{13}\text{C}$ and C:N ratio show a decreasing trend. However, these do not coincide with the time of the fisheries activity, at least on a first approach, even when considering the dating uncertainty. The ratio of C:N and $\delta^{15}\text{N}$ begin their decline in 1960s while $\delta^{13}\text{C}$ changes abruptly in the late 1980s. However, it is likely that the fishing began on a small scale as was discussed in section 2.7.1. Although the fishing might not have influenced the C:N and $\delta^{15}\text{N}$ record, it is very likely that it did cause the abrupt $\delta^{13}\text{C}$ change. It is possible that the lake buffered the fish pollution due to its very fast reservoir turnover of 17 days (Barros and Carrasco 2006) until a threshold was reached in the 1990s. This coincides with the moment ETAPA (Empresa de Telecomunicaciones, Agua Potable, Alcantarillado y saneamiento de Cuenca) declared a deterioration of the water quality in the lake (Barros and Carrasco 2006).

With increasing trophic state, an enrichment of both $\delta^{13}\text{C}$ and $\delta^{15}\text{N}$ is expected (Torres et al., 2012; Vander Zanden and Fetzner, 2007). This is the opposite of the Llaviucu results. However, farm fish are usually fed pellets highly depleted in $\delta^{13}\text{C}$ (-21.53 to -21.1‰; Mazzola and Sara, 2001; Ye et al. 1991), but enriched in $\delta^{15}\text{N}$ (+6.5 to +10.7‰; Sarà et al. 2004). Vizzini and Mazzola (2004) have shown that organisms often take the isotopic signature of their food. As a result, fish faeces are also depleted in $\delta^{13}\text{C}$ (-23.3 to -20.48‰; Mazzola and Sara 2001; Ye et al. 1991) and enriched in $\delta^{15}\text{N}$ (+10.7‰; Sarà et al. 2004). However, the sediment ^{13}C values from Llaviucu are significantly more depleted than these references. Vizzini and Mazzola (2004) have also shown that $\delta^{15}\text{N}$ is more enriched closer to the impact locations. This example may indicate that the Llaviucu sediment core might have been retrieved away from the cages' original locations. This observation, in combination with the lack of $\delta^{15}\text{N}$ enrichment, indicates that the fish farming influenced the $\delta^{13}\text{C}$ values abruptly once the lake passed a threshold, but other processes are also at play. Nitrogen isotopes gradually depleted contrary to expectations. Furthermore, $\delta^{13}\text{C}$ values have continued to decline although the fishing has ceased. If anthropogenic activities were solely influencing the record, low $\delta^{13}\text{C}$ and high $\delta^{15}\text{N}$ would be recorded (Torres et al., 2012).

This gradual depletion in $\delta^{15}\text{N}$ may be the result of a relative increase in N-fixing bacteria such as cyanobacteria. The gradual decline in C:N ratio suggests increasing input from algae relative to higher plants (Brenner et al., 1999). If phosphorous, which was not measured here, was also increasing, there may have been persistent N-limitation favouring N-fixing cyanobacteria which relies on atmospheric N_2 ($\delta^{15}\text{N} = 0\text{‰}$) (Brenner et al., 1999; Torres et al., 2012). The greater relative contribution of depleted $\delta^{15}\text{N}$ would be reflected as a general increase in trophic state according to Brenner et al. (1999). However, high N-availability in the water column can also favour autochthonous organic matter low in $\delta^{15}\text{N}$ as high N concentrations allow greater discrimination by algae against $\delta^{15}\text{N}$ (Torres et al., 2012). A switch to cyanobacteria-dominated phytoplankton may be reflected in the diatom study by Michelutti et al. (2015), which showed decreasing concentrations of many species since the 1970s. However, as the $\delta^{13}\text{C}$ signature of cyanobacteria is also similar to that of the soil, organic matter and C3 plants (-27.7 to -21.6‰) (Gu et al., 1996), it is once again difficult to ascertain this claim.

The particularly depleted $\delta^{13}\text{C}$ values might have been influenced by an amplification of thermal stratification with climate change. Increased anoxia in the bottom water would lead to anaerobic decomposition of the already depleted ^{13}C (Torres et al., 2012). In a temperate stratified lake, strong differences develop between the epilimnion (where production increases due to algal blooms) and the hypolimnion (where respiration dominates). Settling of organic matter dissolves in the hypolimnion releasing ^{12}C into the dissolved inorganic carbon pool producing $\delta^{13}\text{C}$ depleted values (Cohen, 2003). Similar profiles are seen in Lake Annie in Florida where C:N, $\delta^{15}\text{N}$ and $\delta^{13}\text{C}$ are decreasing with time (Torres et al., 2012). This change was related to the thermocline moving to shallower depths. In turn this would increase the volume of anoxic bottom water leading to anaerobic decomposition of already depleted $\delta^{13}\text{C}$ suspended organic matter. Thevenon et al. (2012) also indicate longer and stronger lake stratification may influence the $\delta^{15}\text{N}$ for the same reasons as for $\delta^{13}\text{C}$. With climate change, CNP lakes have become increasingly stratified (Michelutti et al., 2016). Michelutti et al. (2016) showed protracted periods of thermal stratification have become the norm. L. Llaviucu has especially been recording the highest surface temperatures with fewer isothermal conditions of all the other lakes studies. This stratification is also visible from the diatom study by Michelutti et al. (2015), which showed a drastic increase in *Discotella stelligera* starting in the 1960s. This increase reflects a physical restructuring of the water column. The authors hypothesized that with climate change and enhanced thermal stability, upwelling of bottom nutrients become curtailed thus influencing the trophic state towards oligotrophy. This has been demonstrated in an African rift lake (Tierney et al., 2010). However, the relatively small changes in $\delta^{13}\text{C}$ may also be explained by the Suess effect, which should be corrected in lakes according to Verburg (2007). In conclusion, although a trend towards a more oligotrophic state would need further investigation, the unexpectedly depleted $\delta^{13}\text{C}$ values do coincide with stronger thermal stratification.

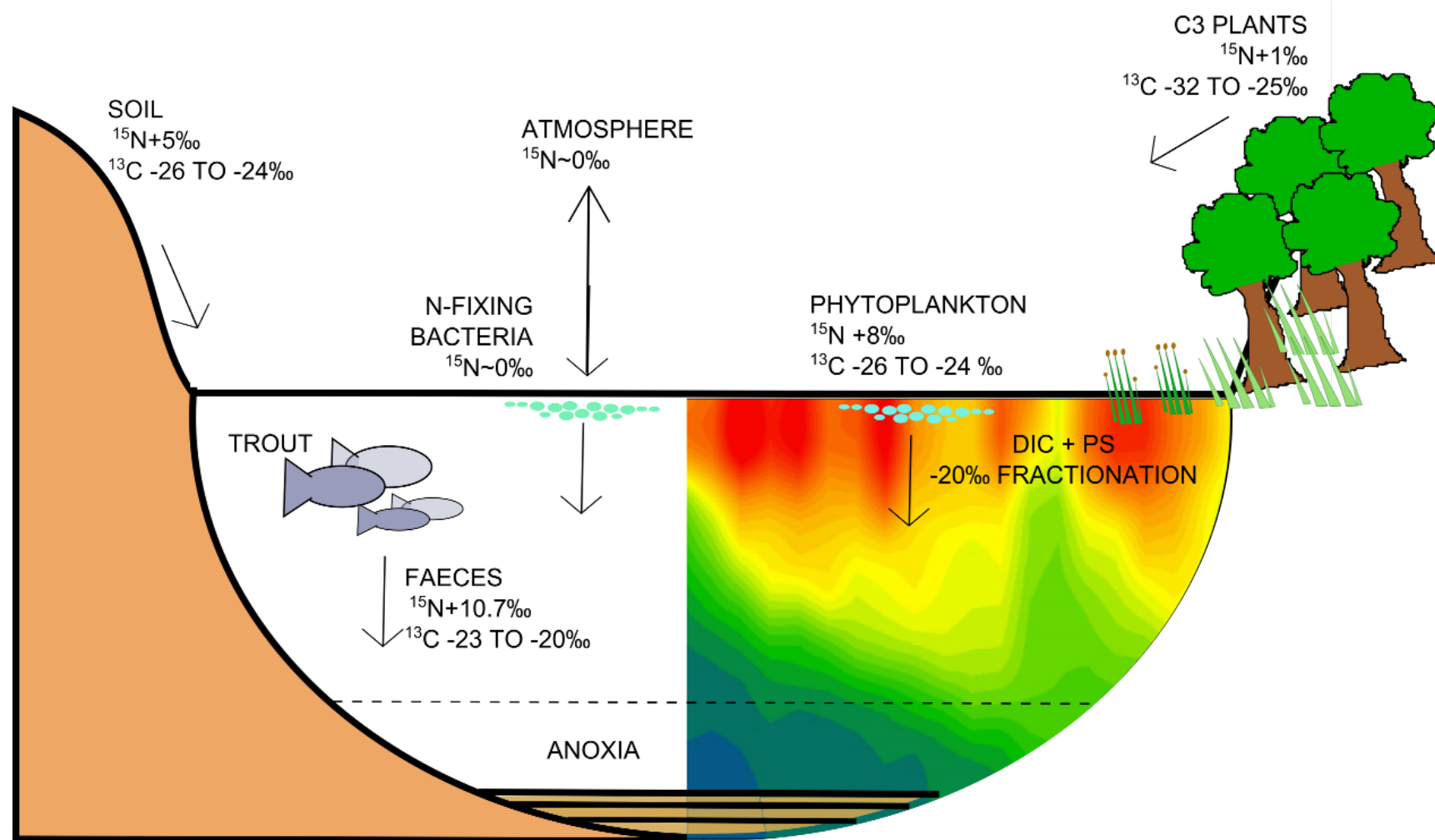


Fig. 6-6 Schematic of the different processes affecting the isotopic signal of the lake sediments of L. Llaviucu. PS stands for photosynthesis. Isotopic values are taken from the following papers: Cohen (2003); Heaton (1986); Meyers and Ishiwatari (1993). Temperature profile was taken from Michelutti et al. (2016).

7 Conclusions

7.1 Summary

The goals of this thesis were varied. The first part was to classify flood layers in the L. Llaviucu sediment core and to combine the results with an age depth model to produce a flood reconstruction. It was expected that the hyperspectral imaging would discriminate the different sediment types (tephra, background, organic and clastic) and a spectral map could be produced. X-ray fluorescence data was also investigated. Both methods yielded promising results that if more time was available could be fine-tuned. However, some limitations were encountered such as the wetness and darkness of the sediment which made the discrimination by hyperspectral imaging challenging. XRF data was also of limited use as tephra also showed similar signals as the flood layers. Finally, visual identification was most successful and a reconstruction was combined with the age-depth model.

In a second part, the thesis looked at conceptualizing a new cleaning procedure for bulk tephra samples. It was expected that a step density removal technique combined with a procedure to remove clay would improve the method. The expectation was that bulk samples would be faster to analyse than single grains (considering the extremely small size of the particles) and that a pure signal could be measured by ICP-MS. However, it became quickly apparent that the final samples were never truly purified. It also became clear that the volcanic bedrock surrounding the lakes was producing xenoliths of similar composition masking the geochemical signal from the tephra. A further issue stemmed from the tephra type which, as andesitic material, is prone to weathering and usually mineral-rich. In a further step, the project aimed to use multiple datasets of morphology, geochemistry and colour combined with statistical procedures to correlate the tephra layers. It was expected that at least one tephrochronomarker could be found with high certainty as the characteristics of the layers would be significantly different. It was further expected that age brackets would be assignable to the layers producing a tephrochronology for south central Ecuador. However, it also became apparent that the mixed geochemical signal, the weathered tephra particles and the large age uncertainties made the correlation challenging. The combination of many datasets and statistical procedure enabled two markers to be identified, however not to the certainty anticipated. It was further expected that L. Llaviucu located in a vegetated area would be easily dated using macrofossils. However, it was challenging to find usable plant material of sufficient carbon weight. In the end, small fossils were dated which meant larger age uncertainties. Finally, it was hoped that original eruptions would be found for these tephrochronomarkers. However, due to the limitations in the measurement of the tephra in this study, due to the scarcity of available data for comparison and due to the lack of a unique signal, provenance investigation was not successful within the timeframe available for this study.

The third and final aspect of the thesis aimed at tracing the effects of the fish hatchery in L. Llaviucu through the use of stable isotopes ^{15}N and ^{13}C as well as elemental carbon and nitrogen. It was expected that the sediment would be depleted in ^{15}N as the hypothesis was that the fish were fed marine fish with a depleted signal. The ^{15}N record does show a decrease but based on the literature, farm fish are fed pellets which are actually enriched in ^{15}N . In addition, the visible depletion in the record begins prior to the fish activity, even when

considering the age uncertainty. It was further expected that the sediment record would show when the lake returned to “normal” after the fishing stopped. However, lake geochemical properties appeared to have passed a threshold and never recovered as the ^{15}N signal continued to decline. In fact all proxies exhibited a continued change after the activities ceased. As a result, whether the changes were due to the fishing is disputable and may be the consequence of other processes. A further interest was to investigate other analytical results from ^{13}C and the C:N ratio. The records revealed complex changes happening in the lake which speak of climate and environmental change. However, not enough data is available to separate the different influences.

7.2 Concluding remarks

This project attempted to produce a flood frequency reconstruction and tephrochronology of the late Holocene as well as investigate the climate and environmental processes which may have affected the lake over the last century. In the first instance, age-depth models offer the opportunity to date lake sediment records but some aspects may be kept in mind. Firstly, comparing several ^{210}Pb models provides a better estimate of the age of young sediment. Furthermore, missing inventory adjustments are necessary to correct for the tailing effect. Moreover, dating bulk and microfossils gives an estimate of the reservoir effect while dating very small microfossils is still a useful endeavour even if the age uncertainty is wide as this gives an indication of a possible time range. Finally, flood layer corrected age-depth models provide more credible profiles.

Secondly, the classification and reconstruction of a flood frequency by scanning methods show promising aspects but requires some fine-tuning. This study showed that the hyperspectral technique can discriminate between types of sediment but is affected by mixed signals. In the future, research should be directed towards finding a more sensitive method to discriminate between the spectra which are similar but relate to different sediment types. Visual and near infrared spectroscopy are also useful to identify the beginning of human impact. Furthermore, this study showed that a flood reconstruction can be produced with adequate certainty using multiple lines of evidence. Multiple lines of evidence are also necessary to disentangle the different processes occurring in the lake as also concluded from the results of the wet chemical analysis. From a limnological point of view, the use of multiple parallel cores demonstrated that deposition is not uniform throughout the lake basin.

Heterogeneous basin deposition was also identified from the attempts at producing a tephrochronology. Furthermore, this section of the study demonstrated that identifying andesitic cryptotephra is challenging due to their very nature. Scanning methods such as XRF and MS are useful but not exhaustive and visual identification remains the best tool. Moreover, it was shown that purifying bulk samples is challenging particularly when dealing with tephra characteristics which are not ideal i.e. weathering-prone and mineral rich. However, a wide range of elements (major, minor and trace) provide substantial data from which to make comparisons and testing many datasets with many statistical procedures is necessary when the data shows conflicting results. In conclusion, tephrochronomarkers should be based on all available data but age and stratigraphy are most important because other datasets may not be the most representative.

7.3 Research importance

The importance of this study is manifold. This study was the first identification and dating of two late Holocene tephrochronomarkers using a wide range of datasets and statistical procedures. It demonstrated the first flood classification attempt using hyperspectral imaging. It also produced the first flood frequency reconstruction from L. Llaviucu which can now be used to compare the results from Rodbell et al. (1999). This project confirmed that even after thorough cleaning using an improved method, bulk tephra analysis remains challenging. It showed that low carbon macrofossil dating can still be useful and demonstrated that missing inventory corrections are necessary and so is the comparison of different ^{210}Pb models. This project once again showed that hyperspectral imaging can identify the start of human impact. Finally, the results clearly showed that multiproxy analyses are necessary to attribute any changes in the records.

7.4 Recommendations for future research

A few recommendations can be made from the present study:

- If time permits, single grain analysis should be used to produce a tephrochronology even if the grains are small.
- Cluster analysis with fewer cluster numbers should be attempted, especially if some of the tephra layers are actually flood layers.
- Replicates should always be made when possible.
- Process studies to understand the functioning of a lake are paramount as this helps with the interpretation of the proxies.
- The investigation of flood layers should follow a structured procedure as exemplified in Schillereff et al. (2014).
- Measuring tape should be placed along the side of sediment cores to avoid measuring errors.
- Parallel cores are fundamental to understand the complete story as deposition is often uneven.
- Hyperspectral classification of flood layers should be investigated further, especially the sensitivity of the statistical procedures used to discriminate the layers.

Lake sediment is a promising but complex archive of the past. Lakes are influenced by a multitude of processes which are challenging to disentangle. Multiple proxy analyses on multiple parallel cores dated through multiple techniques provide the sole possibility to investigate these processes.

8 References

- Adrian, R., Reilly, C.M.O., Zagarese, H., Baines, S.B., Dag, O., 2010. Lakes as sentinels of climate change. *Limnol. Ocean.* 54, 2283–2297.
- Allbrook, R.F., 1985. The effect of allophane on soil properties. *Appl. Clay Sci.* 1, 65–69.
- Alloway, B. V, Lowe, D.J., Larsen, G., Shane, P.A.R., Westgate, J.A., 2013. Tephrochronology. *Encycl. Quat. Sci.* 277–304.
- Appleby, P.G., 2008. Three decades of dating recent sediments by fallout radionuclides: a review. *The Holocene* 18, 83–93.
- Appleby, P.G., 1998. Dating recent sediments by Pb-210: Problems and solutions. *Proc. 2nd NKS/EKO-1 Semin. Helsinki, 2-4 April 1997, STUK, Helsinki* 7–24.
- Appleby, P.G., Oldfield, F., 1978. The calculation of lead-210 dates assuming a constant rate of supply of unsupported 210Pb to the sediment. *Catena* 5, 1–8.
- Arculus, R.J., Gill, J.B., Cambray, H., Chen, W., Stern, R.J., 1995. Geochemical evolution of arc systems in the western Pacific; the ash and turbidite record recovered by drilling. *Active Margins and Marginal Basins of the Western Pacific Geophysical Monographs* 88, 45–65.
- Arcusa, S., Pinninghoff, J.P.A., Saunders, K.M., Hernandez-Almeida, I., Grosjean, M., 2015. Determining human impact on the environment from lake sediment cores using scanning reflectance spectroscopy: two case studies from Chile and the sub-Antarctic. [Poster] 16th Swiss Global Change Day. Bern.
- Asadzadeh, S., de Souza Filho, C.R., 2016. A review on spectral processing methods for geological remote sensing. *Int. J. Appl. Earth Obs. Geoinf.* 47, 69–90.
- Austin, J.A., Colman, S.M., 2007. Lake Superior summer water temperatures are increasing more rapidly than regional temperatures: A positive ice-albedo feedback. *Geophys. Res. Lett.* 34, 1–5.
- Barberi, F., Coltelli, M., Ferrara, G., Innocenti, F., Navarro, J.M., Santacroce, R., 1988. Plio-Quaternary volcanism in Ecuador. *Geol. Mag.* 125, 1–14.
- Barros, S., Carrasco, M.C., 2006. Estudio limnológico en la laguna de Surocucho (cuenca hidrográfica del Río Llaviuco. Cuenca. Unpublished.
- Basile, I., Petit, J.R., Touron, S., Grousset, F.E., Barkov, N., 2001. Volcanic layers in Antarctic (Vostok) ice cores: Source identification and atmospheric implications. *J. Geophys. Res.* 106, 31, 915–931.
- Bastardo, H., 1994. Reproduction and average size at maturity of the trout *Oncorhynchus mykiss* (Salmoniformes: Salmonidae) in the Venezuelan Andes. *Rev. Biol. Trop.* 42, 263–270.
- Battarbee, R.W., 1999. The importance of palaeolimnology to lake restoration. *Hydrobiologia* 395/396, 149–159.
- Beck, E., Kottke, I., Bendix, J., Makeschin, F., Mosandl, R., 2008. Gradients in a tropical mountain ecosystem of Ecuador - a Synthesis. *Ecol. Stud.* 28, 451–463.

- Bellinger, E.G., Sigee, D.C., 2010. *Freshwater Algae: Identification and Use as Bioindicators*. Wiley-Blackwell, Chichester, UK.
- Bertrand, S., Castiaux, J., Juvigné, E., 2008. Tephrostratigraphy of the Late Glacial and Holocene sediments of Puyehue Lake (Southern Volcanic Zone, Chile, 40°S). *Quat. Res.* 70, 343–357.
- Bias, S., Bonadonna, C., 2013. A fast GIS-based risk assessment for tephra fallout: the example of Cotopaxi volcano, Ecuador Part I: probabilistic hazard assessment. *Nat. Hazards* 65, 477–495.
- Bicknell, A.W.J., Campbell, M., Knight, M.E., Bilton, D.T., Newton, J., Votier, S.C., 2011. Effects of formalin preservation on stable carbon and nitrogen isotope signatures in Calanoid copepods: implications for the use of Continuous Plankton Recorder Survey samples in stable isotope analyses. *Rapid Commun. Mass Spectrom.* 25, 1794–1800.
- Binford, M.W., 1990. Calculation and uncertainty analysis of Pb210 dates for PIRLA project lake sediment cores. *J. Paleolimnol.* 3, 253–267.
- Birks, H., Last, W., Smol, J., 2001. *Tracking Environmental Change Using Lake Sediments*. Kluwer Academic Publishers, Dordrecht.
- Blaauw, M., 2010. Methods and code for “classical” age-modelling of radiocarbon sequences. *Quat. Geochronol.* 5, 512–518.
- Blaauw, M., Christen, J.A., 2011. Flexible paleoclimate age-depth models using an autoregressive gamma process. *Bayesian Anal.* 6, 457–474.
- Blaauw, M., Christen, J.A., 2005. Radiocarbon peat chronologies and environmental change. *J. R. Stat. Soc. Ser. C Appl. Stat.* 54, 805–816.
- Blockley, S.P.E., Pyne-O’donnell, S.D.F., Lowe, J.J., Matthews, I.P., Stone, A., Pollard, A.M., Turney, C.S.M., Molyneux, E.G., 2005. A new and less destructive laboratory procedure for the physical separation of distal glass tephra shards from sediments. *Quat. Sci. Rev.* 24, 1952–1960.
- Bondad-Reantaso, M.G., 2007. *Assessment of freshwater fish seed resources for sustainable aquaculture*, FAO Fisheries Technical Paper. Food and Agriculture Organization of the United Nations, Rome.
- Borchardt, G.A., Aruscavage, P.J., Millard, H.T., 1972. Correlation of the Bishop Ash, a Pleistocene marker bed, using instrumental neutron activation analysis. *J. Sediment. Res.* 42, 301–306.
- Boyle, J., 1999. Variability of tephra in lake and catchment sediments, Svínavatn, Iceland. *Glob. Planet. Change* 21, 129–149.
- Brendryen, J., Haflidason, H., Sejrup, H.P., 2010. Norwegian Sea tephrostratigraphy of marine isotope stages 4 and 5: Prospects and problems for tephrochronology in the North Atlantic region. *Quat. Sci. Rev.* 29, 847–864.
- Brenner, M., Whitmore, T.J., Curtis, J.H., Hodell, D. A, Schelske, C.L., 1999. Stable isotope ($\delta^{13}\text{C}$ and $\delta^{15}\text{N}$) signature of sedimented organic matter as indicators of historic lake trophic state. *J. Paleolimnol.* 22, 205–211.
- Briggs, P.H., Meier, A.L., 2002. *The determination of forty-two elements in geological materials by inductively coupled plasma – mass spectrometry*. Analytical methods for chemical analysis of geologic and other materials. U.S. Geological Survey Open File Report 02-223-I.
- Brown, S.K., Sparks, R.S.J., Mee, K., Ilyinskaya, E., Jenkins, S.F., Loughlin, S.C., 2015. Appendix B –

- Region 15 Country and regional profiles of volcanic hazard and risk : South America Region 15 : South America, in: Loughlin, S.C., Sparks, R.S.J., Brown, S.K., Jenkins, S.F., Vye-Brown, C. (Eds.), *Global Volcanic Hazards and Risk*. Cambridge University Press, Cambridge.
- Brunschön, C., Behling, H., 2009. Late Quaternary vegetation, fire and climate history reconstructed from two cores at Cerro Toledo, Podocarpus National Park, southeastern Ecuadorian Andes. *Quat. Res.* 72, 388–399.
- Bryant, C.J., Arculus, R.J., Eggins, S.M., 1999. Laser ablation inductively coupled plasma mass spectrometry and tephras: A new approach to understanding arc-magma genesis. *Geology* 27, 1119–1122.
- Butz, C., 2016. The Specim hyperspectral single core scanner: User manual. PhD Thesis. University of Bern.
- Butz, C., Grosjean, M., Fischer, D., Wunderle, S., Tylmann, W., Rein, B., 2015. Hyperspectral imaging spectroscopy: a promising method for the biogeochemical analysis of lake sediments. *J. Appl. Remote Sens.* 9, 20.
- Buytaert, W., Deckers, J., Wyseure, G., 2007. Regional variability of volcanic ash soils in south Ecuador: The relation with parent material, climate and land use. *Catena* 70, 143–154.
- Buytaert, W., Deckers, J., Wyseure, G., 2006. Description and classification of nonallophanic Andosols in south Ecuadorian alpine grasslands (páramo). *Geomorphology* 73, 207–221.
- Carabel, S., Verísimo, P., Freire, J., 2009. Effects of preservatives on stable isotope analyses of four marine species. *Estuar. Coast. Shelf Sci.* 82, 348–350.
- Carroll, J., Abraham, J., 1996. Sediment isotope tomography (SIT) model version 1. Master Thesis. DOE/Grand Junction Project Office.
- Caseldine, C., Baker, A., Barnes, W.L., 1999. A rapid, non-destructive scanning method for detecting distal tephra layers in peats. *The Holocene* 9, 635–638.
- Cohen, A.S., 2003. *Paleolimnology: The History and Evolution of Lake Systems*. Oxford University Press, New York.
- Colinvaux, P.A., Bush, M.B., Steinitz-Kannan, M., Miller, M.C., 1997. Glacial and Postglacial Pollen Records from the Ecuadorian Andes and Amazon. *Quat. Res.* 48, 69–78.
- Comunidad Andina, 2009. *Atlas de las dinámicas del territorio Andino: Población Bienes expuestos a amenazas naturales*.
- Conroy, J.L., Overpeck, J.T., Cole, J.E., Shanahan, T.M., Steinitz-Kannan, M., 2008. Holocene changes in eastern tropical Pacific climate inferred from a Galápagos lake sediment record. *Quat. Sci. Rev.* 27, 1166–1180. doi:10.1016/j.quascirev.2008.02.015
- Croweller, H.S., Sparks, R.S.J., Sieber, J.R., 2009. Volcano Global Risk Identification and Analysis Project (VOGRIPA) [WWW Document]. URL <http://www.bgs.ac.uk/vogripa/>
- Croudace, I.W., Rothwell, R.G., 2015. Future Developments and Innovations in High-Resolution Core Scanning, in: *Micro-XRF Studies of Sediment Cores*.
- D’Anjou, R.M., Balascio, N.L., Bradley, R.S., 2014. Locating cryptotephra in lake sediments using fluid imaging technology. *J. Paleolimnol.* 52, 257–264.
- Daga, R., Guevara, S.R., Poire, D.G., Arribére, M., 2014. Characterization of tephras dispersed by the recent eruptions of volcanoes Calbuco (1961), Chaitén (2008) and Cordon Caulle

- Complex (1960 and 2011), in Northern Patagonia. *J. South Am. Earth Sci.* 49, 1–14.
- Daga, R., Guevara, S.R., Sánchez, M.L., Arribére, M., 2010. Tephrochronology of recent events in the Andean Range (northern Patagonia): Spatial distribution and provenance of lacustrine ash layers in the Nahuel Huapi National Park. *J. Quat. Sci.* 25, 1113–1123.
- Davies, S.J., Lamb, H.F., Roberts, S.J., 2015. Micro-XRF Core Scanning in Palaeolimnology: Recent Developments, in: *Micro-XRF Studies of Sediment Cores*. Springer Netherlands, Dordrecht 189–226.
- Davies, S.M., 2015. Cryptotephra: the revolution in correlation and precision dating; Cryptotephra: the revolution in correlation and precision dating. *J. Quat. Sci.* 30, 114–130.
- de Fontaine, C.S., Kaufman, D.S., Scott Anderson, R., Werner, A., Waythomas, C.F., Brown, T. a., 2007. Late Quaternary distal tephra-fall deposits in lacustrine sediments, Kenai Peninsula, Alaska. *Quat. Res.* 68, 64–78.
- De Jong, R., Von Gunten, L., Maldonado, A., Grosjean, M., 2013. Late Holocene summer temperatures in the central Andes reconstructed from the sediments of high-elevation Laguna Chepical, Chile (32°S). *Clim. Past* 9, 1921–1932.
- Dearing, J.A., Battarbee, A.R.W., Dikau, A.R., Larocque, I., Oldfield, A.F., 2006. Human–environment interactions: learning from the past. *Reg. Env. Change* 6, 1–16.
- Dugmore, A.J., Newton, A.J., 1995. Seven tephra isochrones in Scotland. *The Holocene* 5, 257–266.
- Eastwood, W.J., Pearce, N.J.G., Westgate, J.A., Perkins, W.T., Lamb, H.F., Roberts, N., 1999. Geochemistry of Santorini tephra in lake sediments from Southwest Turkey. *Glob. Planet. Change* 21, 17–29.
- ECOLAP, MAE, 2007. *Guía del Patrimonio de Áreas Naturales Protegidas del Ecuador*. Quito.
- Eden, D.N., Froggatt, P.C., McIntosh, P.D., 1992. The distribution and composition of volcanic glass in late Quaternary loess deposits of southern South Island, New Zealand, and some possible correlations. *New Zealand J. Geol. Geophys.* 35, 69–79.
- Elbert, J., Wartenburger, R., Von Gunten, L., Urrutia, R., Fischer, D., Fujak, M., Hamann, Y., Greber, N.D., Grosjean, M., 2013. Late Holocene air temperature variability reconstructed from the sediments of Laguna Escondida, Patagonia, Chile (45°30'S). *Palaeogeogr. Palaeoclimatol. Palaeoecol.* 369, 482–492.
- Emck, P., 2007. *A Climatology of South Ecuador With special focus on the Major Andean Ridge as Atlantic-Pacific Climate Divide*. PhD Thesis. Friedrich-Alexander-Universität Erlangen-Nürnberg.
- Fontijn, K., Lachowycz, S.M., Rawson, H., Pyle, D.M., Mather, T.A., Naranjo, J.A., Moreno-Roa, H., 2014. Late Quaternary tephrostratigraphy of southern Chile and Argentina. *Quat. Sci. Rev.* 89, 70–84.
- French, N.R., 1960. Strontium-90 in Ecuador. *Science* 131, 1889–1890.
- Froese, R., Pauly, D., 2016. FishBase [WWW Document]. URL www.fishbase.org
- Garrison, J.M., Davidson, J.P., Hall, M., Mothes, P., 2011. Geochemistry and petrology of the most recent deposits from Cotopaxi Volcano, Northern Volcanic Zone, Ecuador. *J. Petrol.* 52, 1641–1678.

- Gehrels, M.J., Newnham, R.M., Lowe, D.J., Wynne, S., Hazell, Z., Caseldine, C., 2008. Towards rapid assay of cryptotephra in peat cores: Review and evaluation of various methods. *Quat. Int.* 178, 68–84.
- Gilli, A., Anselmetti, F.S., Glur, L., Wirth, S.B., 2013. Lake Sediments as Archives of Recurrence Rates and Intensities of Past Flood Events, in: Schneuwly-Bollscheweiler, M. (Ed.), *Dating Torrential Processes on Fans and Cones*. Springer Science+Business Media, Dordrecht, 225–242.
- Goddard, L., Dilley, M., 2005. El Niño: Catastrophe or Opportunity. *Am. Meteorol. Soc.* 18, 651–665.
- Goodman, A.Y., 1996. *Glacial Geology and Soil Catena Development on Moraines in Las Cajas National Park, Ecuador*. Union College, Schenectady, NY.
- Grosjean, M., Amann, B., Butz, C., Rein, B., Tylmann, W., 2014. Hyperspectral imaging: a novel non destructive method for investigating sub-annual sediment structures and composition. *PAGES Mag.* 22, 10–11.
- Gu, B., Schelske, C.L., Brenner, M., 1996. Relationship between sediment and plankton isotope ratios ($\delta^{13}\text{C}$ and $\delta^{15}\text{N}$) and primary productivity in Florida lakes. *Can. J. Fish. Aquat. Sci.* 53, 875–883.
- Guyard, H., Chapron, E., St-Onge, G., Anselmetti, F.S., Arnaud, F., Magand, O., Francus, P., Res, M.-A., 2007. High-altitude varve records of abrupt environmental changes and mining activity over the last 4000 years in the Western French Alps (Lake Bramant, Grandes Rousses Massif). *Quat. Sci. Rev.* 26, 2644–2660.
- Hafliðason, H., Eiríksson, J., Van Kreveld, S., 2000. The tephrochronology of Iceland and the North Atlantic region during the Middle and Late Quaternary: a review. *J. Quat. Sci.* 15, 3–22.
- Hall, M., Mothes, P., 2007. The rhyolitic–andesitic eruptive history of Cotopaxi volcano, Ecuador. *Bull. Volcanol.* 70, 675–702.
- Hall, M.L., Robin, C., Beate, B., Mothes, P., Monzier, M., 1999. Tungurahua Volcano, Ecuador: structure, eruptive history and hazards. *J. Volcanol. Geotherm. Res.* 91, 1–21.
- Hammer, Ø., Harper, D.A.T., Ryan, P.D., 2001. Paleontological statistics software package for education and data analysis. *Palaeontol. Electron.* 4, 9–18.
- Hansen, B.C.S., Rodbell, D.T., Seltzer, G.O., Leon, D.B., Young, K.R., Abbott, M., 2003. Late-glacial and Holocene vegetational history from two sites in the western Cordillera of southwestern Ecuador. *Palaeogeogr. Palaeoclimatol. Palaeoecol.* 194, 79–108.
- Hatté, C., Jull, A.J.T., 2013. ^{14}C of Plant Macrofossils. *Encycl. Quat. Sci.* (Second Ed.) 361–367.
- Hayward, C., 2012. High spatial resolution electron probe microanalysis of tephtras and melt inclusions without beam-induced chemical modification. *The Holocene* 22, 119–125.
- Heaton, T.H.E., 1986. Isotopic Studies of Nitrogen Pollution in the Hydrosphere and Atmosphere : a Review. *Chem. Geol.* 59, 87–102.
- Hopkins, J.L., Millet, M.-A., Timm, C., Wilson, C.J.N., Leonard, G.S., Palin, J.M., Neil, H., 2015. Tools and techniques for developing tephra stratigraphies in lake cores: A case study from the basaltic Auckland Volcanic Field, New Zealand. *Quat. Sci. Rev.* 123, 58–75.
- Jain, A.K., 2010. Data clustering: 50 years beyond K-means. *Pattern Recognit. Lett.* 31, 651–666.

- Kaehler, S., Pakhomov, E.A., 2001. Effects of storage and preservation on the ^{13}C and ^{15}N signatures of selected marine organisms. *Mar. Ecol. Prog. Ser.* 219, 299–304.
- Kämpf, L., Brauer, A., Dulski, P., Lami, A., Marchetto, A., Gerli, S., Ambrosetti, W., Guilizzoni, P., 2012. Detrital layers marking flood events in recent sediments of Lago Maggiore (N. Italy) and their comparison with instrumental data. *Freshw. Biol.* 57, 2076–2090.
- Katoh, S., Nagaoka, S., WoldeGabriel, G., Renne, P., Snow, M.G., Beyene, Y., Suwa, G., 2000. Chronostratigraphy and correlation of the Plio-Pleistocene tephra layers of the Konso Formation, southern Main Ethiopian Rift, Ethiopia. *Quat. Sci. Rev.* 19, 1305–1317.
- Krishnaswamy, S., Lal, D., Martin, J.M., Meybeck, M., 1971. Geochronology of lake sediments. *Earth Planet. Sci. Lett.* 11, 407–414.
- Kuehn, S.C., Foit, F.F., 2006. Correlation of widespread Holocene and Pleistocene tephra layers from Newberry Volcano, Oregon, USA, using glass compositions and numerical analysis. *Quat. Int.* 148, 113–137.
- Kuehn, S.C., Froese, D.G., 2010. Tephra from Ice—A Simple Method to Routinely Mount, Polish, and Quantitatively Analyze Sparse Fine Particles. *Microsc. Microanal.* 1–8.
- Kylander, M.E., Lind, E.M., Wastegard, S., Lowemark, L., 2012. Recommendations for using XRF core scanning as a tool in tephrochronology. *The Holocene* 22, 371–375.
- Ledru, M.-P., Jomelli, V., Samaniego, P., Vuille, M., Hidalgo, S., Herrera, M., Ceron, C., 2013. The Medieval Climate Anomaly and the Little Ice Age in the eastern Ecuadorian Andes. *Clim. Past* 9, 307–321.
- Libby, W.F., Anderson, E.C., Arnold, J.R., 1949. Age Determination by Radiocarbon Content: World-Wide Assay of Natural Radiocarbon. *Science* 109, 227–228.
- Lim, C., Ikehara, K., Toyoda, K., 2008. Cryptotephra detection using high-resolution trace-element analysis of Holocene marine sediments, southwest Japan. *Geochim. Cosmochim. Acta* 72, 5022–5036.
- Liu, E.J., Oliva, M., Antoniadis, D., Giralt, S., Granados, I., Pla-Rabes, S., Toro, M., Geyer, A., 2015. Expanding the tephrostratigraphical framework for the South Shetland Islands, Antarctica, by combining compositional and textural tephra characterisation. *Sediment. Geol.* in press.
- Livingstone, D.M., 2003. Thermal Structure of a Large Temperate Central European Lake. *Clim. Change* 57, 205–225.
- Lowe, D.J., 2011. Tephrochronology and its application: A review. *Quat. Geochronol.* 6, 107–153.
- Lowe, D.J., 2008. Globalization of tephrochronology: new views from Australasia. *Prog. Phys. Geogr.* 32, 311–335.
- Lowe, D.J., Shane, P.A.R., Alloway, B. V., Newnham, R.M., 2008. Fingerprints and age models for widespread New Zealand tephra marker beds erupted since 30,000 years ago: a framework for NZ-INTIMATE. *Quat. Sci. Rev.* 27, 95–126.
- Mackay, H., Hughes, P.D.M., Jensen, J.L., Langdon, P.G., Donnell, S.D.F.P.-O., Plunkett, G., Froese, D.G., Coulter, S., Gardner, J.E., 2016. A mid to late Holocene cryptotephra framework from eastern North America Introduction. *Quat. Sci. Rev.* 132, 101–113.
- MacKenzie, A.B., Hardie, S.M.L., Farmer, J.G., Eades, L.J., Pulford, I.D., 2011. Analytical and sampling constraints in ^{210}Pb dating. *Sci. Total Environ.* 409, 1298–1304.

- Mackie, E.A., Davies, S.M., Turney, C.S., Dobbyn, K., Lowe, J.J., Hillt, P.G., 2002. The use of magnetic separation techniques to detect basaltic microtephra in last glacial-interglacial transition (LGIT; 15-10 ka cal. BP) sediment sequences in Scotland. *Scottish J. Geol.* 38, 21–30.
- Mazzola, A., Sara, G., 2001. The Effects of Fish Farming Organic Waste on Food Availability for Bivalve Molluscs: Stable Isotope Analysis. *Aquaculture* 192, 361–379.
- McCormac, F.G., Hogg, A.G., Blackwell, P.G., Buck, C., Higham, T.F.G., Reimer, P.J., 2004. SHCAL04 Southern Hemisphere Calibration, 0–11.0 cal kyr BP. *Radiocarbon* 46, 1084–1092.
- Meyers, P.A., 1994. Preservation of elemental and isotopic source identification of sedimentary organic matter. *Chem. Geol.* 114, 289–302.
- Meyers, P.A., Ishiwatari, R., 1993. Lacustrine organic geochemistry—an overview of indicators of organic matter sources and diagenesis in lake sediments. *Org. Geochem.* 20, 867–900.
- Michelutti, N., Labaj, A., Grooms, C., Smol, J., 2016. Equatorial mountain lakes show extended periods of thermal stratification with recent climate change. *J. Limnol.* 18, n.a.
- Michelutti, N., Wolfe, A.P., Cooke, C.A., Hobbs, W.O., Vuille, M., Smol, J.P., 2015. Climate Change Forces New Ecological States in Tropical Andean Lakes. *PLoS One* 10, n.a.
- Mix, A.C., Rugh, W., Pisias, N.G., Veirs, S., ShipboardSedimentologists, L. 138, Leg 138, S.P., 1992. Color reflectance spectroscopy: a tool for rapid characterization of deep sea sediments. *Proc. Ocean Drill. Program, Initial Reports*, 138, 67–77.
- Monzier, M., Robin, C., Samaniego, P., Hall, M.L., Cotten, J., Mothes, P., Arnaud, N., 1999. Sangay volcano, Ecuador: structural development, present activity and petrology. *J. Volcanol. Geotherm. Res.* 90, 49–79.
- Morán-Tejeda, E., Bazo, J., López-Moreno, J.I., Aguilar, E., Azorín-Molina, C., Sanchez-Lorenzo, A., Martínez, R., Nieto, J.J., Mejía, R., Martín-Hernández, N., Vicente-Serrano, S.M., 2016. Climate trends and variability in Ecuador (1966-2011). *Int. J. Climatol.* n.a.
- Mothes, P.A., Hall, M.L., 1998. Quilotoa's 800 y BP ash: a valuable stratigraphic marker unit for the integration period., in: Mothes, P. (Ed.), *Actividad Volcánica Y Pueblos Precolombinos En El Ecuador*. Abya-Yala, Quito, 111–138.
- Moy, C.M., Seltzer, G.O., Rodbell, D.T., Anderson, D.M., 2002. Variability of El Niño/ Southern Oscillation activity at millennial timescales during the Holocene epoch. *Nature* 420, 162.
- Nelson, C.S., Froggatt, P.C., Gosson, G.J., 1985. Nature, chemistry, and origin of late Cenozoic megascopic tephra in Leg 90 cores from the southwest Pacific. *Initial reports Deep. Drill. Proj.* 90, 1161–1173.
- Newton, A.J., Dugmore, A.J., Gittings, B.M., 2007. Tephrobase: tephrochronology and the development of a centralised European database. *J. Quat. Sci.* 22, 737–743.
- Ohkouchi, N., Ogawa, N.O., Chikaraishi, Y., Tanaka, H., Wada, E., 2015. Biochemical and physiological bases for the use of carbon and nitrogen isotopes in environmental and ecological studies. *Prog. Earth Planet. Sci.* 2, 1–17.
- Palais, J.M., Kirchner, S., Delmas, R.J., 1990. Identification of some global volcanic horizons by major element analysis of fine ash in antarctic ice. *Ann. Glaciol.* 14, 216–220.
- Pearce, N.J.G., Bendall, C.A., Westgate, J.A., 2008. Comment on “Some numerical considerations in the geochemical analysis of distal microtephra” by A.M. Pollard, S.P.E. Blockley and C.S. Lane. *Appl. Geochemistry* 23, 1353–1364.

- Pearce, N.J.G., Denton, J.S., Perkins, W.T., Westgate, J.A., Alloway, B. V, 2007. Correlation and characterisation of individual glass shards from tephra deposits using trace element laser ablation ICP-MS analyses: current status and future potential. *J. Quat. Sci* 22, 721–736.
- Pearce, N.J.G., Westgate, J.A., Perkins, W.T., Preece, S.J., Harmon, R.S., 2004. The application of ICP-MS methods to tephrochronological problems. *Appl. Geochemistry* 19, 289–322.
- Persson, C., 1971. Tephrochronological investigation of peat deposits in Scandinavia and on the Faroe Islands. Sveriges reproduktions AB.
- Pison, G., Struyf, A., Rousseeuw, P.J., 1999. Displaying a clustering with CLUSPLOT. *Comput. Stat. Data Anal.* 30, 381–392.
- Placzek, C., Quade, J., Rech, J. a., Patchett, P.J., Pérez de Arce, C., 2009. Geochemistry, chronology and stratigraphy of Neogene tuffs of the Central Andean region. *Quat. Geochronol.* 4, 22–36.
- Pollard, A.M., Blockley, S.P.E., Lane, C.S., 2006. Some numerical considerations in the geochemical analysis of distal microtephra. *Appl. Geochemistry* 21, 1692–1714.
- Pollard, A.M., Blockley, S.P.E., Ward, K.R., 2003. Chemical alteration of tephra in the depositional environment: Theoretical stability modelling. *J. Quat. Sci.* 18, 385–394.
- Putyrskaya, V., Klemt, E., Rollin, S., Astner, M., Sahli, H., 2015. Dating of sediments from four Swiss prealpine lakes with ²¹⁰Pb determined by gamma-spectrometry : progress and problems. *J. Environ. Radioact.* 145, 78–94.
- Pyne-O'Donnell, S., 2011. The taphonomy of Last Glacial-Interglacial Transition (LGIT) distal volcanic ash in small Scottish lakes. *Boreas* 40, 131–145.
- Ramsey, C.B., Housley, R.A., Lane, C.S., Smith, V.C., Pollard, A.M., 2015. The RESET tephra database and associated analytical tools. *Quat. Sci. Rev.* 118, 33–47.
- Rea, H.A., Swindles, G.T., Roe, H.M., 2012. The Hekla 1947 tephra in the north of Ireland: regional distribution, concentration and geochemistry. *J. Quat. Sci.* 27, 425–431.
- Reimer, P., Bard, E., Bayliss, A., Beck, J.W., Blackwell, P.G., Bronk Ramsey, C., Buck, C.E., Cheng, H., Edwards, R.L., Friedrich, M., Grootes, P.M., Guilderson, T.P., Haffidason, H., Hajdas, I., Hatté, C., Heaton, T.J., Hoffman, D.L., Hogg, A.G., Hughen, K.A., Kaiser, K.F., Kromer, B., Manning, S.W., Niu, M., Reimer, R.W., Richards, D.A., Scott, E.M., Southon, J.R., Staff, R.A., Turney, C.S.M., van der Plicht, J., 2013. IntCal13 and Marine13 Radiocarbon Age Calibration Curves 0–50,000 Years cal BP. *Radiocarbon* 55, 1869–1887.
- Rein, B., 2007. How do the 1982/83 and 1997/98 El Niños rank in a geological record from Peru? *Quat. Int.* 161, 56–66.
- Rodbell, D.S.T., Seltzer, G.O., Anderson, D.M., Abbott, M.B., Enfield, D.B., Newman, J.H., 1999. An aprox. 15,000 - Year Record of El Niño - Driven Alluviation in Southwestern Ecuador. *Science* 283, 516–520.
- Rodbell, D.T., Bagnato, S., Nebolini, J.C., Seltzer, G.O., Abbott, M.B., 2002. A Late Glacial–Holocene Tephrochronology for Glacial Lakes in Southern Ecuador. *Quat. Res.* 57, 343–354.
- Rodbell, D.T., Seltzer, G.O., Mark, B.G., Smith, J.A., Abbott, M.B., 2008. Clastic sediment flux to tropical Andean lakes: records of glaciation and soil erosion. *Quat. Sci. Rev.* 27, 1612–1626.
- Roland, T.P., Mackay, H., Hughes, P.D.M., 2015. Rapid Communication Tephra analysis in ombrotrophic peatlands: A geochemical comparison of acid digestion and density separation techniques. *J. Quat. Sci.* 30, 3–8.

- Rüdel, H., Kösters, J., Schörmann, J., 2011. Determination of the Elemental Content of Environmental Samples using ICP-MS German Environmental Specimen Field of application General informatio. Guidelines for sampling, transport, storage and chemical characterisation of environmental and human samples, V 2.1.0.
- Salazar, G., Zhang, Y.L., Agrios, K., Szidat, S., 2015. Development of a method for fast and automatic radiocarbon measurement of aerosol samples by online coupling of an elemental analyzer with a MICADAS AMS. *Nucl. Instruments Methods Phys. Res. Sect. B Beam Interact. with Mater. Atoms* 361, 163–167.
- Sarà, G., Scilipoti, D., Mazzola, A., Modica, A., 2004. Effects of fish farming waste to sedimentary and particulate organic matter in a southern Mediterranean area (Gulf of Castellammare, Sicily): A multiple stable isotope study ($\delta^{13}\text{C}$ and $\delta^{15}\text{N}$). *Aquaculture* 234, 199–213.
- Sarakinos, H.C.H., Johnson, M.L., Vander Zanden, M., 2002. A synthesis of tissue-preservation effects on carbon and nitrogen stable isotope signatures. *Can. J. Zool* 80, 381–387.
- Sarmiento, F.O., 2002a. Anthropogenic changes in the landscapes of highland Ecuador. *Geogr. Rev.* 92, 213–234.
- Sarmiento, F.O., 2002b. Anthropogenic change in the landscapes of highland Ecuador. *Geogr. Rev.* 92, 213–234.
- Schillereff, D.N., Chiverrell, R.C., Macdonald, N., Hooke, J.M., 2014. Flood stratigraphies in lake sediments: A review. *Earth-Science Rev.* 135, 17–37.
- Schnurrenberger, D., Russell, J., Kelts, K., 2003. Classification of lacustrine sediments based on sedimentary components. *J. Paleolimnol.* 29, 141–154.
- Schultheiss, P.J., Weaver, P.P.E., 1992. Multi-sensor Core Logging for Science and Industry. *Oceans* 608–613.
- Schultze, E., Niederreiter, R., 1990. Paläolimnologische Untersuchungen an einem Bohrkern aus dem Profundal des Mondsees (Oberösterreich). n.a.
- Shane, P., 2000. Tephrochronology: A New Zealand case study, *Earth Science Reviews* 49, 223–259.
- Stewart, A.-M., Castro, J.M., 2016. P-T-X Evolution of the 1280 AD Quilotoa Dacite. *J. Volcanol. Geotherm. Res.* 313, 29–43.
- Straub, S.M., 1997. Multiple sources of Quaternary tephra layers in the Mariana Trough. *J. Volcanol. Geotherm. Res.* 76, 251–276.
- Stuiver, M., Reimer, P., 1986. A computer program for radiocarbon age calibration. *Radiocarbon* 28, 1022–1030.
- Sulpizio, R., Zanchetta, G., Paterne, M., Siani, G., 2003. A review of tephrostratigraphy in central and southern Italy during the last 65 ka. *J. Quat. Sci.* 16, 51–68.
- Suzuki, R., Shimodaira, H., 2006. Pvcust: an R package for assessing the uncertainty in hierarchical clustering. *Bioinformatics* 22, 1540–1542.
- Taggart, J.E., 2002. Analytical methods for chemical analysis of geologic and other materials, U.S. Geological Survey, 1-20.
- Teranes, J.L., Bernasconi, S.M., 2000. The record of nitrate utilization and productivity limitation provided by $\delta^{15}\text{N}$ values in lake organic matter—A study of sediment trap and core

- sediments from Baldeggersee, Switzerland. *Limnol. Ocean.* 45, 801–813.
- Thevenon, F., Adatte, T., Spangenberg, J.E., Anselmetti, F.S., 2012. Elemental (C/N ratios) and isotopic (^{15}N , ^{13}C) compositions of sedimentary organic matter from a high-altitude mountain lake (Meidsee, 2661 m a.s.l., Switzerland): Implications for Lateglacial and Holocene Alpine landscape evolution. *The Holocene* 22, 1135–1142.
- Thomas, R., 2001. A Beginner's Guide to ICP-MS Part II: The Sample-Introduction System. *Spectroscopy* 16, 56–61.
- Tierney, J.E., Mayes, M.T., Meyer, N., Johnson, C., Swarzenski, P.W., Cohen, A.S., Russell, J.M., 2010. Late-twentieth-century warming in Lake Tanganyika unprecedented since AD 500. *Nat. Geosci.* 3, 422–425.
- Tomlinson, E.L., Thordarson, T., Mueller, W., Thirlwall, M., Menzies, M.A., 2010. Microanalysis of tephra by LA-ICP-MS - Strategies, advantages and limitations assessed using the Thorsmork ignimbrite (Southern Iceland). *Chem. Geol.* 279, 73–89.
- Torres, I.C., Inglett, P.W., Brenner, M., Kenney, W.F., Reddy, K.R., 2012. Stable isotope ($\delta^{13}\text{C}$ and $\delta^{15}\text{N}$) values of sediment organic matter in subtropical lakes of different trophic status. *J. Paleolimnol.* 47, 693–706.
- Tuominen, L., Kairesalo, T., Hartikainen, H., 1994. Comparison of methods for inhibiting bacterial activity in sediment. *Appl. Environ. Microbiol.* 60, 3454–3457.
- Turney, C.S.M., 1998. Extraction of rhyolitic component of Vedde microtephra from minerogenic lake sediments. *J. Paleolimnol.* 19, 199–206.
- Tylmann, W., Bonk, A., Goslar, T., Wulf, S., Grosjean, M., 2016. Calibrating ^{210}Pb dating results with varve chronology and independent chronostratigraphic markers: Problems and implications. *Quat. Geochronol.* 32, 1–10.
- Tylmann, W., Enters, D., Kinder, M., Moska, P., Ohlendorf, C., Poreba, G., Zolitschka, B., 2013. Multiple dating of varved sediments from Lake Lazduny, northern Poland: Toward an improved chronology for the last 150 years. *Quat. Geochronol.* 15, 98–107.
- Tylmann, W., Fischer, H., Enters, D., Kinder, M., Moska, P., Ohlendorf, C., Poreba, G., Zolitschka, B., 2014. Reply to the comment by F. Gharbi on "Multiple dating of varved sediments from Lake Lazduny, northern Poland: Toward an improved chronology for the last 150 years." *Quat. Geochronol.* 20, 113.
- Van Acker, J., Wolff, C., Pino, M., Urrutia, R., Roberts, S., Vincze, L., De Batist Van Daele, M.M., Moernaut, J., Silversmit, G., Schmidt, S., Fontijn, K., Heirman, K., Vandoorne, W., De, M., Van Daele, M., De Clercq, M., De Batist, M., 2014. The 600 yr eruptive history of Villarrica Volcano (Chile) revealed by annually laminated lake sediments. *Geol. Soc. Am. Bull.* 1–19.
- Vander Zanden, M.J., Fetzer, W.W., 2007. Global Patterns of Aquatic Food Chain Length. *Oikos* 116, 1378–1388.
- Vander Zanden, M.J., Shuter, B.J., Lester, N., Rasmussen, J.B., 1999. Patterns of Food Chain Length in Lakes: A Stable Isotope Study. *The American Naturalist* 154, 406–416.
- Velastegui, A., 2010. Analisis geospacial y estadístico preliminar de la actividad minera en los paramos del Ecuador. PPA-EcoCiencia, Quito, 1–38.
- Venzke, E., 2016. Global volcanism program [WWW Document]. Smithsonian. Inst. URL http://volcano.si.edu/search_volcano.cfm

- Verburg, P., 2007. The need to correct for the Suess effect in the application of $\delta^{13}\text{C}$ in sediment of autotrophic Lake Tanganyika, as a productivity proxy in the Anthropocene. *J. Paleolimnol.* 37, 591–602.
- Villalba, R., Grosjean, M., Kiefer, T., 2009. Long-term multi-proxy climate reconstructions and dynamics in South America (LOTRED-SA): State of the art and perspectives. *Palaeogeogr. Palaeoclimatol. Palaeoecol.* 281, 175–179.
- Vizzini, S., Mazzola, A., 2004. Stable isotope evidence for the environmental impact of a land-based fish farm in the western Mediterranean. *Mar. Pollut. Bull.* 49, 61–70.
- Vogel, H., Zanchetta, G., Sulpizio, R., Wagner, B., Nowaczyk, N., Vogel, H., Zanchetta, G., Wagner, R., Nowaczyk, B., 2009. A tephrostratigraphic record for the last glacial–interglacial cycle from Lake Ohrid, Albania and Macedonia. *J. Quat. Sci.*, 1–19.
- von Gunten, L., Grosjean, M., Kamenik, C., Fujak, M., Urrutia, R., 2012. Calibrating biogeochemical and physical climate proxies from non-varved lake sediments with meteorological data: Methods and case studies. *J. Paleolimnol.* 47, 583–600.
- Vos, R., Velasco, M., de Labastida, E., 1999. Economic and Social Effects of El Niño in Ecuador , 1997-1998, Sustainable development department technical papers series. Washington, D.C.
- Vuille, M., Bradley, R.S., Keimig, F., 2000a. Interannual climate variability in the Central Andes and its relation to tropical Pacific and Atlantic forcing. *J. Geophys. Res.* 105, 14447–12460.
- Vuille, M., Bradley, R.S., Keimig, F., 2000b. Climate Variability in the Andes of Ecuador and its Relation to Tropical Pacific and Atlantic Sea Surface Temperature Anomalies. *J. Clim.* 13, 2520–2535.
- Watson, E.J., Swindles, G.T., Lawson, I.T., Savov, I.P., 2016. Do peatlands or lakes provide the most comprehensive distal tephra records? *Quat. Sci. Rev.* 139, 110–128.
- Wilks, D.S., 2011. *Statistical Methods in the Atmospheric Sciences*, 3rd Revised edition. Elsevier Science Publishing Co Inc, San Diego.
- Wilson, S., 1997. The collection, preparation and testing of USGS reference material BCR-2, Columbia River, Basalt, U.S. Geological Survey Open-File Report, 98-100.
- Wirth, S.B., Gilli, A., Simonneau, A., Ariztegui, D., Vanni, B., Glur, L., Chapron, E., Magny, M., Anselmetti, F.S., 2013. A 2000 year long seasonal record of floods in the southern European Alps. *Eur. Alps . Geophys. Res. Lett.* 40, 4025–4029.
- Wohlfarth, B., Skog, G., Possnert, G., Holmquist, B., 1998. Pitfalls in the AMS radiocarbon-dating of terrestrial macrofossils. *J. Quat. Sci.* 13, 137–145.
- Xia, D., Chun, X., Bloemendal, J., Chiverrell, R.C., Chen, F., 2007. Use of magnetic signatures to correlate tephra layers in Holocene loessial soil profiles from a small region, SE Iceland. *Environ. Geol.* 51, 1425–1437.
- Ye, L.X., Ritz, D.A., Fenton, G.E., Lewis, M.E., 1991. Tracing the influence on sediments of organic waste from a salmonid farm using stable isotope analysis. *J. Exp. Mar. Bio. Ecol.* 145, 161–174.

Plate I: Macrofossils *L. Llaviucu*



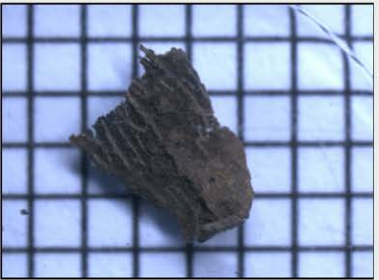
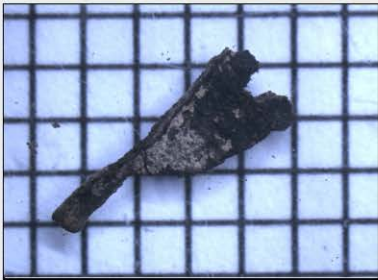








		
<p>LLA14-1a Pooled sample from a leaf, part of a bud and insect part.</p>	<p>LLA14-1c(1) Part of a leaf</p>	<p>LLA14-1c(2) Part of a leaf</p>
		
<p>LLA14-1c(3) Part of a leaf</p>	<p>LLA14-1c(4) Part of a leaf</p>	<p>LLA14-1c(5) Part of a leaf</p>
		
<p>LLA15-6a Piece of wood, located above tephra layer</p>	<p>LLA15-6a Leaf fragment</p>	<p>LLA15-6b Seed shell</p>
		
<p>LLA15-6c Leaf fragment</p>	<p>LLA15-6e(1) Seed fragment</p>	<p>LLA15-6e(2) Seed fragment</p>

Plate II: Macrofossils L. Fondococha

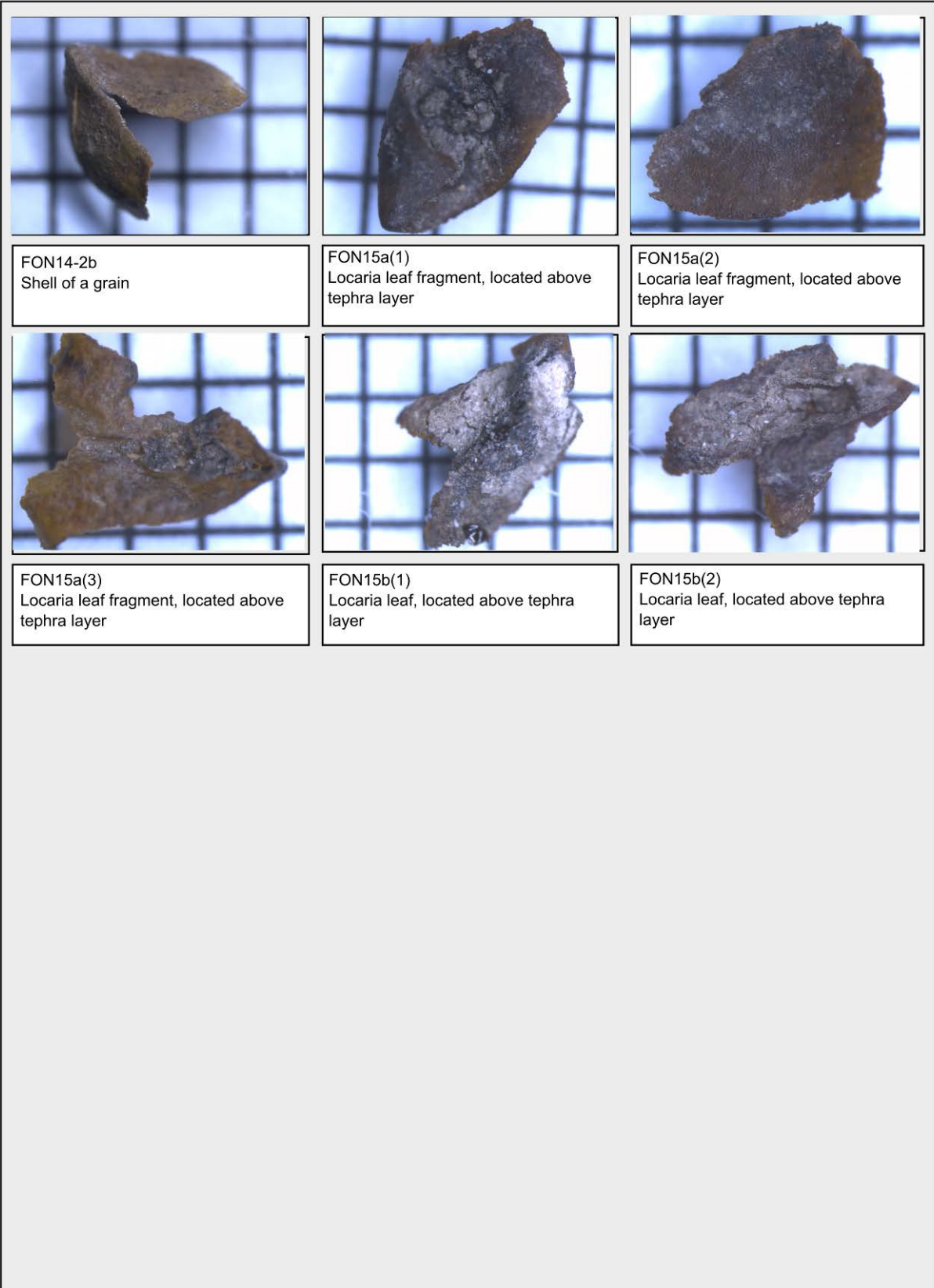


Plate III: Tephra

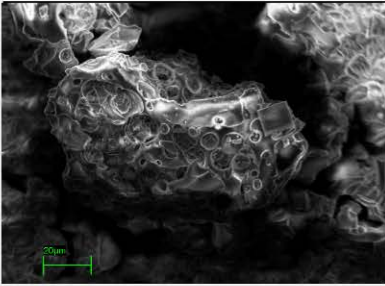
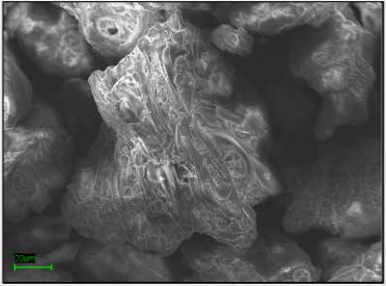
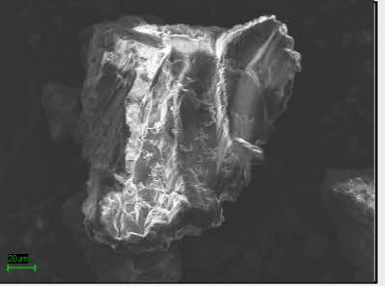
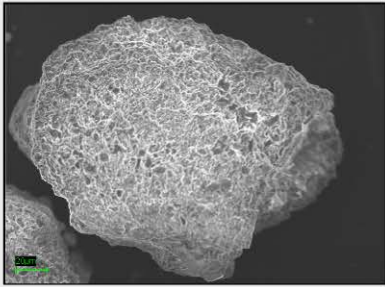
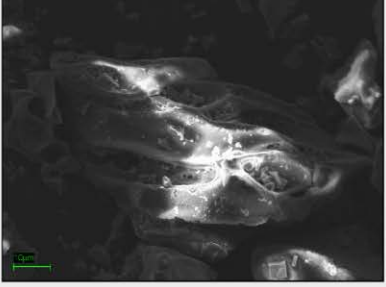
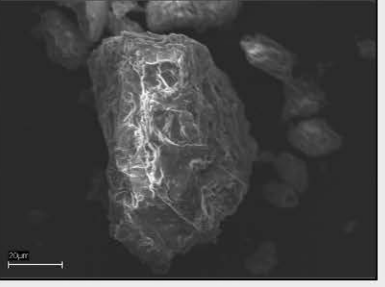

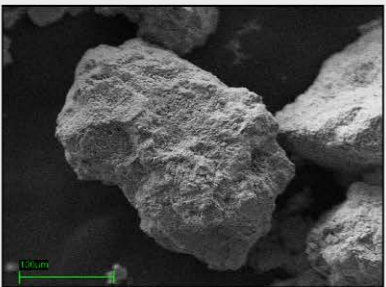
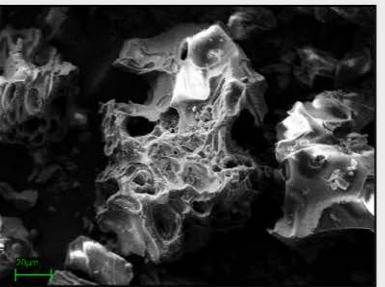

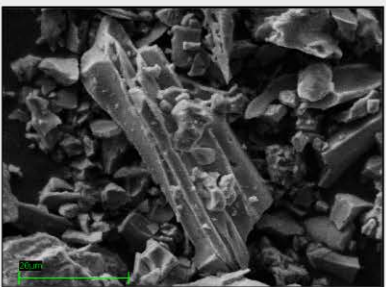
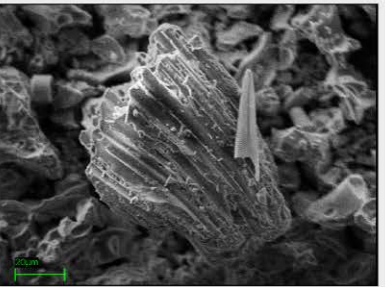
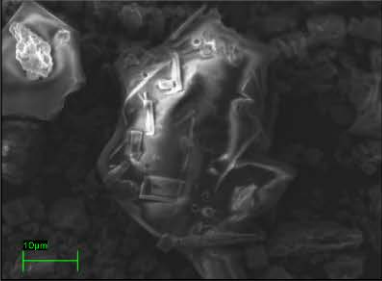
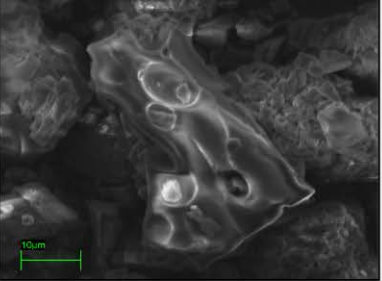

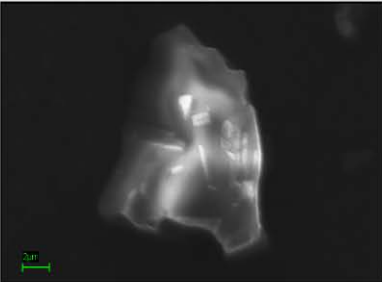
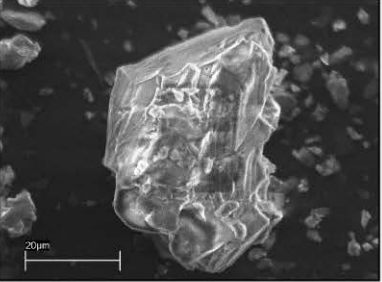
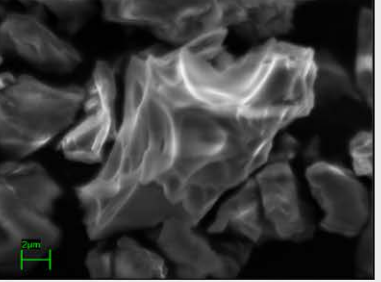

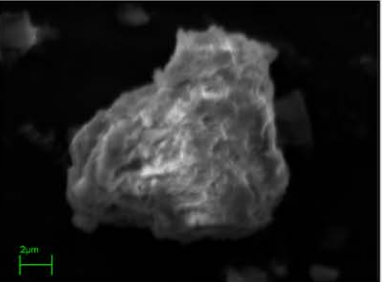
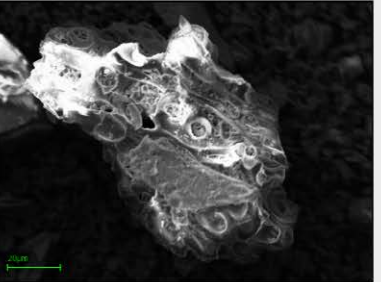
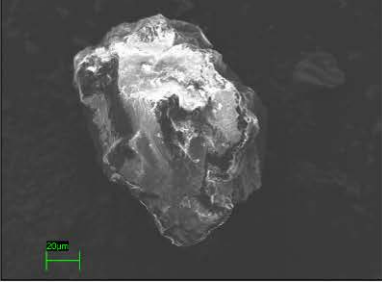
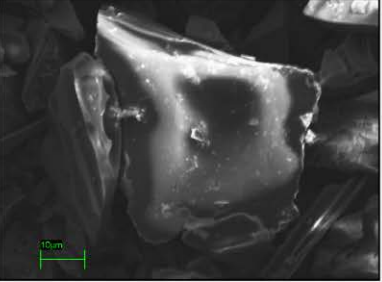
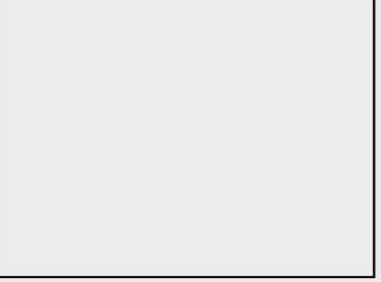
		
RIN15-3/4/5-A	LLA15-6-B	LLA15-3/4/5-B
		
LLA15-3/4/5-B	EST15-3-A	LLA15-3/4/5-C
		
LLA15-3/4/5-A	LLA15-4/5-D	RIN14-1-B
		
LLA14-2-B	RIN14-1-A	EST15-3-A

Plate IV: Tephra continued

		
LLA15-6-C	FON14-1-A	FON14-2-A
		
EST15-1-A	LLA15-6-C	LLA15-6-A
		
FON15-3-B	LLA14-2-A	FON14-1-B
		
LLA14-2-C	RIN15-3/5-B	

Declaration

under Art. 28 Para. 2 RSL 05

Last, first name: Stéphanie Arcusa

Matriculation number: 14-108-351

Programme: Masters in Climate Sciences

Bachelor Master Dissertation

Thesis title: Late Holocene flood history and tephrochronology using lake sediments from
Cajas National Park, south central Ecuador

Thesis supervisor: Prof. Dr. Martin Grosjean

I hereby declare that this submission is my own work and that, to the best of my knowledge and belief, it contains no material previously published or written by another person, except where due acknowledgement has been made in the text. In accordance with academic rules and ethical conduct, I have fully cited and referenced all material and results that are not original to this work. I am well aware of the fact that, on the basis of Article 36 Paragraph 1 Letter o of the University Law of 5 September 1996, the Senate is entitled to deny the title awarded on the basis of this work if proven otherwise. I grant inspection of my thesis.

.....

.....

Place, date

Signature